

AD-A058 326

OHIO STATE UNIV RESEARCH FOUNDATION COLUMBUS  
FUNDAMENTAL STUDIES OF DISSOLUTION AND PASSIVITY OF ALLOYS AND --ETC(U)  
JUL 78 J B LUMSDEN, R W STAENLE, L ABREGO

F/G 11/6

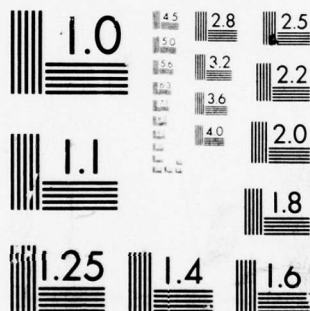
N00014-75-C-0665

NL

UNCLASSIFIED

1 OF 2  
AD  
A068326





MICROCOPY RESOLUTION TEST CHART  
NATIONAL BUREAU OF STANDARDS-1963-A



ADA 058326

AD No.

DDC FILE COPY

**the  
ohio  
state  
university**

**research foundation**

1314 kinnear road  
columbus, ohio  
43212

RF Project 760233/784131  
Final Report

**LEVEL** ~~III~~

A035271

(12)

Sc

FUNDAMENTAL STUDIES OF  
DISSOLUTION AND PASSIVITY OF ALLOYS AND COMPOUNDS

J. B. Lunsden, R. W. Staehle, L. Abrego  
Department of Metallurgical Engineering

For the Period  
March 1, 1977 - February 28, 1978

U.S. DEPARTMENT OF THE NAVY  
Office of Naval Research  
Arlington, Virginia 22217

Contract No. N00014-75-C-0665

July, 1978

DDC  
RECEIVED  
SEP 1 1978  
A

DISTRIBUTION STATEMENT A  
Approved for public release;  
Distribution Unlimited

78 08 07 047

FUNDAMENTAL STUDIES OF DISSOLUTION  
AND PASSIVITY OF ALLOYS AND COMPOUNDS

Research Program for the  
Office of Naval Research

Contract # N00014-75-C-0665 (NR036-085)

Report of Work During the Period  
1 March 1977 - 28 February 1978

J. B. Lumsden  
R. W. Staehle

Department of Metallurgical Engineering  
The Ohio State University  
Columbus, Ohio

Reproduction in whole or in part is permitted for  
any purpose of the United States Government

Unclassified

SECURITY CLASSIFICATION OF THIS PAGE (When Data Entered)

REPORT DOCUMENTATION PAGE		READ INSTRUCTIONS BEFORE COMPLETING FORM
1. REPORT NUMBER	2. GOVT ACCESSION NO.	3. RECIPIENT'S CATALOG NUMBER
4. TITLE (and Subtitle) FUNDAMENTAL STUDIES OF DISSOLUTION AND PASSIVITY OF ALLOYS AND COMPOUNDS		5. TYPE OF REPORT & PERIOD COVERED Final Report 3/1/77 through 2/28/78
6. AUTHOR(s) J.B./Lumsden, R.W./Staehle L./Abrego		7. PERFORMING ORG. REPORT NUMBER OSURF-784131-3
8. PERFORMING ORGANIZATION NAME AND ADDRESS The Ohio State University Research Foundation 1314 Kinnear Road Columbus, Ohio 43212		9. CONTRACT OR GRANT NUMBER(s) N00014-75-C-0665
10. CONTROLLING OFFICE NAME AND ADDRESS Office of Naval Research Code N00014 Department of the Navy Arlington, Virginia 22217		11. PROGRAM ELEMENT, PROJECT, TASK AREA & WORK UNIT NUMBERS NR 036-085/1-3/75 (471)
12. MONITORING AGENCY NAME & ADDRESS (if different from Controlling Office) Office of Naval Research Resident Representative The Ohio State University Research Center 1314 Kinnear Road Columbus, Ohio 43212		13. REPORT DATE June 1978
14. DISTRIBUTION STATEMENT (of this Report) Reproduction in whole or in part is permitted for any purpose of the United States Government.		14. NUMBER OF PAGES 109
15. DISTRIBUTION STATEMENT (of the abstract entered in Block 20, if different from Report) Final rept. 12 Mar 77-28 Feb 78		15. SECURITY CLASS. (of this report) Unclassified
16. SUPPLEMENTARY NOTES		15a. DECLASSIFICATION/DOWNGRADING SCHEDULE
17. KEY WORDS (Continue on reverse side if necessary and identify by block number) Auger spectroscopy      Pitting Passive film              Iron Silicon Passivation Corrosion		
18. ABSTRACT (Continue on reverse side if necessary and identify by block number) This investigation was concerned with rationalizing the improved stability of passive films obtained by the addition of silicon to iron. Auger Spectroscopy and electrochemical techniques were used. The results indicated the following: (1) The beneficial effects of silicon alloying for corrosion resistance is not effective until the alloy contains 14.5 wt % (25 at %) silicon; silicon contents of less than 8 wt % (15 at %) are detrimental to the corrosion properties in sulfate and chloride solutions.		

DD FORM 1473 1 JAN 73

EDITION OF 1 NOV 65 IS OBSOLETE

Unclassified

SECURITY CLASSIFICATION OF THIS PAGE (When Data Entered)

267 360

Unclassified

SECURITY CLASSIFICATION OF THIS PAGE(When Data Entered)

- (2) Silicon enrichment and the formation of an  $\text{SiO}_2$  film are responsible for the corrosion resistant properties.
- (3) The formation of an  $\text{SiO}_2$  film resists the penetration of the sulfate anion.
- (4) Since no evidence of enhanced pitting resistance was noted in 3 and 8 wt % (6.5 and 15 at %) silicon alloys, it is postulated that the increased pitting resistance noted in stainless steels with 2-3 % silicon is due to a synergistic effect of silicon with another alloying element.

ACCESSION FOR	
RTIS	White Section <input checked="" type="checkbox"/>
DDB	Buff Section <input type="checkbox"/>
UNANNOUNCED	
JUSTIFICATION	<i>Pitting on file</i>
BY	
DISTRIBUTION/AVAILABILITY CODES	
Dist.	AVAIL. and/or SPECIAL
A	

SECURITY CLASSIFICATION OF THIS PAGE(When Data Entered)



# TABLE OF CONTENTS

	<u>Page</u>
ABSTRACT	
1.0 INTRODUCTION . . . . .	1
2.0 CORROSION PROPERTIES OF IRON-SILICON ALLOY . . . . .	1
3.0 EXPERIMENTAL PROCEDURE . . . . .	7
4.0 EXPERIMENTAL RESULTS . . . . .	13
4.1 Introduction . . . . .	13
4.2 Microstructure . . . . .	14
4.3 Electrochemical Behavior . . . . .	14
4.3.1 Borate Buffer Solution . . . . .	14
4.3.2 Sulfate Solutions . . . . .	20
4.3.3 Borate Buffer + 0.1M Potassium Chloride . . . . .	29
4.3.4 0.1N and 0.5N Sodium Chloride . . . . .	33
4.3.5 1N Hydrochloride Acid . . . . .	33
4.4 AES Film Composition Results . . . . .	39
4.4.1 Introduction . . . . .	39
4.4.2 Air Formed Films . . . . .	40
4.4.3 Borate Buffer Films . . . . .	46
4.4.4 Sulfate Solution Films . . . . .	52
4.4.5 Films in Borate Buffer + 0.1M Potassium Chloride . . . . .	68
4.4.6 Films in 0.1N Sodium Chloride . . . . .	74
4.4.7 Average Film Composition Determination . . . . .	74
4.5 Current Decay Curves in Sulfate Solutions . . . . .	79
5.0 DISCUSSION . . . . .	89
5.1 Introduction . . . . .	89
5.2 The Polarization Potential . . . . .	89
5.3 Passivity . . . . .	94
5.3.1 Current Decay . . . . .	96
5.4 The pH Effect . . . . .	101
5.5 Breakdown of Passivity . . . . .	103
5.6 The Anion Effect . . . . .	104
5.6.1 Borate . . . . .	104
5.6.2 The Sulfate Ion . . . . .	105
5.6.3 Chloride Ion . . . . .	106
6.0 CONCLUSIONS . . . . .	107
References . . . . .	108

## LIST OF FIGURES

<u>Figure</u>	<u>Page</u>
1a. Potential-pH equilibrium diagram for the water-silicon system at 25°C considering only Fe, Fe <sub>3</sub> O <sub>4</sub> and Fe <sub>2</sub> O <sub>3</sub> . (3)	2
1b. Potential-pH equilibrium diagram for the water-silicon system at 25°C. (3)	3
2. Effect of alloyed silicon on the corrosion resistance of iron in 10% sulfuric acid at 80°C. (4)	5
3. Auger spectrum taken before sputtering. Note large oxygen peak and SiO <sub>2</sub> peak.	11
4. Auger spectrum taken after sputtering. Note disappearance of oxygen peak.	12
5a. Microstructure of 100Fe sample (nital etch, 100X).	15
5b. Microstructure of 3Si sample (nital etch, 100X).	15
5c. Microstructure of 8Si sample (mixed acids/glycerol etch, 100X).	16
5d. Microstructure of 10Si sample (mixed acids/glycerol etch, 100X).	16
5e. Microstructure of 14.5Si sample (mixed acids/glycerol etch, 500X).	17
6. The polarization curves of Fe-Si Alloys in a borate buffer solution (pH = 8.4).	18
7. The open circuit and passivation potential (NHE) vs silicon content in a borate buffer solution.	19
8. The passive and active current density vs silicon content in a borate buffer solution.	21
9. Polarization curve of iron-silicon alloys in 1N H <sub>2</sub> SO <sub>4</sub> , pH = 0.4 (scanning rate 50 mV/min.).	22
10. Polarization curves for iron-silicon alloys in 1N Na <sub>2</sub> SO <sub>4</sub> , pH = 3.2 (scanning rate 50 mV/min.).	23
11. Polarization curves for iron-silicon alloys in 1N Na <sub>2</sub> SO <sub>4</sub> , pH = 6.4 (scanning rate 50 mV/min.).	24

<u>Figure</u>		<u>Page</u>
12.	Polarization curves for iron-silicon alloys in 1N Na <sub>2</sub> SO <sub>4</sub> , pH = 10.2 (scanning rate 50 mV/min.).	25
13.	Polarization curves for iron-silicon alloys in 1N Na <sub>2</sub> SO <sub>4</sub> , pH = 14 (scanning rate 50 mV/min.; pH adjusted with NaOH).	27
14.	The open circuit and passivation potential vs solution pH for iron-silicon alloys in sulfate solutions.	28
15.	The passive current density and active current vs pH of Fe-Si alloys in the sulfate solutions.	31
16.	Polarization curves of iron-silicon alloys in borate buffer with potassium chloride.	32
17.	Pitting potential for iron-silicon alloys in borate buffer and 0.1M potassium chloride determined by the "scratch technique."	34
18.	Example of pits which formed on iron in borate buffer and 0.1M potassium chloride (200X).	35
19.	Example of pits which formed on 3Si in borate buffer and 0.1M potassium chloride (150X).	35
20.	Polarization curve of iron-silicon alloys in 0.1N NaCl (scanning rate 20 mV/min.).	36
21.	Polarization curve of iron-silicon alloys in 0.5M NaCl; the potential was held until the current reached a steady value.	37
22.	Polarization curve of iron-silicon alloys in 1N HCl (scanning rate 50 mV/min.).	38
23.	Auger compositional profile of film formed on 3Si sample exposed to only the air for 24 hours (sputtering voltage 600 V).	41
24.	Auger compositional profile of film formed on 8Si sample exposed to only the air for 24 hours (sputtering voltage 600 V).	42
25.	Auger compositional profile of film formed on 10Si sample exposed to only the air for 24 hours (sputtering voltage 600 V).	43

<u>Figure</u>		<u>Page</u>
26.	Auger compositional profile of film formed on 14.5Si sample exposed to only the air for 24 hours (sputtering voltage 600 V).	44
27.	Auger compositional profile of silica formed in air on a silicon wafer.	45
28.	Auger compositional profile of 100Fe passivated for 1 hr in borate buffer at 200 mV (SCE) with sputtering voltage 600 V.	47
29.	Auger compositional profile of film formed in borate buffer solution at 200 mV (SCE) for 1 hr (sputtering voltage of 600 V).	48
30.	Auger compositional profile of film formed on 8 Si sample polarized in borate buffer solution at 200 mV (SCE) for 1 hr (sputtering voltage 600 V).	49
31.	Auger compositional profile of film formed on 10Si sample polarized in borate buffer solution at 200 mV (SCE) for 1 hr (sputtering voltage 600 V).	50
32.	Auger compositional profile for 14.5Si in borate buffer solution.	51
33.	Auger compositional profile for iron with film formed in 1N sulfuric acid.	53
34.	Auger compositional profile of film formed on 3Si in 1N sulfuric acid.	54
35.	Auger compositional profile of film formed on 8Si sample polarized at 800 mV (SCE) for 1 hr (sputtering voltage 600 V).	55
36.	Auger compositional profile of film formed on 10Si in 1N sulfuric acid.	56
37.	Auger compositional profile of film formed on 14.5Si sample polarized in 1N sulfuric acid at 800 mV (SCE) for 1 hr (sputtering voltage 600 V).	57
38.	Auger compositional profile of film formed on 100Fe sample polarized in 1N sodium sulfate (pH = 3.2) at 600 mV (SCE) for 1 hr (sputtering voltage 600 V).	58



Figure

Page

39. Auger compositional profile of film formed on 3Si in 1N sodium sulfate. 59
40. Auger compositional profile of film formed on 8Si in 1N sodium sulfate. 60
41. Auger compositional analysis of film formed on 10Si in 1N sodium sulfate, pH = 3.2. 61
42. Auger compositional profile of 14.5Si with film formed in 1N sodium sulfate, pH = 3.2. 62
43. Auger compositional profile of film formed on iron in 1N sodium sulfate. 63
44. Auger compositional profile of film formed on 3Si sample polarized in 1N sodium sulfate (pH = 6.4) at 600 mV (SCE) for 1 hr (sputtering voltage 600 V). 64
45. Auger compositional profile of film formed on 8Si sample polarized in 1N sodium sulfate (pH = 6.4) at 600 mV (SCE) for 1 hr (sputtering voltage 600 V). 65
46. Auger compositional profile of film formed on 10Si in 1N sodium sulfate. 66
47. Auger compositional profile of film formed on 14.5Si in 1N sodium sulfate. 67
48. Auger compositional profile of film formed on iron in 1N sodium sulfate, pH = 10. 69
49. Auger compositional profile of film formed on 10Si sample polarized in 1N sodium sulfate (pH = 10.3) at 600 mV (SCE) for 1 hr (sputtering voltage 600 V). 70
50. Auger compositional profile of film formed on 14.5Si sample polarized in 1N sodium sulfate (pH = 10.3) at 600 mV (SCE) for 1 hr (sputtering voltage 600 V). 71

<u>Figure</u>		<u>Page</u>
51.	Examples of the type of pits analyzed by scanning Auger in Figure 7; note the etched area surrounding the pits.	72
52.	Scanning Auger elemental distribution of material around a pit formed on 8Si in borate buffer and 0.1M potassium chloride.	73
53.	Auger compositional profile of material in "flow region" around pit in 8Si.	75
54.	Auger compositional profile of unpitted area on 8Si sample on which pits formed in borate buffer plus 0.1M potassium chloride solution (sputtering voltage 600 V).	76
55.	Auger compositional profile of material in "flow region" around pit in 3Si.	77
56.	Auger analysis on a 14.5Si sample which had been passivated for 1 hr in 0.1N NaCl at 200 mV SCE (440 mV NHE).	78
57.	Average air oxide film Si content vs alloy silicon content. Dashed line represents equal concentrations in the oxide and the alloy.	80
58.	Average anodic oxide film Si content vs alloy Si content. Dashed line represents equal concentrations in the oxide and the alloy.	81
59.	Average anodic oxide film silicon content vs alloy silicon content. Dashed line represents equal concentrations in the oxide and the alloy.	82
60.	Average anodic oxide film Si content vs alloy Si content. Dashed line represents equal concentrations in the oxide and the alloy.	83
61.	Average anodic oxide film Si content vs alloy Si content. Dashed line represents equal concentrations in the oxide and the alloy.	84

<u>Figure</u>	<u>Page</u>
62. Current decay curves for iron-silicon alloys in 1N H <sub>2</sub> SO <sub>4</sub> , pH = 0.4, E <sub>app</sub> = 800 mV (SCE), 1040 mV (NHE).	85
63. Current decay curves for iron-silicon alloys in 1N Na <sub>2</sub> SO <sub>4</sub> , pH = 3.2, E <sub>app</sub> = 600 mV (SCE), 840 mV (NHE).	86
64. Current decay curves for iron-silicon alloys in 1N Na <sub>2</sub> SO <sub>4</sub> , pH = 6.4, E <sub>app</sub> = 600 mV (SCE), 840 mV (NHE).	87
65. Current decay curves for iron-silicon alloys in 1N Na <sub>2</sub> SO <sub>4</sub> , pH = 10.2, E <sub>app</sub> = 600 mV (SCE), 840 mV (NHE).	88
66. The change in the corrosion potential E <sub>r</sub> as a function of alloy Si content (at %).	92
67. The change in passivation potential, E <sub>p</sub> , as a function of alloy Si content (at %).	93
68. The change in active and passive current densities as a function of alloy silicon content (at %).	95
69. The change in slopes of the current density vs time plots as a function of silicon content of the alloy (at %).	97
70. Film thickness calculated from the total charge passed during current decay plotted vs atomic % silicon.	99
71. Film thickness from Auger sputtering times assuming a sputtering rate of 1-3 Å/min plotted vs atomic % silicon in the alloy.	100

#### LIST OF TABLES

Table I	Alloy Composition	8-9
Table II	Open Circuit Potential (NHE) - pH Relationships (pH < 7) for Sulfate Solutions	30
Table III	Passivation Potential (NHE) - pH Relationships for Sulfate Solutions	30
Table IV	Slopes from Current Decay Curves in Sulfate Solutions	90

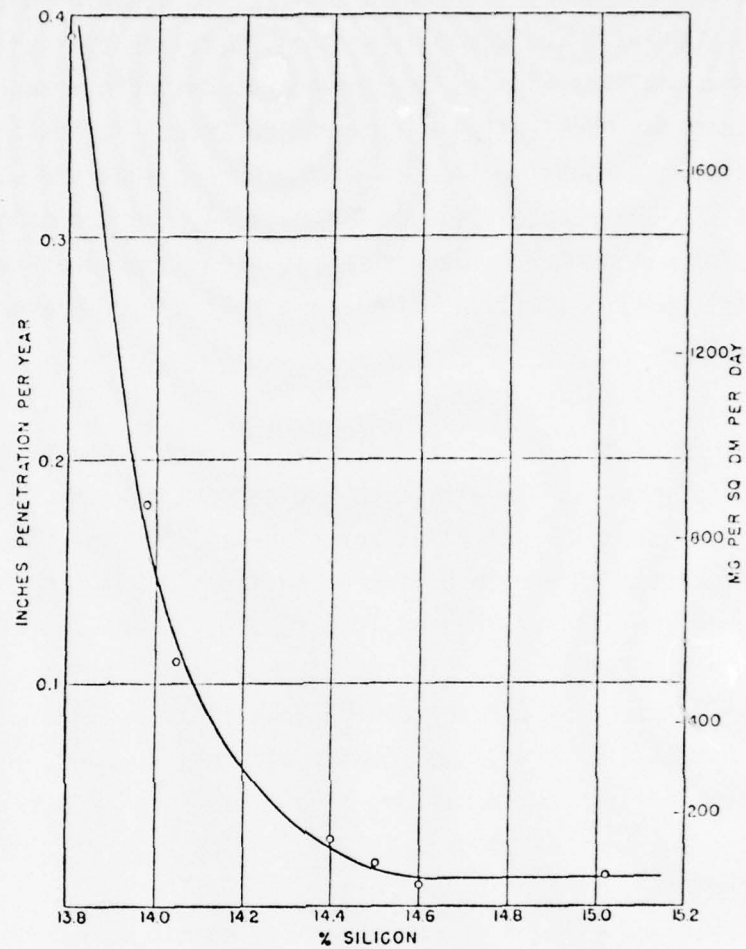
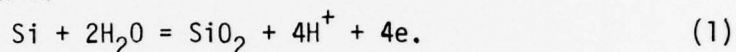


Figure 2. Effect of alloyed silicon on the corrosion resistance of iron in 10% sulfuric acid at 80°C. (4)



the passive region (8-11). A mechanism for this behavior has been postulated by Omartug and Duruk (8). They postulate that silicon acts as a cathodic additive and creates anodic and cathodic areas on the alloy that stimulate the passivation of the entire area. At low silicon concentrations, the passive film is mostly iron oxides and some silica. However, as silicon reaches 14.5 wt % (25 at %), the corrosion rate is then due to the formation of  $\text{SiO}_2$  because there is an increased availability of silicon atoms to form a silica film. The half cell reaction associated with passivation is



The effect of silicon on the corrosion potential in 1N sulfuric acid is not as consistent as its effect on the current density. Crow et al (9) determined the corrosion potential for a series of iron-silicon alloys; they found that the corrosion potential shifts slightly in the negative direction when the silicon content is 2 to 6 wt %, but it shifts in the positive direction at 12 wt % silicon. Low silicon alloys exhibit polarization behavior similar to that of iron except that their passive current density is higher than that of iron. At 15 wt % silicon, however, the alloys have excellent passivation behavior. The difference in passivation behavior suggests that the mechanism for passivity in the high silicon alloys is different from that in the low silicon alloys (11).

The effects of silicon on corrosion resistance is not limited to binary alloys. In austenitic stainless steels silicon additions of 2-3 wt % have improved the pitting resistance of the alloys in chloride environments (12, 13) and also improved the stress corrosion resistance (14). This effect was explained by an argument similar to that used for the binary alloys, i.e., that there was a preferential dissolution of the more reactive elements in the alloy leaving behind a passive film enriched in silica (15).

But a reassessment of the film stripping technique used by Rhodin (15) to determine the composition of the passive film has established that the stripped films were heavily contaminated with ferrous salts derived from

## 1.0 INTRODUCTION

This is an investigation of the electrochemical and composition aspects of iron-silicon alloys in aqueous environments. This work is concerned primarily with understanding the role of alloying and environmental species on the passivity of iron base alloys in aqueous environments. To this end this work undertook the investigation of the behavior of iron-silicon alloys in borate buffer, sulfate, and chloride environments.

Auger electron spectroscopy for composition analysis of the passive films formed on the alloys under controlled electrochemical conditions were undertaken. Thus, the effects of alloying, potential, and pH on the film composition were assessed. With the addition of chloride ions to the aqueous solution the breakdown of passivity was also investigated; film and substrate compositions inside the growing pits were obtained.

This investigation determined that the corrosion resistance of iron-silicon alloys is due to the formation of a film of  $\text{SiO}_2$  which occurs only when the alloy composition reaches 14.5 wt % (25 at %) silicon.

## 2.0 Corrosion Properties of Iron-Silicon Alloys

It has been known for many years that iron-silicon alloys show an increased corrosion resistance as the silicon content approaches 14.5 wt % (25 at %) silicon (1, 2). Although limited in usefulness by a low tensile strength and brittleness, iron-silicon alloys from 13 to 15 wt % silicon are important for their effective resistance to acids. In spite of their drawbacks, iron-silicon equipment is produced in cast form and used for special applications in chemical plants.

The effect of silicon in aqueous environments can somewhat be justified by a comparison of the Pourbaix equilibrium diagrams for iron-water and silicon-water systems shown in Figures 1a and 1b respectively. There is a wide range of stability for  $\text{SiO}_2$ , while dissolution of iron is indicated

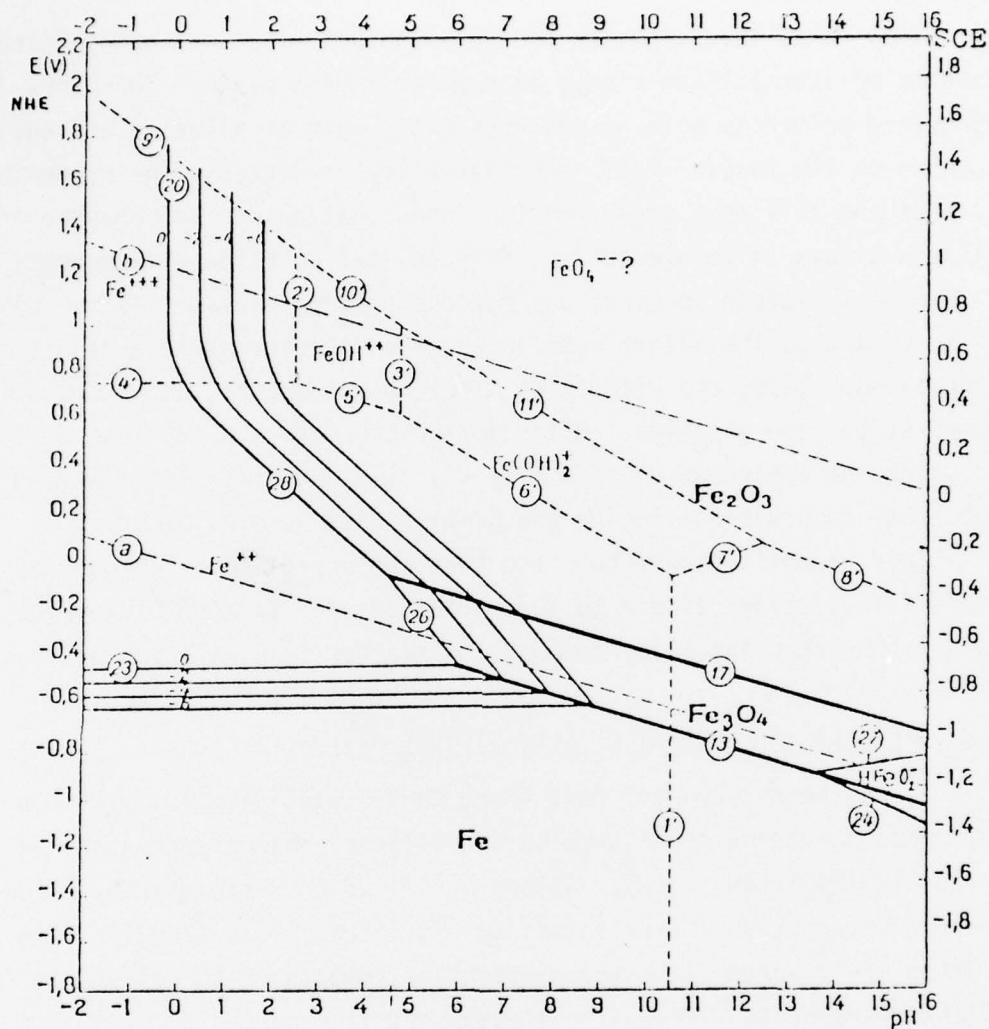


Figure 1a. Potential-pH equilibrium diagram for the water-silicon system at 25°C considering only Fe, Fe<sub>3</sub>O<sub>4</sub> and Fe<sub>2</sub>O<sub>3</sub>. (3)

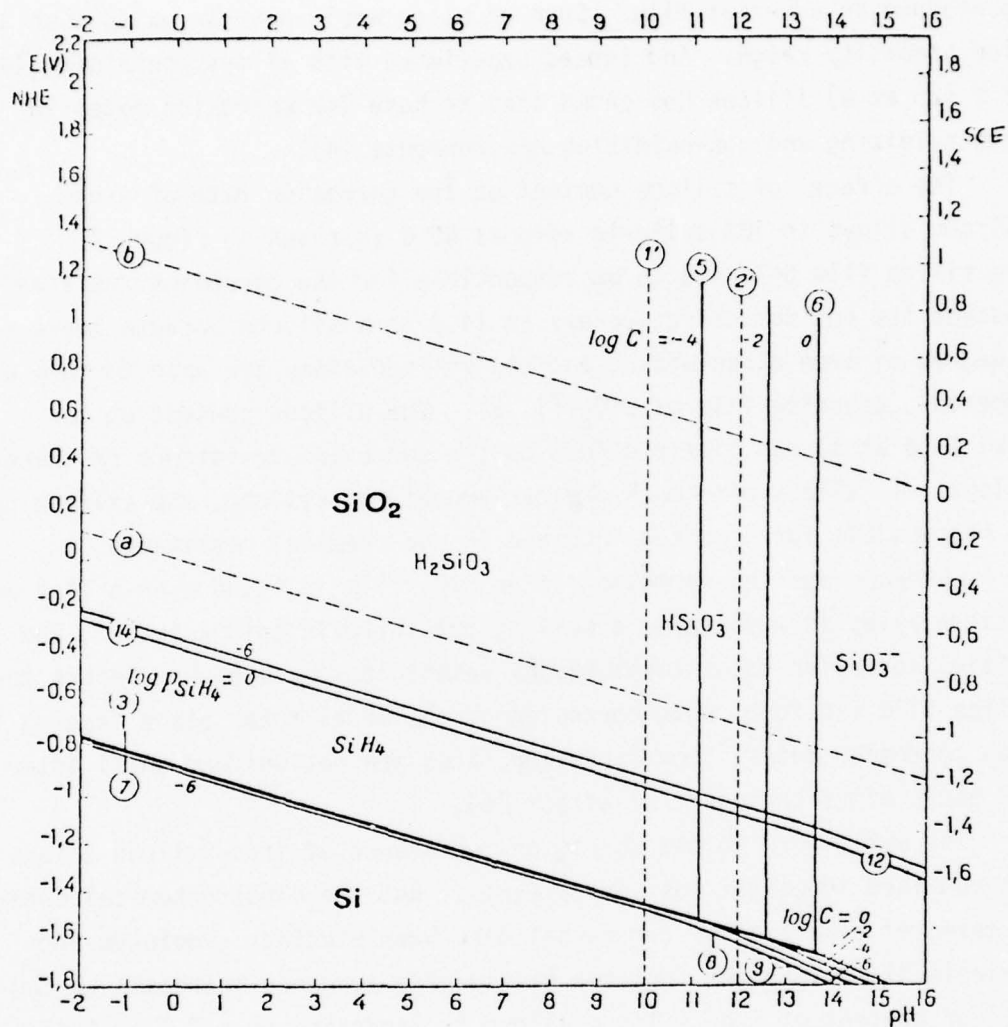


Figure 1b. Potential-pH equilibrium diagram for the water-silicon system at 25°C. (3)



in the acid pH regions (3). Superposition of the diagrams implies that an alloy of iron-silicon would have some dissolution of iron but passivity by the formation of silica if the silicon content is sufficient to produce an adherent film. Such an alloy would have an oxide with a wide stability range. And indeed experience with alloys containing 14.5 wt % (25 at %) silicon has shown them to have low corrosion rates in both oxidizing and non-oxidizing environments (4).

The effect of silicon content on the corrosion rate of iron silicon alloys in 10% sulfuric acid at 80°C is shown in Figure 2. The silica film believed to be responsible for the corrosion resistance reaches its optimum effectiveness at 14.5 wt % silicon because there occurs a degree of iron dissolution, and the silicon atoms are able to form a tightly adherent, cohesive film of  $\text{SiO}_2$  (1, 5). The silicon content up to 3 wt % (6 at %) has little effect on the corrosion resistance of these alloys. In alloys with much greater amounts of silicon, the silicon content is responsible for a marked increase in the chemical resistance.

Evidence for the formation of an  $\text{SiO}_2$  film is found when a 14.5 wt % silicon alloy is exposed to a boiling 30% sulfuric acid solution; the initial corrosion rates (measured by weight loss) are high. Before the silica film can form, some corrosion of the metal takes place leading to high corrosion rates. Low corrosion rates are not uniform until after 100 hours after the onset of attack (6).

The early work in the corrosion resistance of iron-silicon alloys was confined to weight loss experiments. But the electrochemical behavior in terms of polarization curves has also been studied. Robinson and DuPlessis (7) have shown that the passivating tendency increases as the silicon content of iron silicon alloys is increased from 7.5 wt % to 15 wt %. A 7.5 wt % alloy shows little to no passivation in 2.5 % hydrochloric acid, while a 15 wt % alloy shows a decrease in the current density marking the onset of passivity.

Further electrochemical studies at 25°C in sulfuric acid show that the effect of silicon on the active-passive behavior of its alloys is to decrease the active peak current density and to increase the extent of

the stripping solutions, and that the high water content noted in the films was probably due to the hygroscopic nature of the contaminant (16). Consequently, silicon enrichment is questionable.

Silicon is evidently a useful addition to stainless steels imparting added corrosion resistance to those alloys. However, increasing the silicon content above 3 wt % does not produce significant changes in the corrosion properties. This lack of greater effect by silicon is surprising because if silicon were enriched in the passive film as previously postulated, it might be expected to have a greater effect on the corrosion properties (17).

From the preceding survey it can be noted that silicon exerts two types of beneficial alloying effects. There is a critical concentration of 14.5 wt % (25 at %) silicon where substantial changes in the corrosion behavior occur; and there is a different type of effect in the austenitic and ferritic stainless steels where the critical concentration of silicon is decreased by a factor of five.

### 3.0 EXPERIMENTAL PROCEDURE

The sample compositions, preparation procedure, and electrochemical techniques were documented in the previous reporting period. In this section the surface analysis technique is presented.

Table I lists the chemical composition and fabrication history of the samples used in this study.

#### Auger Electron Spectroscopy (AES)

The composition of the passive films was determined by Auger electron spectroscopy. For this analysis each sample was prepared as previously described for polarization measurements. The specimen was cathodically polarized for 10 minutes and then anodically polarized to the potential of interest; it was held at that potential for one hour while the current behavior was monitored.

TABLE I

ALLOY COMPOSITION

Elements:	Cr	Ni	Mo	Si	C	Cu	Mn
Alloy Designation:							
100Fe	-	-	-	0.005	0.007	-	0.075
* 3Si	0.010	0.010	-	3.45	0.010	0.10	0.075
8Si	0.008	0.07	>.10	7.89	0.008	0.010	0.01
10Si	0.009	0.08	>.10	9.45	0.007	0.008	0.01
14.5Si	0.01	0.10	>.10	14.12	0.012	0.010	0.01

Elements:	S	P	Al	O (ppm)	N (ppm)	H (ppm)
Alloy Designation:						
100Fe	0.018	0.005	-	-	-	-
3Si	0.018	0.005	0.010	30	33	-
8Si	0.008	0.010	0.010	40	39	-
10Si	0.008	0.010	0.010	46	31	-
14.5Si	0.009	0.010	0.020	49	50	1.4

\*Chemical analysis supplied by Battelle, Columbus, Oh; all other analysis conducted by The Duriron Co, Dayton, Oh.

Alloy:	ATOMIC PERCENT OF Si IN ALLOYS
3Si	6.5%
8Si	14.8
10Si	18.2
14.5Si	24.7

TABLE I (CON'T)

FABRICATION HISTORY AND HEAT TREATMENT

100Fe	Heated to 1200°C for 24 hrs, furnace cooled to 900°C cooled at rate of 100°C for 24 hrs to 600°C and furnace cooled.
3Si	Melted under argon above 1500°C for 10 min; allowed to cool to room temperature in furnace.
8Si	Melted under argon above 1500°C for 20 min; power to furnace was turned down at the rate of 1% power control every 15 min.
10Si	Same as above.
14.5Si	Same as above.



The sample was then taken out of the cell, rinsed with methanol (reagent grade), and carefully broken out of the bakelite holder and clipped onto the Auger sample holder carousel. When the carousel was filled with the samples for analysis, it was lightly doused with methanol and placed in the stainless steel vacuum chamber.

A Physical Electronics Industries, Inc., Model 11-500 Auger System Control unit with an ultra high vacuum system supplied by Varian Vacuum Systems was utilized; the latter system used sorption, ion, and titanium sublimation pumps to attain a pressure in the  $10^{-10}$  torr range.

A brief outline of the Auger analysis procedure is presented here, while the actual Auger results contain the operating parameters for each analysis.

Details of the principles of AES can be found elsewhere (18). But briefly, with AES, the specimen is excited with a focussed electron beam and secondary electrons emitted from the surface as a result of the Auger process are energy analyzed. AES allows high sensitivity analysis of the surface constituents; and when combined with a sputter etching technique, it also allows depth composition analysis.

For the analysis of this work, once the vacuum chamber had reached  $10^{-10}$  torr range, a preliminary surface scan was run. The chamber was then backfilled with prepurified argon to a pressure of  $5 \times 10^{-5}$  torr; the titanium sublimation pump was operated for 75 seconds in five minute cycles to getter the oxygen in the system during the entire analysis period.

After backfilling, the sample was sputter etched at 600V with a current of 25  $\mu$ A, the argon beam sputtered an area 2-3 mm in diameter. The etching was continued for 30 to 60 seconds and then the sample was re-analyzed. The peak heights of the oxygen line (510 eV), the iron line (703 eV), and the silicon line (92 eV) were monitored at each analysis. The sputter/analysis procedure was repeated until the oxygen signal was no longer detected. Figure 3 shows a typical Auger spectrum prior to sputtering; Figure 4 shows the same sample after sputtering some time.

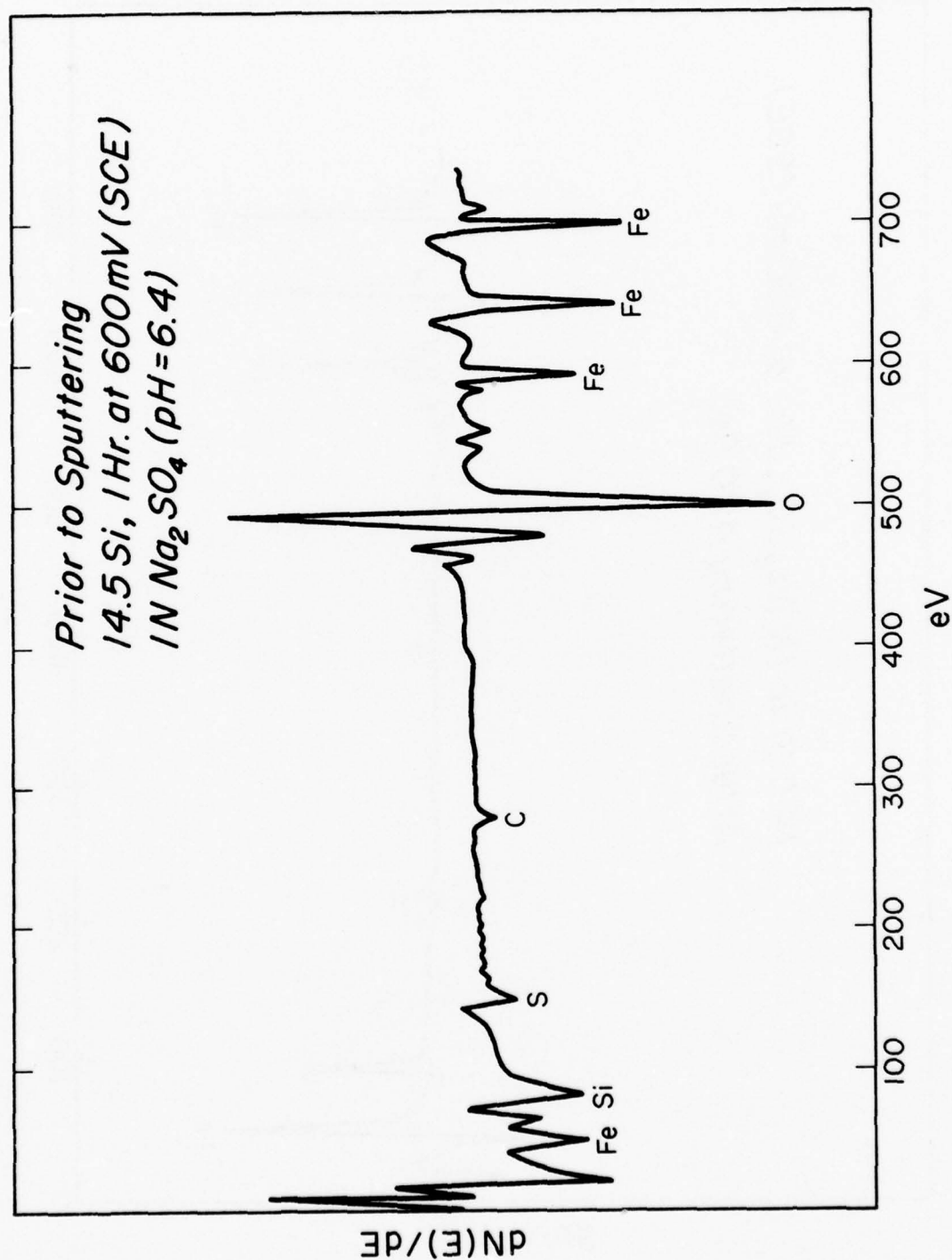


Figure 3. Auger spectrum taken before sputtering. Note large oxygen peak and SiO<sub>2</sub> peak.

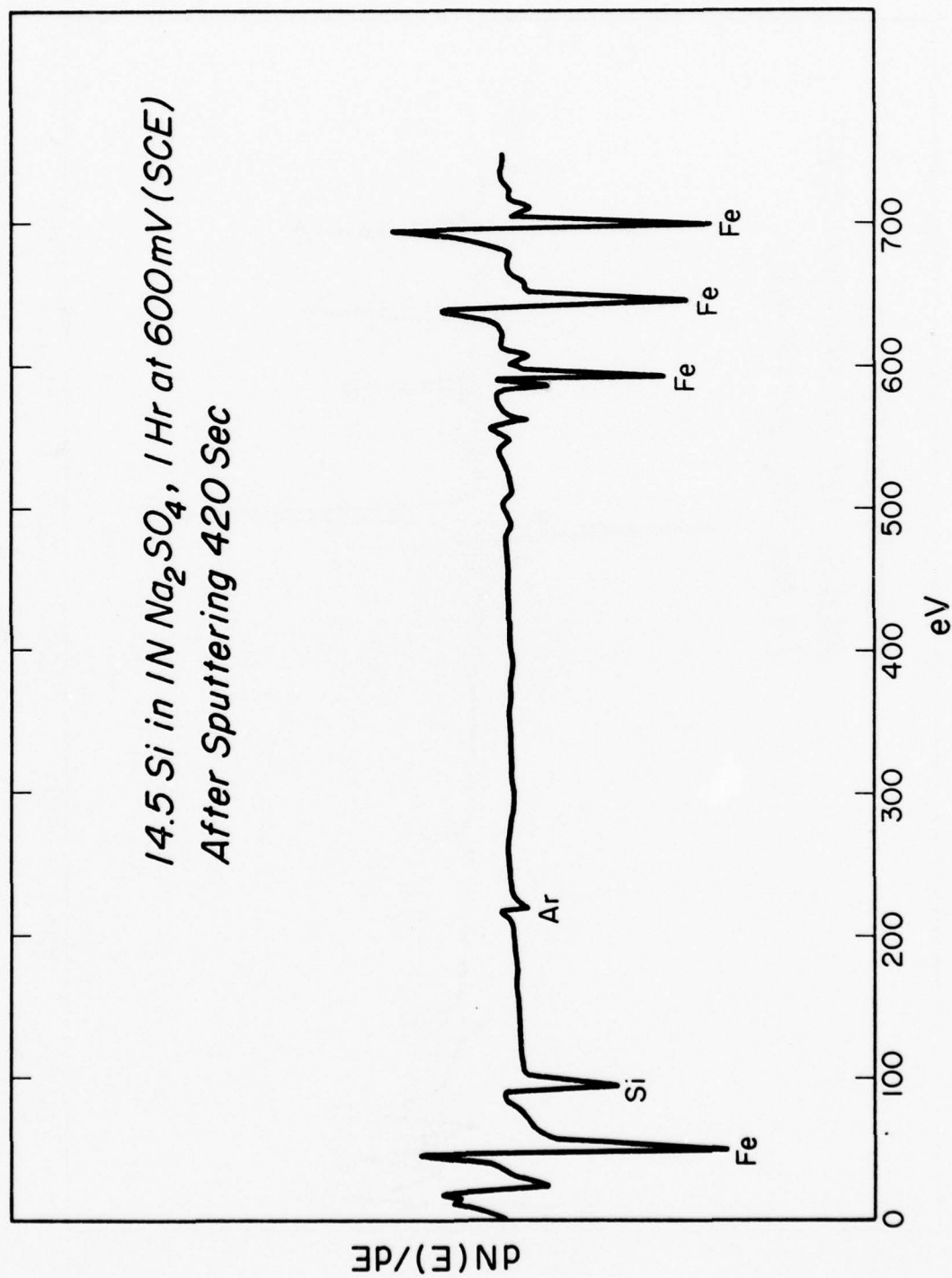


Figure 4. Auger spectrum taken after sputtering. Note disappearance of oxygen peak.

Additional spectral information was obtained by monitoring the low energy iron and silicon peaks at 47, 66, and 92 eV. Seo et al (19) showed that the low energy spectra at various depths changed corresponding to different oxide compositions.

#### 4.0 EXPERIMENTAL RESULTS

##### 4.1 Introduction

The purpose of this investigation was to rationalize the role that silicon plays as an alloying element in influencing the nature of the passive film which forms on iron-silicon alloys in aqueous environments. It has been shown in the literature that silicon has a pronounced beneficial effect on the corrosion properties of iron-silicon alloys when the silicon concentration reaches 14.5 wt %. It was also noted that improved pitting resistance resulted when 2-3 wt % silicon is added to ferritic and austenitic stainless steels. These beneficial aspects of the silicon additions are related to the electrochemical effects of the silicon additions as well as the compositional effects that silicon has on the passive film.

This work is aimed at rationalizing the role that silicon plays as an alloying element with respect to its influence on the composition and the quality of the passive film which forms on the iron-silicon alloys in aqueous environments. With this end, the electrochemical behavior of a series of iron-silicon alloys was investigated in sulfate, borate, and chloride solutions. The composition of the passive films which formed was determined by Auger electron spectroscopy. In an effort to characterize the rate of dissolution, current decay curves were generated in the sulfate solutions. Such results would give the film growth dependence as a function of silicon content, applied potential, and pH.

In this section the experimental results of this study are presented.



## 4.2 Microstructures

The microstructures of the series of alloys used in this investigation are shown in Figures 5a-5d. The alloys are solid solutions of silicon in a ferrite matrix for all compositions. X-ray diffraction analysis indicated only the presence of a single ferrite phase in all the alloys.

An examination of the microstructures shows that the alloys are large grained due to the slow cool down cycle used in their fabrication. Although the 10Si and 14.5Si samples show some evidence of a second phase, x-ray diffraction of the material did not identify it. Dissolution techniques to determine the second phase were not attempted, but should be considered in further work with this alloy system.

## 4.3 Electrochemical Behavior

### 4.3.1 Borate Buffer Solution, pH = 8.4

The polarization curves of the series of binary alloys in 0.15N sodium borate and 0.15N boric acid, pH = 8.4, are shown in Figure 6. The curve of 100Fe compares favorably with that reported by Nagayama and Cohen (20). The effect of silicon is evident in the decrease in the active peak as the silicon content increases. The open circuit potentials,  $E_r$ , are shown in Figure 7. Nagayama and Cohen (20) report the rest potential in deaerated borate buffer as -820 mV, SCE (-580 NHE); this is only slightly more active than the -800 mV, SCE (-560 NHE) reported in this study. Silicon additions less than 14.5% shifted the potentials slightly in the noble direction; the shift in  $E_r$  was not particularly dramatic. 14.5Si shifted  $E_r$  to -760 mV, SCE (-520 NHE).

Also plotted in Figure 7 is the passivation potential,  $E_p$ , vs silicon content. Once again, silicon contents less than 14.5% shifted  $E_p$  in the noble direction. Although a passivation potential is plotted for the 14.5Si sample, there is some doubt as to the existence of truly active-passive behavior in this alloy, as is evident from the lack of a significant active peak in the polarization curve of this alloy.

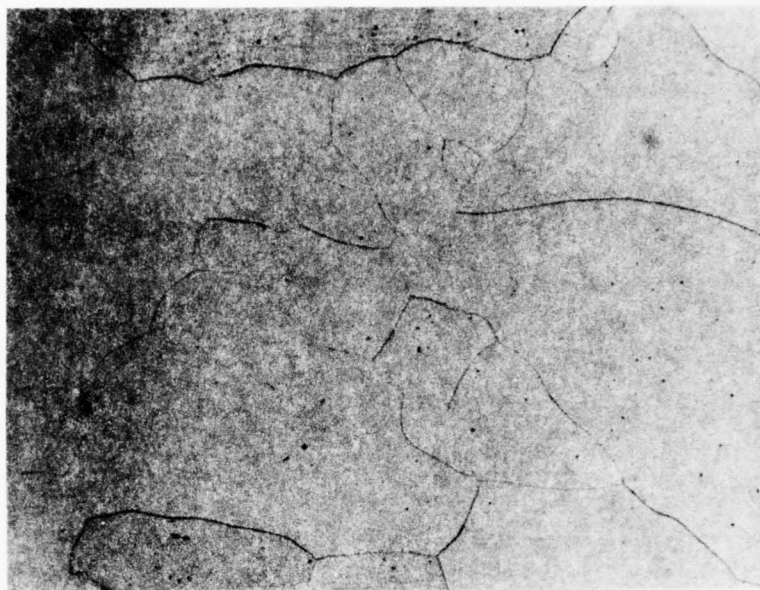


Figure 5a. Microstructure of 100Fe sample (nital etch, 100X).

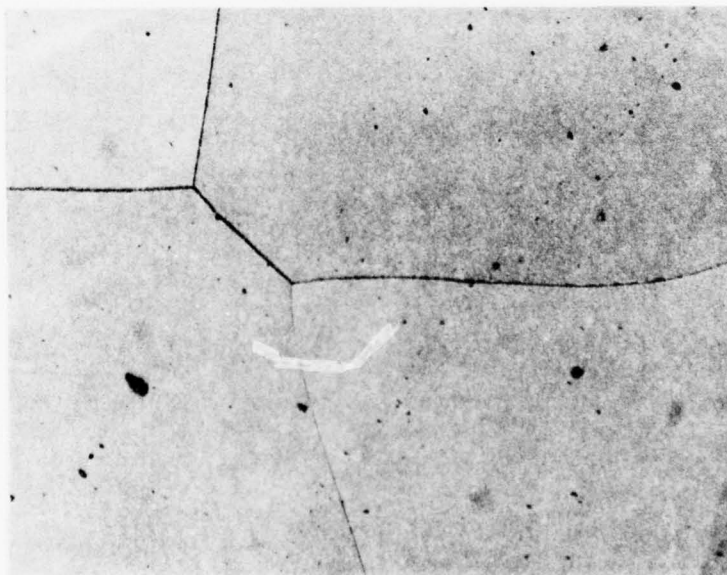


Figure 5b. Microstructure of 3Si sample (nital etch, 100X).

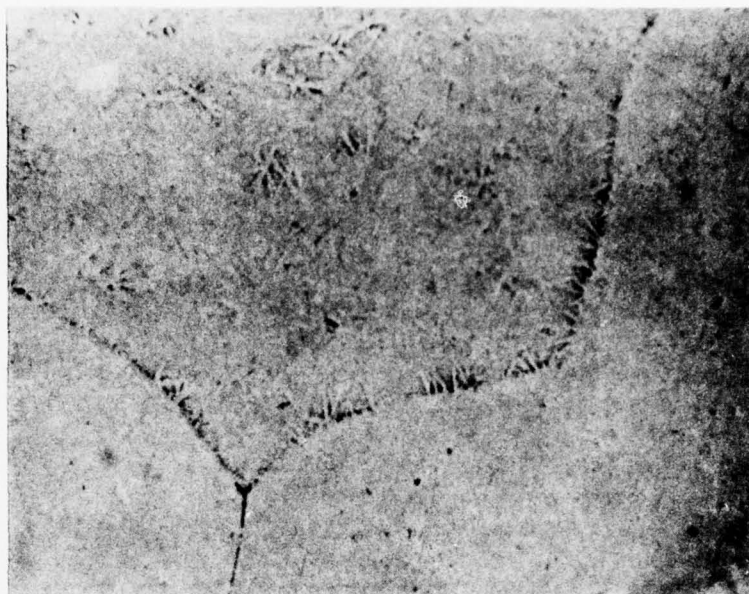


Figure 5c. Microstructure of 8Si sample (mixed acids/glycerol etch, 100X).

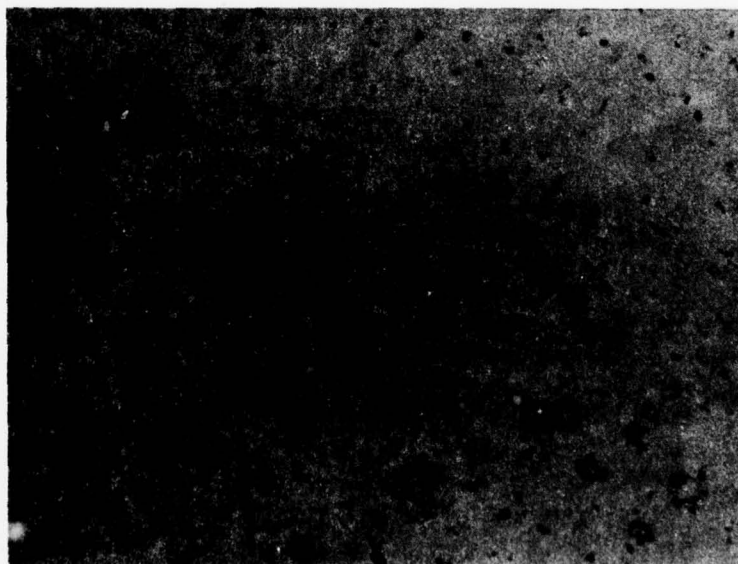


Figure 5d. Microstructure of 10Si sample (mixed acids/glycerol etch, 100X).

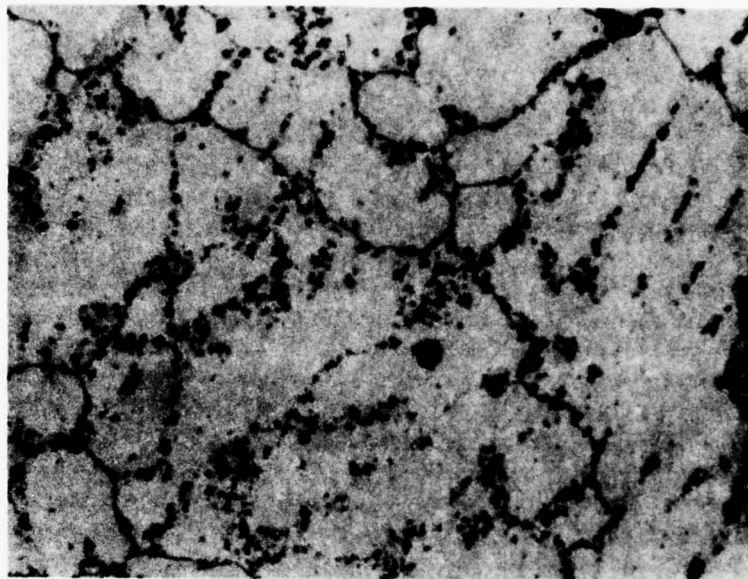


Figure 5e. Microstructure of 14.5Si sample (mixed acids/glyceral etch, 500X).

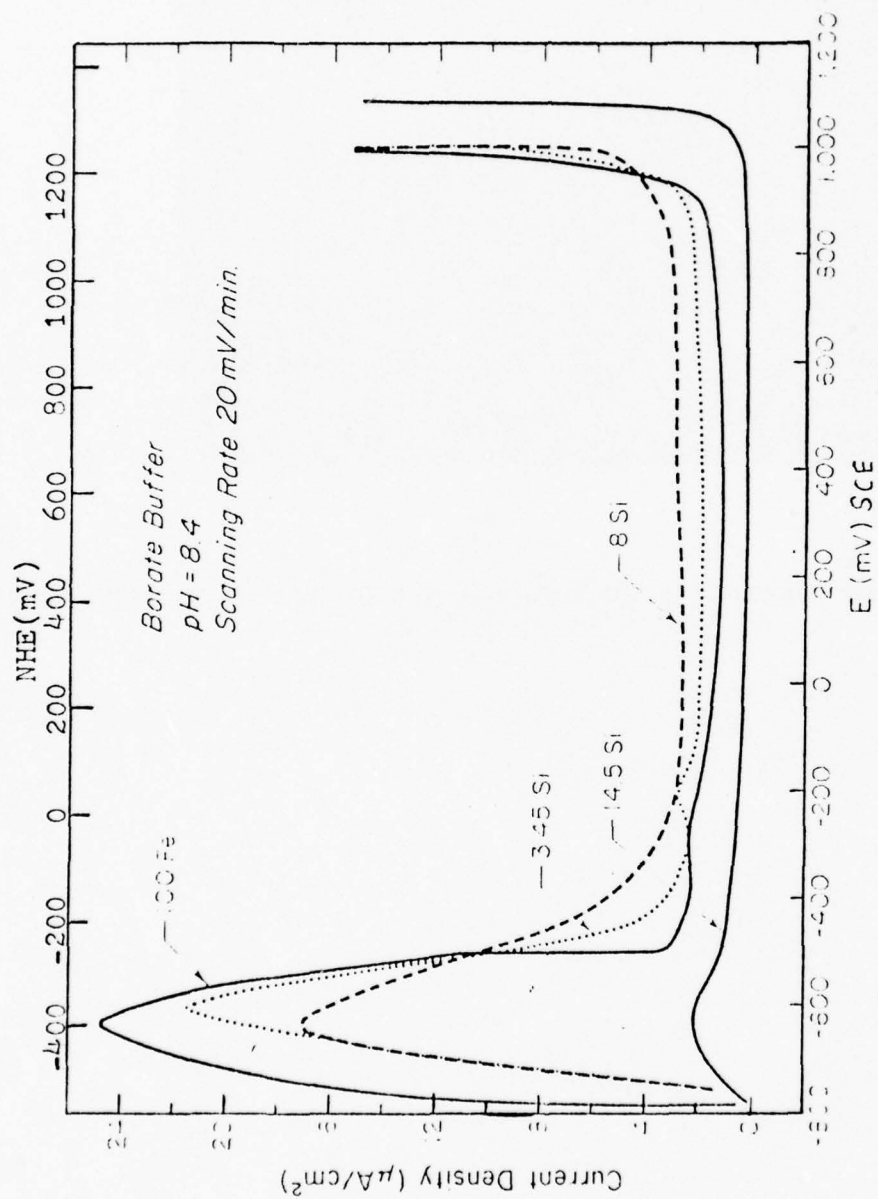


Figure 6. The polarization curves of Fe-Si Alloys in a borate buffer solution (pH = 8.4).



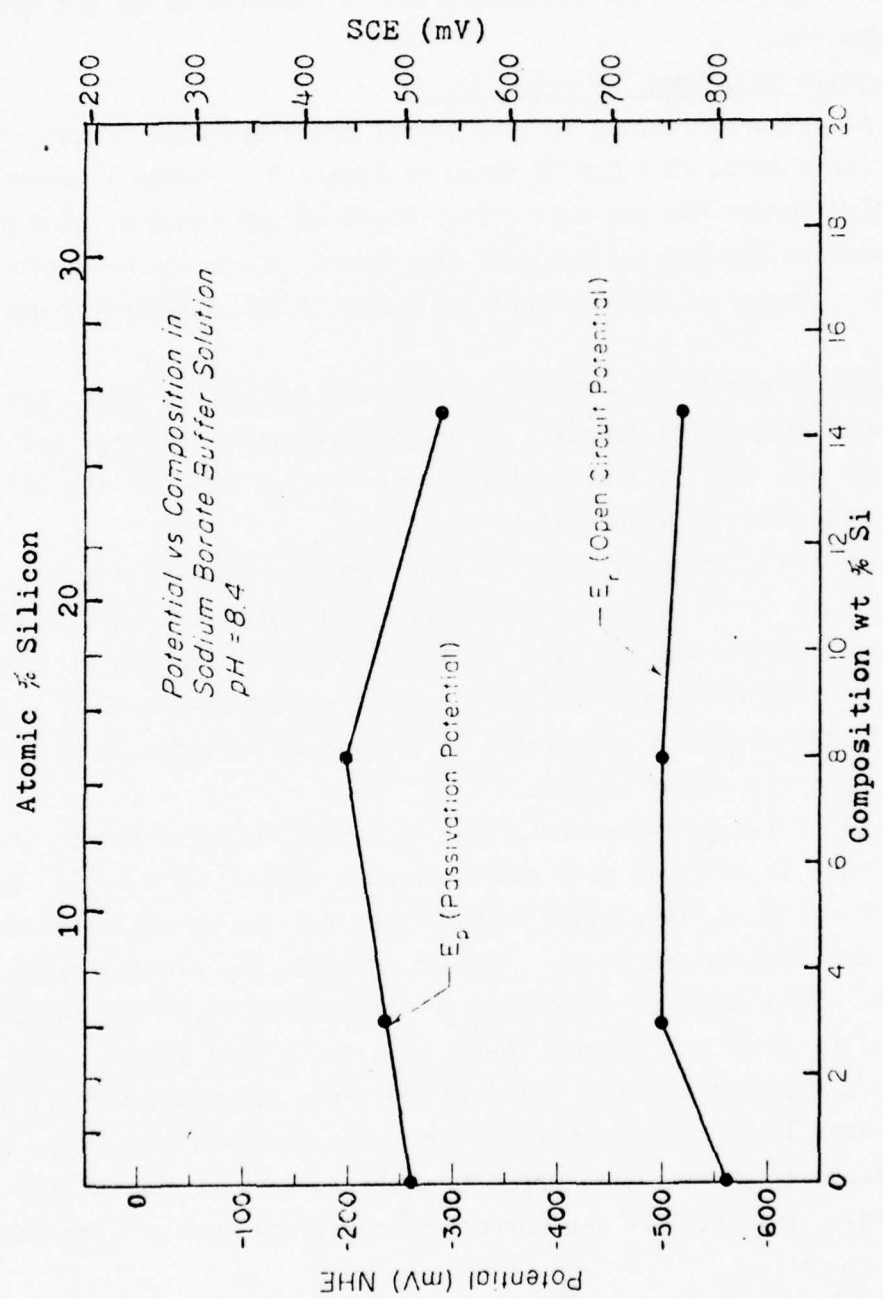


Figure 7. The open circuit and passivation potential (NHE) vs silicon content in a borate buffer solution.

The active current vs silicon content is plotted in Figure 8 where the decrease in active current from  $\sim 25 \mu\text{A}/\text{cm}^2$  for 100Fe to  $\sim 2 \mu\text{A}/\text{cm}^2$  for 14.5Si. Also on this figure is plotted the passive current densities where the effect of silicon content is not as dramatic as on the active current density.

#### 4.3.2 Sulfate Solutions (pH = 0.4 to 14)

The polarization curves for the series of alloys used in this study in 1N sulfuric acid, pH = 0.4 is shown in Figure 9. Figure 10 shows the polarization curves for the same alloys in 1N sodium sulfate, pH = 3.2. With respect to the general shape of the curves, there was no great effect noted with changing silicon content until the 14.5Si composition was reached.

Figures 11 and 12 show the polarization curves in 1N sodium sulfate, pH = 6.4 and 10.3, respectively. Although passivation occurred for the alloys with less than 14.5 wt % silicon, the active peaks of the 3Si and 8Si alloys were higher than that of pure iron.

A porous film formed at the limiting current values on the low silicon alloys; it is evident from the polarization curves that it was stable over a wide potential range of 500 to 750 mV. Economy et al (21) observed a porous film range for iron in sulfuric acid with  $-0.47 \leq \text{pH} \leq 3.73$ . The polarization behavior documented in this study for iron in pH = 0.4 and 3.2 agrees with their curves.

Crow et al (9) generated polarization curves for a series of iron-silicon alloys in sulfuric acid solutions with  $-1.07 \leq \text{pH} \leq 1.09$ . In the 1N sulfuric acid, they found a wide range for the porous films which formed at the limiting currents. For 3Si and 8Si, the plateau range was 700-800 mV. They recorded no plateau or porous film stability region for 15Si alloy which corresponds to the results in this study.

Current fluctuations were noted in all these solutions for all alloys with less than 14.5% silicon when the samples approached passivity. These current fluctuations have been noted by other workers in the sulfate system (22, 23, 24). In this work the current fluctuations went off the scale

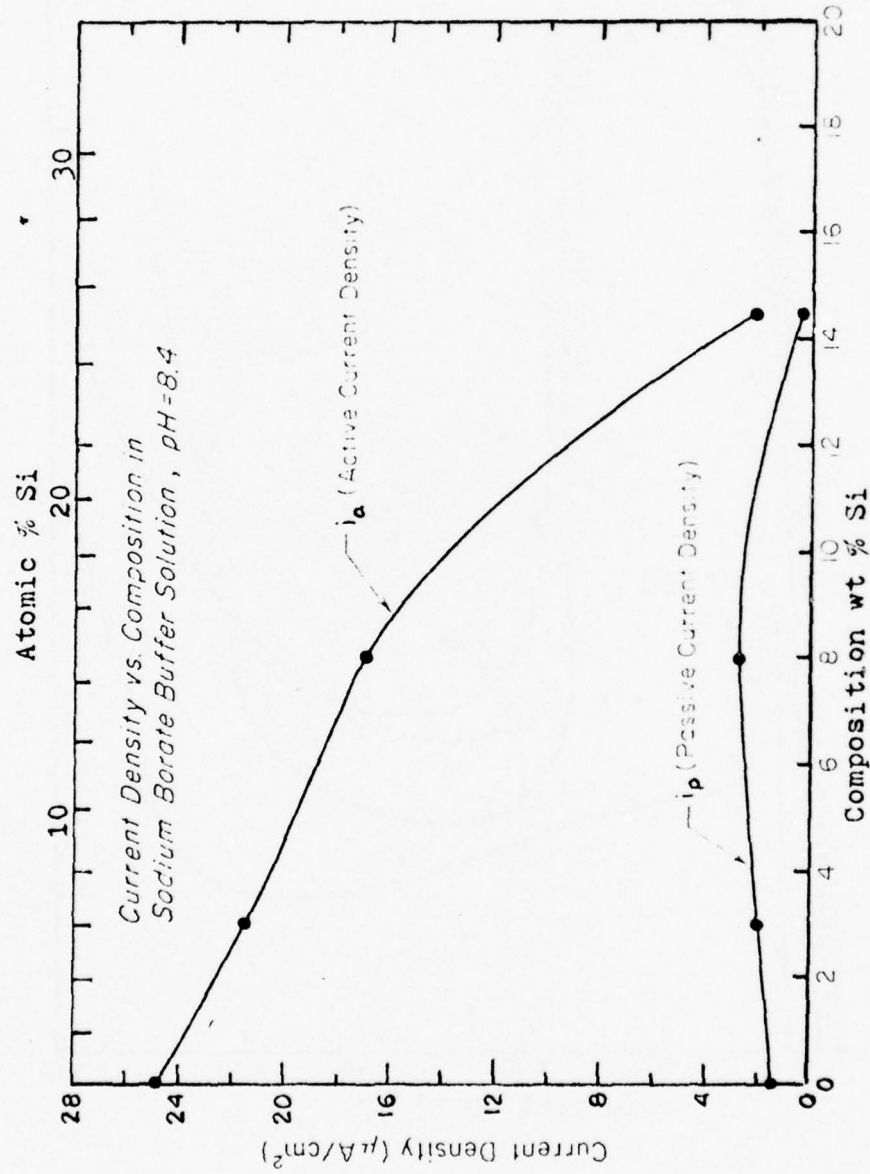


Figure 8. The passive and active current density vs silicon content in a borate buffer solution.



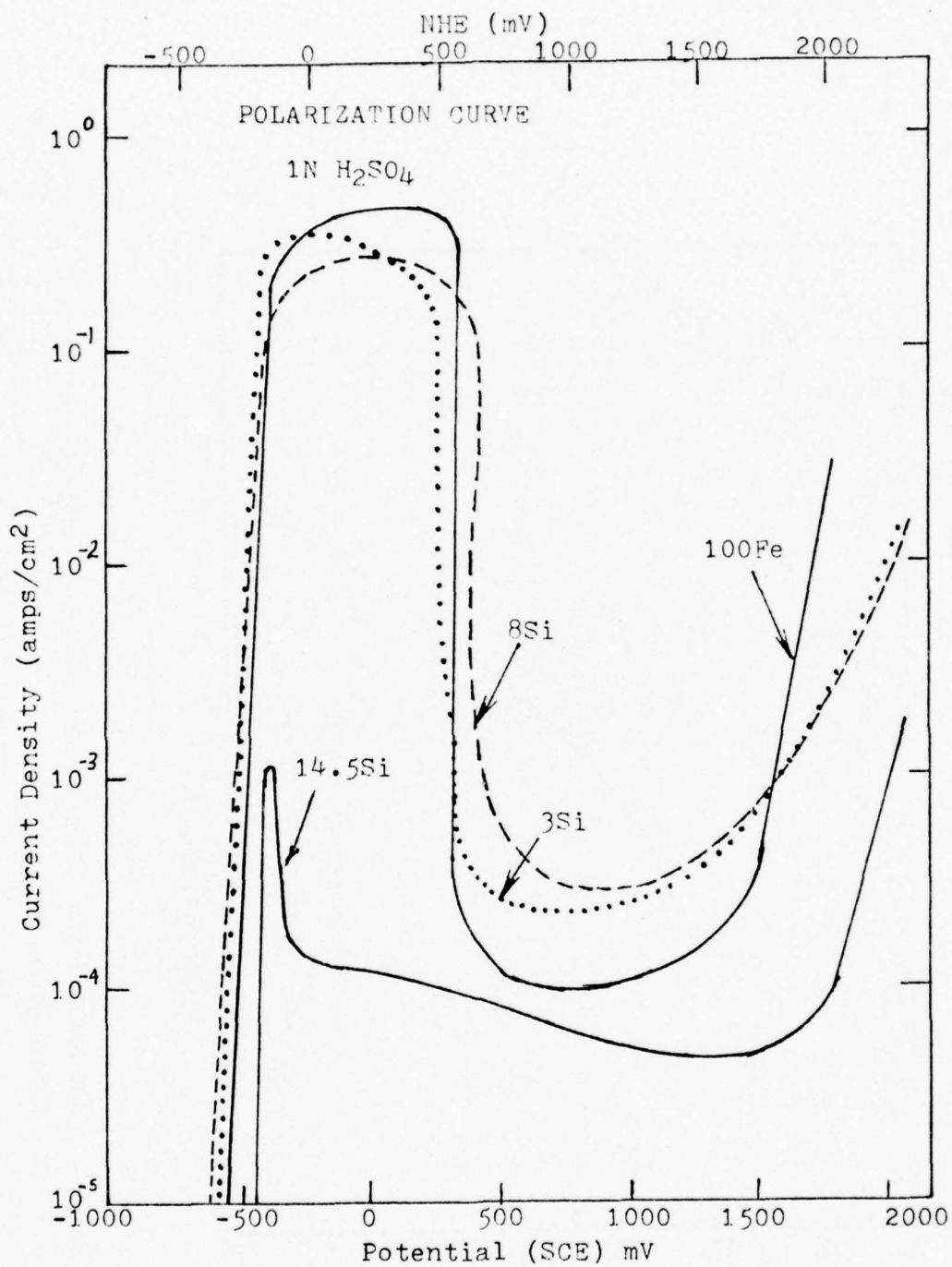


Figure 9. Polarization curve of iron-silicon alloys in 1N H<sub>2</sub>SO<sub>4</sub>, pH = 0.4 (scanning rate 50 mV/min.).

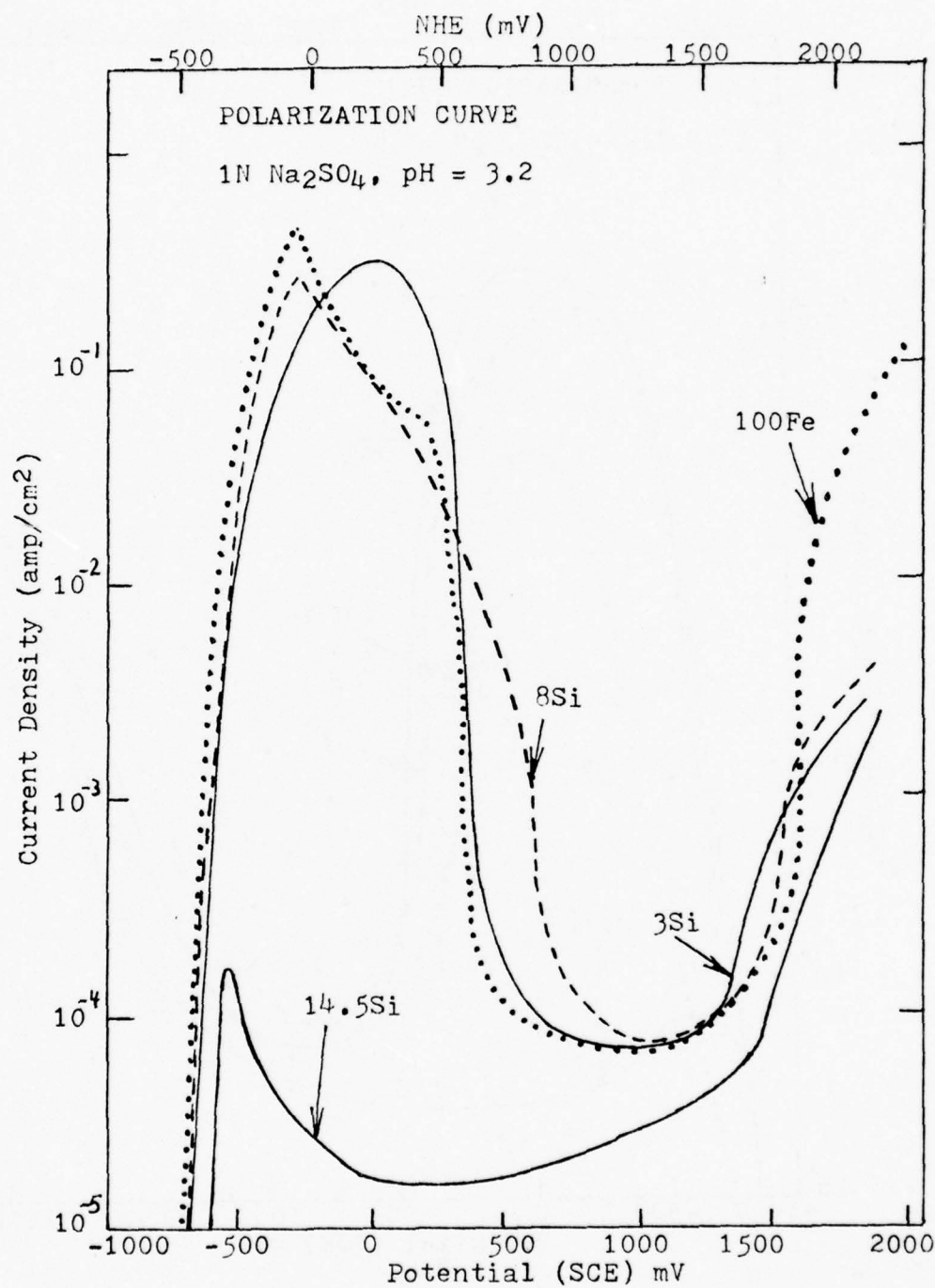


Figure 10. Polarization curves for iron-silicon alloys in 1N Na<sub>2</sub>SO<sub>4</sub>, pH = 3.2 (scanning rate 50 mV/min.).

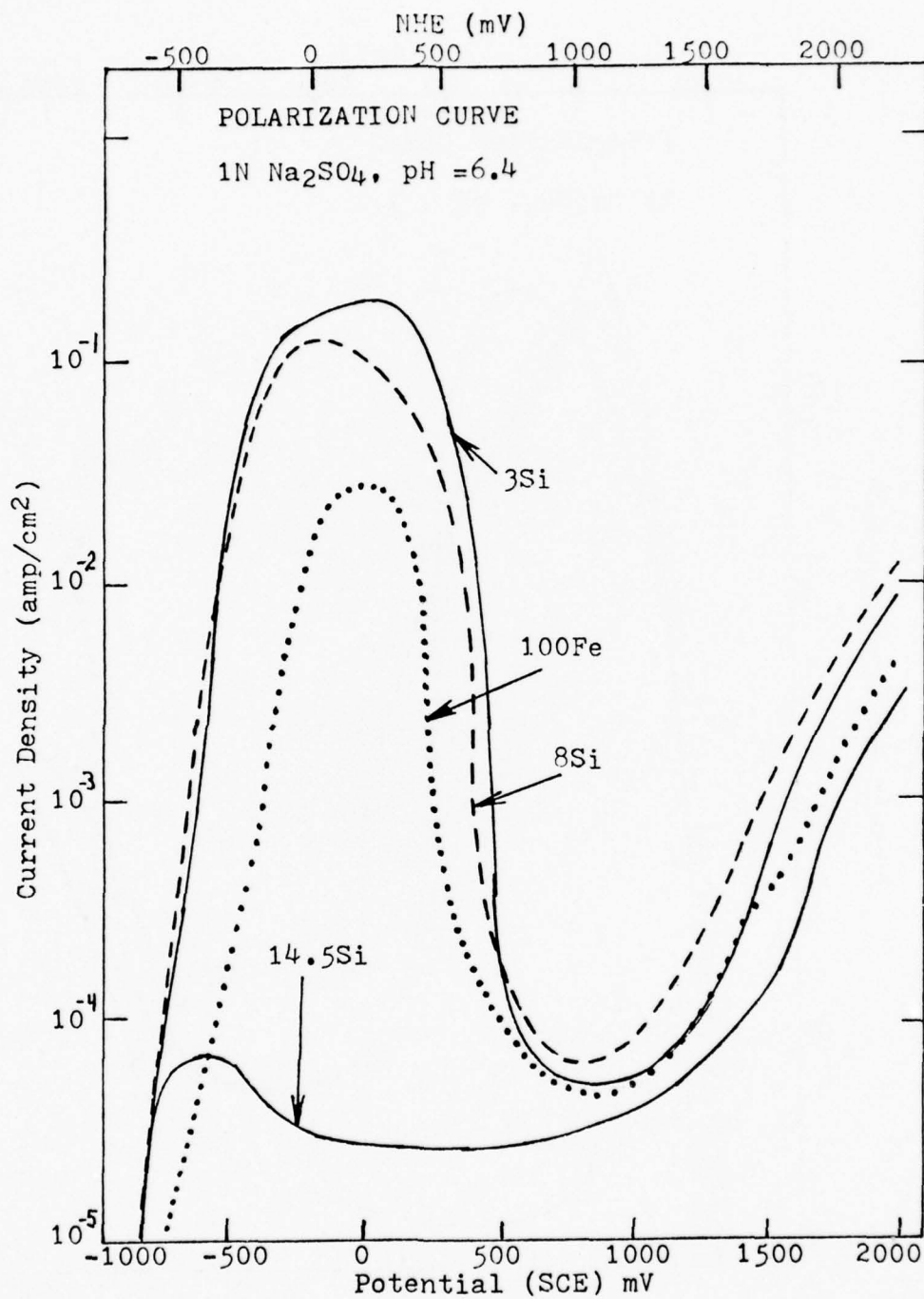


Figure 11. Polarization curves for iron-silicon alloys in 1N Na<sub>2</sub>SO<sub>4</sub>, pH = 6.4 (scanning rate 50/mV/min.).

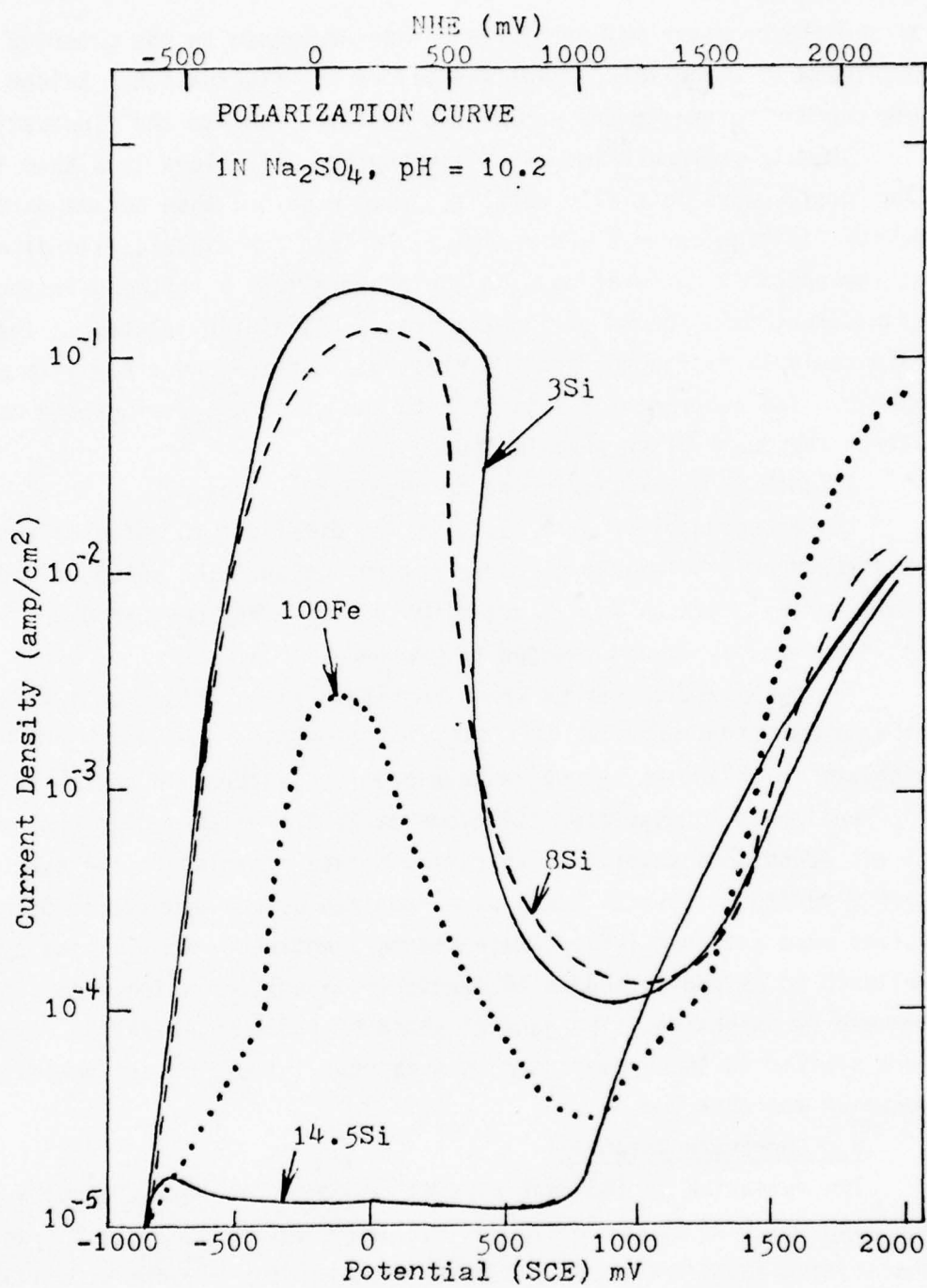


Figure 12. Polarization curves for iron-silicon alloys in 1N Na<sub>2</sub>SO<sub>4</sub>, pH = 10.2 (scanning rate 50 mV/min.).

of the electrometer momentarily and then decreased to the order of magnitude at which the current was before the fluctuation. Seldom did the current return to the same value it held prior to the fluctuation.

Visible surface films were observed for all alloys less than 14.5 Si. The samples were initially metallic gray in color, then became darker as the limiting current was reached. In iron the visible film disappeared at the onset of passivation. On the other alloys a thick, gelatinous, transparent film formed during the active dissolution plateau. The film could be dislodged from the electrode surface and a new film would appear. The adherence of this film to the electrode surface did not affect the passivation reaction potential.

No such porous films formed on the 14.5Si alloy.

In the solution of pH = 10.3, it was difficult to maintain a stable pH throughout a polarization curve determination. The solution would start at the above pH value, but after a sample had been anodically polarized in the solution, the pH changed to as low as 9.0.

The polarization curves shown in Figure 13 in 1N sodium sulfate, pH14 proved to be the most difficult to reproduce. Such reproducibility problems in 1N sodium hydroxide have been encountered in past studies (25, 26). In experiments in deaerated solutions at 25°C of 0.2M sodium hydroxide, it was found that several polarization curves recycled in the same solution over a period of several weeks were required before consistent polarization curves were attained (26). These inconsistencies in the initial cycles were believed to be due to traces of reactable impurities which were slowly removed by oxidation. The general shape of these polarization curves on iron were similar to those generated in this study, i.e., no active-passive behavior was observed.

#### A. Corrosion Potential

The variation in the open circuit or corrosion potential with pH for each alloy is shown in Figure 14. There was no consistent trend of the silicon additions on  $E_p$ . Similar inconsistent effects of silicon on the corrosion potential have been found by workers in deaerated sulfuric acid (9, 10). However, at 14.5Si,  $E_p$  shifted significantly in the noble



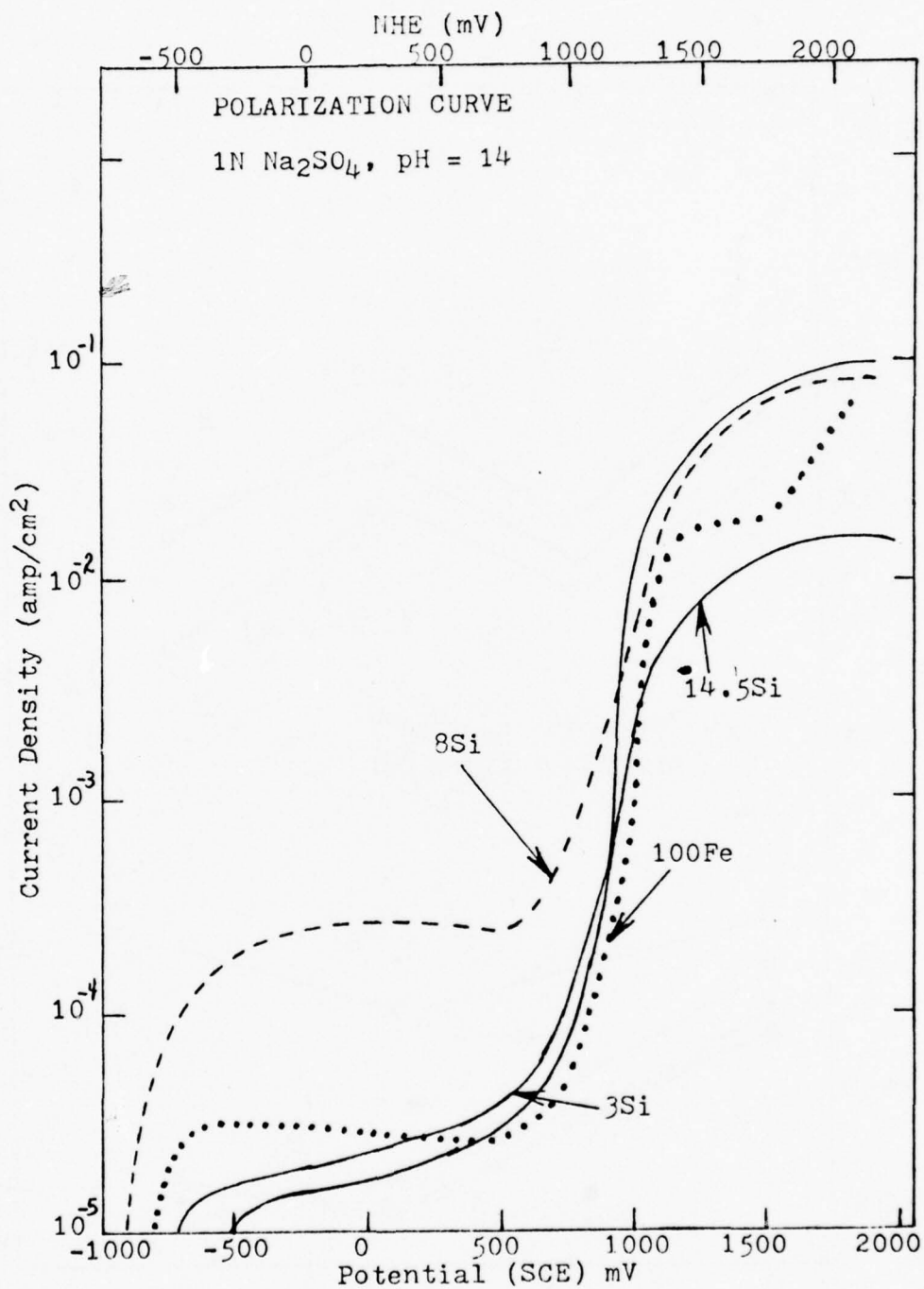


Figure 13. Polarization curves for iron-silicon alloys in 1N Na<sub>2</sub>SO<sub>4</sub>, pH = 14 (scanning rate 50 mV/min.; pH adjusted with NaOH).

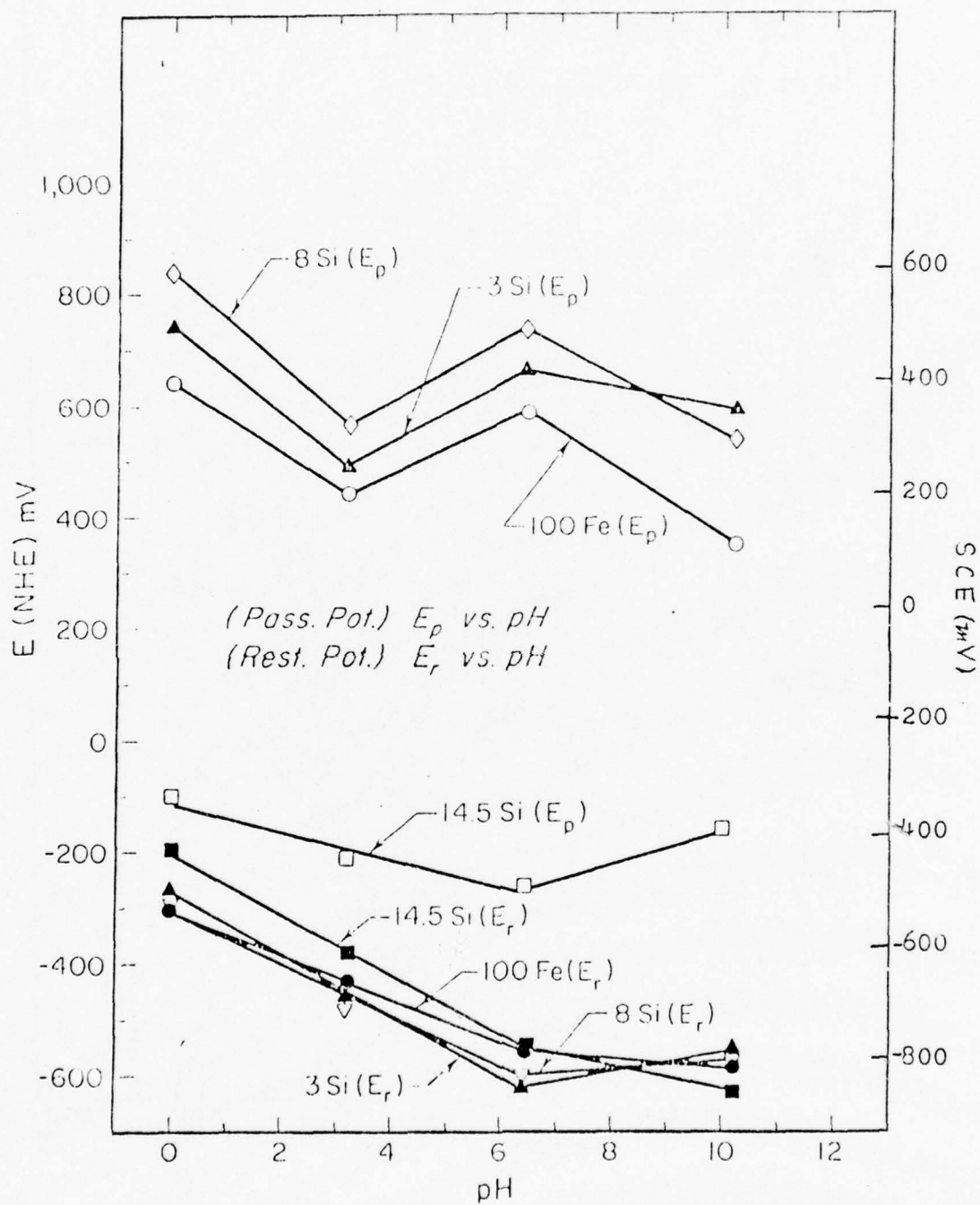


Figure 14. The open circuit and passivation potential vs solution pH for iron-silicon alloys in sulfate solutions.

direction with respect to the iron sample and remained more noble for solutions with  $\text{pH} < 10.3$ . At the higher pH,  $E_r$  for 14.5Si become more active than that of iron. Table II lists the linear relations between  $E_r$  and pH as plotted on Figure 14 for  $\text{pH} < 7$ .

#### B. Passivation Potential

The passivation potential for each alloy as a function of pH is plotted in Figure 14. The effect of 3Si and 8Si is to shift the potentials in the noble direction. Table III lists the linear relationships between  $E_p$ , the passivation potential, and pH for the alloys divided into three areas:  $\text{pH} < 3$ ,  $3 < \text{pH} < 7$ ,  $\text{pH} > 7$ . A comparison among the 100Fe, 3Si, and 8Si shows that the slopes of these expressions are similar.

#### C. Active and Passive Current Densities

Figure 15 shows the plot of the active current density vs pH for each alloy as well as the respective variation in passive current density. For  $\text{pH} \leq 6.4$ , the height of the active peak decreased as the pH increased. At  $\text{pH} = 10.3$ , the active current value increased. The same general trends were followed by the passive current densities.

The effect of increasing silicon content in the alloys was to increase both the active and the passive current densities; however both values did decrease significantly in the 14.5Si alloy. Similar effects have been noted by other workers (9, 10) in sulfuric acid.

#### 4.3.3 Borate Buffer + 0.1M Potassium Chloride

To study the effect of chloride in a system where the alloys were known to have active-passive behavior, a 0.1M potassium chloride addition was made to the borate buffer. Figure 16 shows the polarization curves for the alloys in this solution. Listed on this figure are also the pitting potentials determined by using the scratch technique previously described. The value obtained for 100Fe was -215 mV SCE (+25 mV NHE). Janik-Czachor (27) obtained a pitting value of -160 mV SCE (+80 mV NHE) in this same solution; this value was obtained using the galvanostatic technique. Pitting values have been found to show a wide variation (28)

TABLE II

OPEN CIRCUIT POTENTIAL (NHE) - pH RELATIONSHIPS  
(pH < 7) FOR SULFATE SOLUTIONS

Alloy	$E_r$ Expression
100Fe	$-0.306 - 0.039 \text{ pH}$
3Si	$-0.274 - 0.055 \text{ pH}$
8Si	$-0.301 - 0.048 \text{ pH}$
14.5Si	$-0.205 - 0.055 \text{ pH}$

TABLE III

PASSIVATION POTENTIAL (NHE) - pH RELATIONSHIPS  
FOR SULFATE SOLUTIONS

Alloy	$E_p$ pH < 3	$E_p$ 3 < pH < 7	$E_p$ pH > 7
100Fe	$0.64 - 0.06 \text{ pH}$	$0.29 + 0.05 \text{ pH}$	$0.99 - 0.06 \text{ pH}$
3Si	$0.74 - 0.08 \text{ pH}$	$0.32 + 0.05 \text{ pH}$	$0.78 - 1.0 \text{ pH}$
8Si	$0.84 - 0.08 \text{ pH}$	$0.39 + 0.05 \text{ pH}$	$1.07 - 0.05 \text{ pH}$
14.5Si	$-0.10 - 0.02 \text{ pH}$		$-0.45 + 0.03 \text{ pH}$

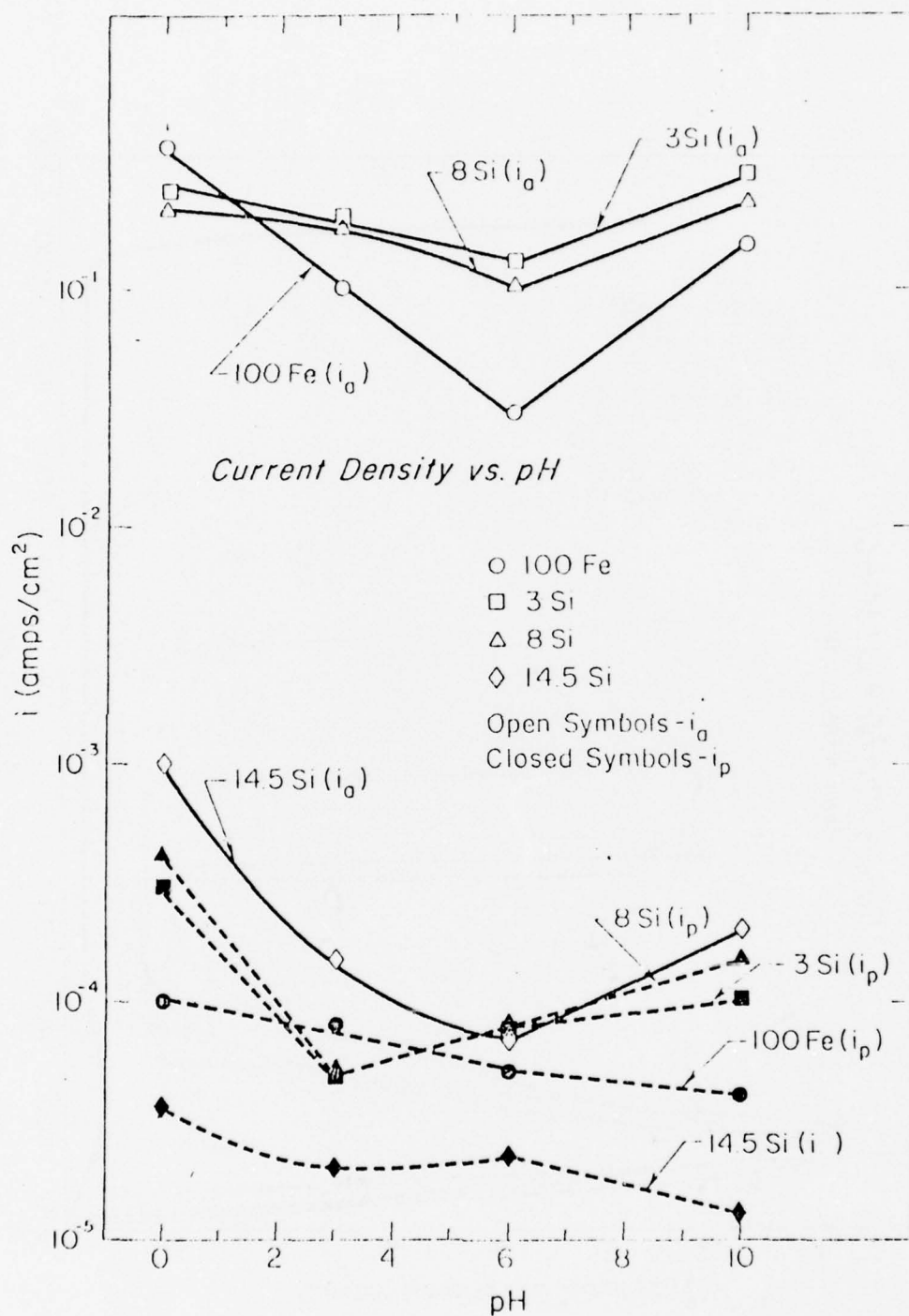


Figure 15. The passive current density and active current vs pH of Fe-Si alloys in the sulfate solutions.



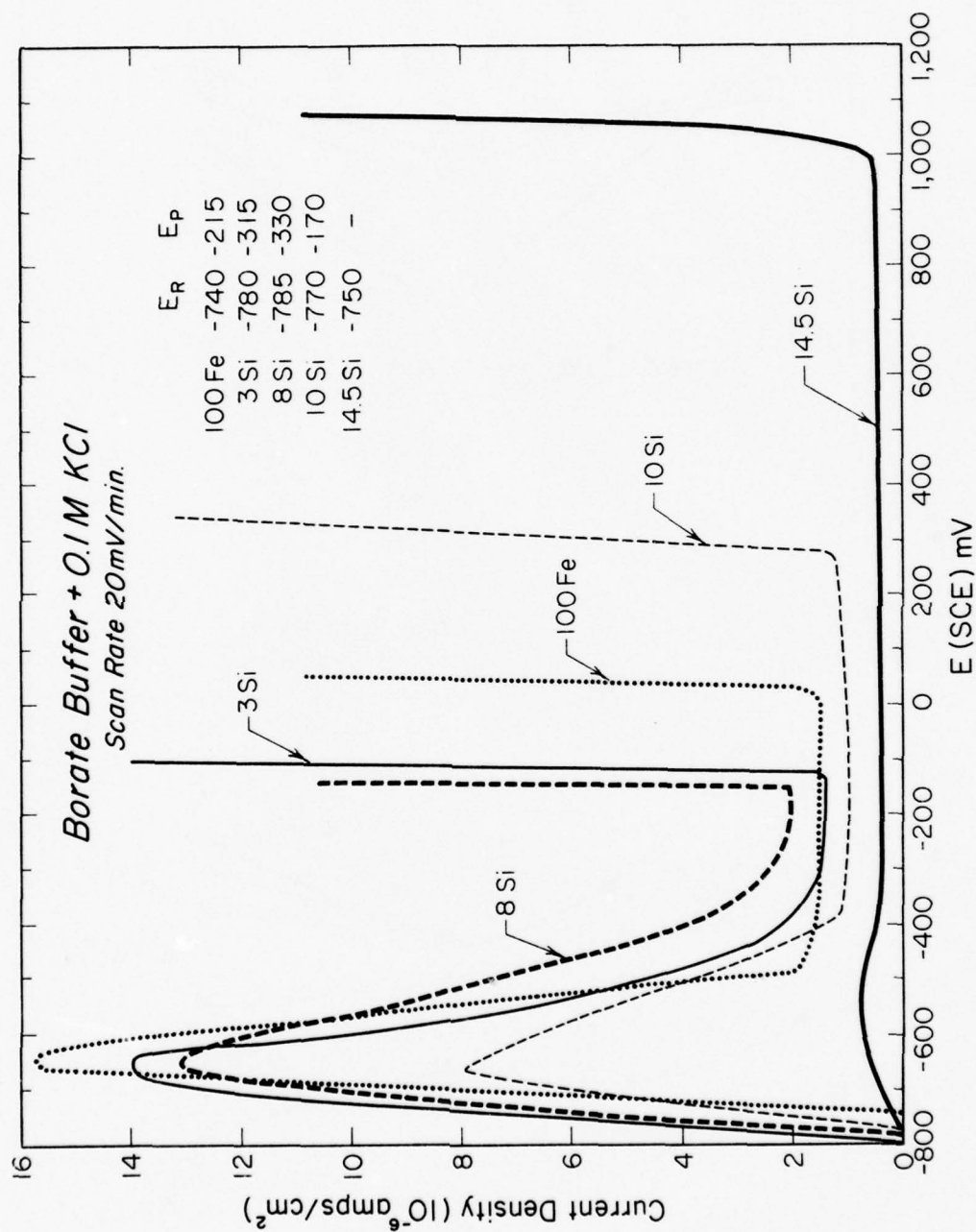


Figure 16. Polarization curves of iron-silicon alloys in borate buffer with potassium chloride.

depending on the method used to determine them. No values of pitting potentials on pure iron determined by the scratch method could be found reported in the literature.

The effect of the silicon content on the pitting potential was not consistent. Figure 17 shows the variation of this potential with silicon content. At concentrations of 3 and 8 wt %, the pitting potential shifted toward values more active than that of iron. At 10 wt % the potential moved to a value more noble than that of iron. No pitting potential was determined for the 14.5Si alloy since no pits formed in this alloy. Tajima et al also found that this alloy did not pit in chloride environments (10).

Figure 18 shows the typical pits obtained in pure iron. These pits are similar to those observed by Vetter and Streblow (29) and Janik-Czachor (27).

Figure 19 shows typical pits formed in the silicon alloys. Material appears to have flowed from the pit and etched the surrounding area. Similar "flow" patterns have been observed for iron-molybdenum (30).

#### 4.3.4 0.1N and 0.5N Sodium Chloride

The polarization curves for the alloys in 0.1N sodium chloride are shown in Figure 20. No active-passive behavior was noted in the iron, 3Si and 8Si samples. Figure 21 shows the polarization curve for the same alloys in 0.5N sodium chloride solution, pH = 6.5. The curves resemble those in 0.1N sodium chloride; no active-passive behavior was noted. This result opposes that noted by Semino and Galvele (31) who detected a narrow passive region for pure iron in neutral 0.5N sodium chloride. No active-passive behavior could be obtained in this work despite the fact that the potential was manually stepped in 20 mV increments and held until the current reached a steady value. The time between potential steps ranged from 30 min to 3 hours. No current decrease could be detected.

#### 4.3.5 1N Hydrochloric Acid

The polarization curves for the binary alloys in 1N hydrochloric acid are shown in Figure 22. The solution had a pH = 0.4. The lower

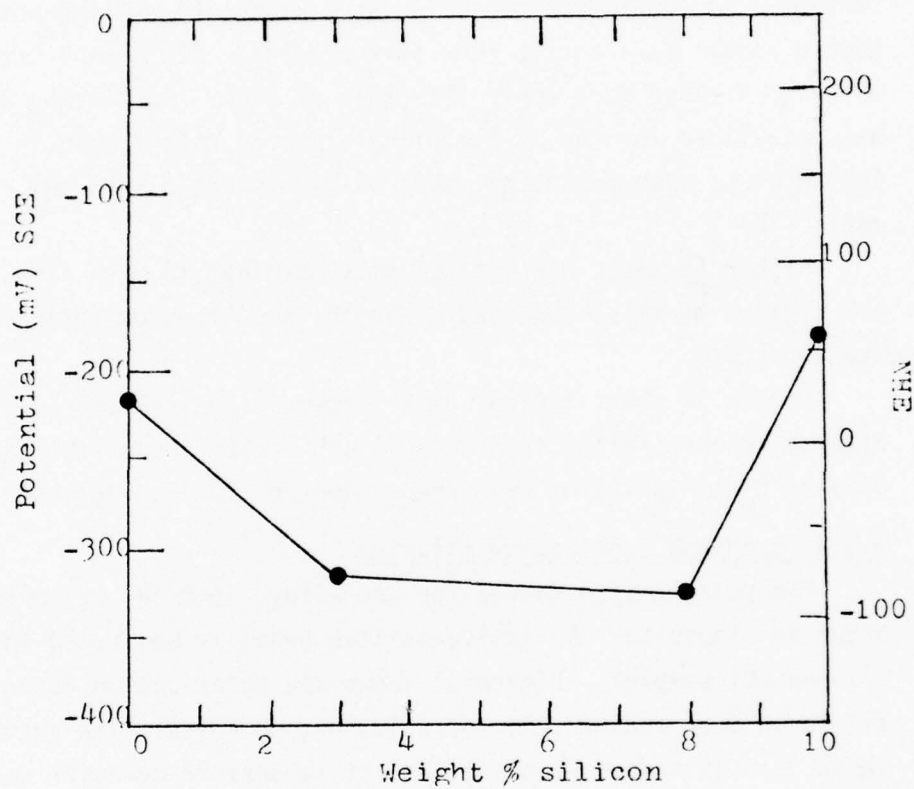


Figure 17. Pitting potential for iron-silicon alloys in borate buffer and 0.1M potassium chloride determined by the "scratch technique."

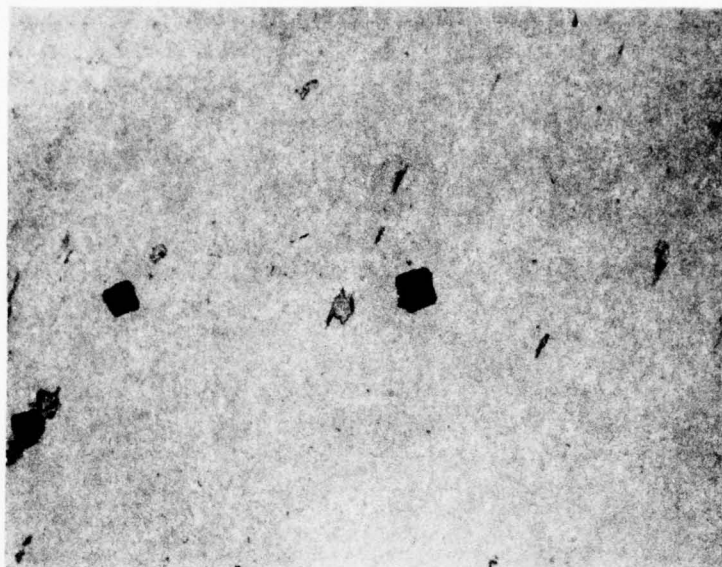


Figure 18. Example of pits which formed on iron in borate buffer and 0.1M potassium chloride (200X).



Figure 19. Example of pits which formed on 3Si in borate buffer and 0.1M potassium chloride (150X).

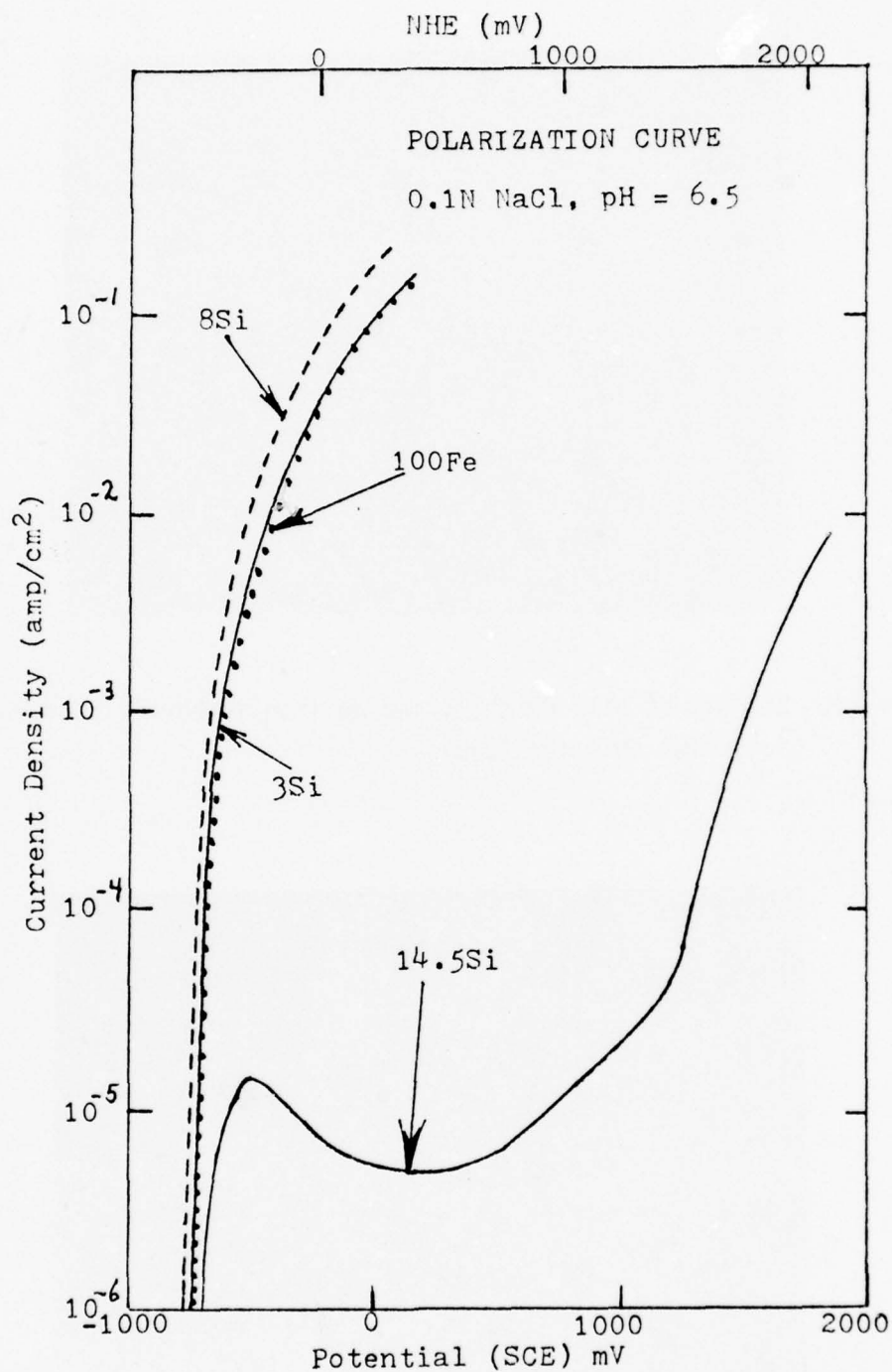


Figure 20. Polarization curve of iron-silicon alloys in 0.1N NaCl (scanning rate 20 mV/min.).



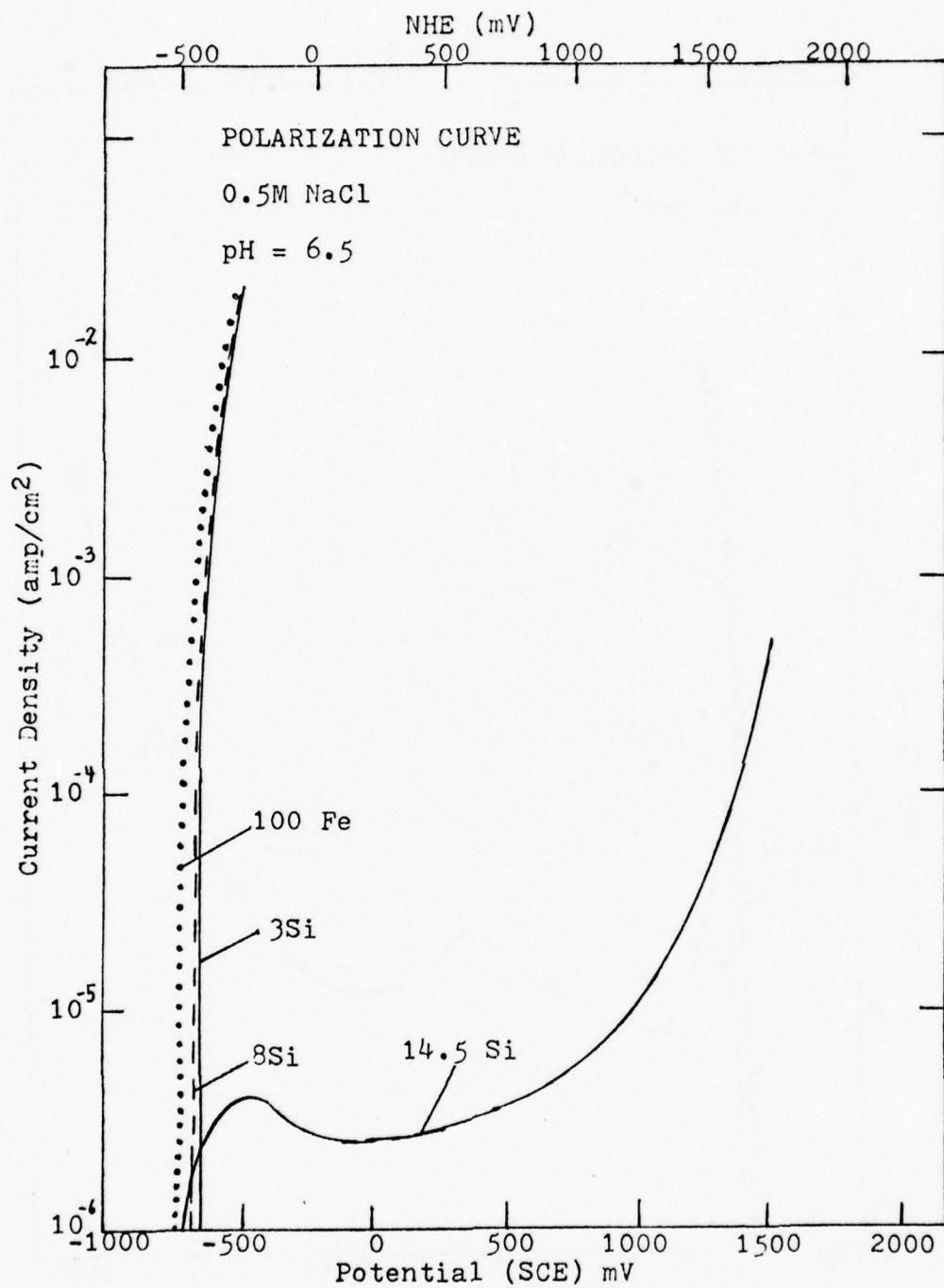


Figure 21. Polarization curve of iron-silicon alloys in 0.5M NaCl; the potential was held until the current reached a steady value.

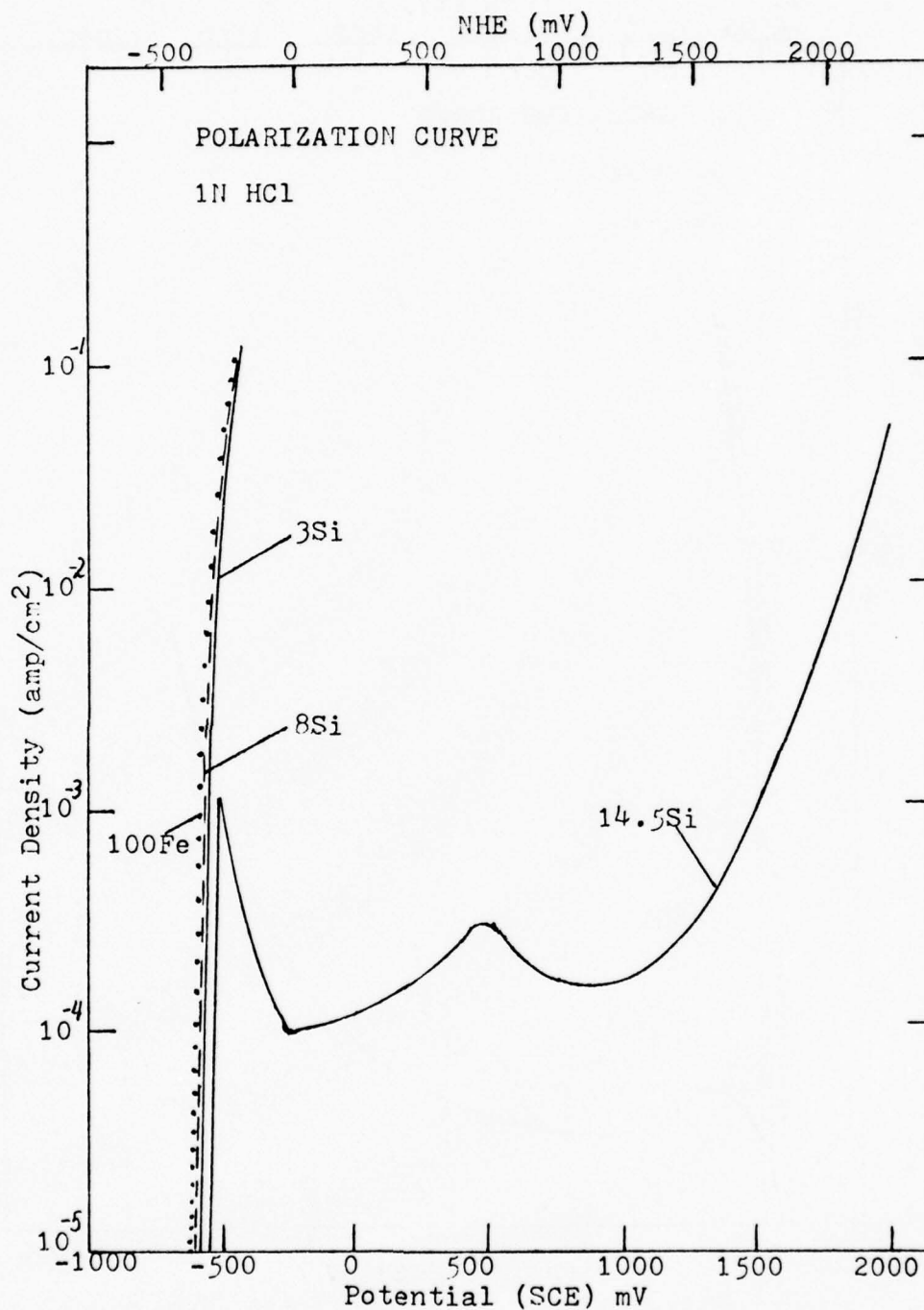


Figure 22. Polarization curve of iron-silicon alloys in 1N HCl (scanning rate 50 mV/min.).

silicon samples had no active-passive behavior while the 14.5Si alloy did passivate. The passive current density, however, was an order of magnitude greater than that in the sodium chloride solutions. Other studies (10) have shown that the effect of chloride appears as the continuous increase of the passive current density with increasing chloride concentration without being accompanied by pitting.

#### 4.4 AES Film Composition Results

##### 4.4.1 Introduction

The compositions of the anodic films formed in the previously discussed electrolytes were determined by Auger electron spectroscopy (AES). Each of the samples to be examined was held at a specified potential for one hour and then placed in the vacuum chamber.

The composition profiles of all the films analyzed were determined in an identical manner. For each sample an Auger spectrum was determined initially and the peak to peak height (pph) for each component detected in the oxide film was monitored as the film was sputtered. To eliminate experimental errors caused by fluctuations of the Auger operating conditions, the observed pph of each component or element was normalized as a ratio to the sum of the pph's of iron and silicon. This ratio was then plotted vs sputtering time, thus developing a composition profile of the film.

In order to sort out the silica and the silicon contributions, the low energy lines (62 and 92 eV) of the spectra were used. Silicon generates high energy lines on the spectra, but these were not used to determine composition because the escape depth of these Auger electrons was several times greater than the iron 703 eV electrons which were the highest energy used.

However, by using the low energy lines it was possible to distinguish a peak at 66 eV associated with  $\text{SiO}_2$  and a stronger peak at 84 to 92 eV associated with silicon. The pph of both of these lines were used to determine the composition profiles. These lines are shown in Figure 3; the disappearance of the  $\text{SiO}_2$  peak is noted in Figure 4 after sputtering.

The disappearance of the  $\text{SiO}_2$  line is accompanied by a shift and an increase in the silicon peak seen in this figure at 92 eV; this peak is associated with the uncombined silicon in the alloy.

The inserts which appear in the Auger composition profiles show the changes in the low energy spectra of the alloys. These spectra resulted from transitions involving valence band electrons; except for the 66 eV and 92 eV lines, the Auger lines used to determine the film compositions resulted from inner level transitions and remained unchanged in energy and shape. The change in the low energy spectra of iron suggest the valence state of iron in the film (32).

#### 4.4.2 Air Formed Films

Figures 23-26 show the Auger composition profiles of films which formed after the alloy samples were polished through 0.05  $\mu\text{m}$  alumina, dried, exposed to ambient air for 24 hours, and then placed in the Auger vacuum chamber for analysis.

Plotted on the figures are the normalized ratios for the oxygen line (510 eV), silicon,  $\text{SiO}_2$ , and iron. No  $\text{SiO}_2$  was observed on the 3Si sample but it was observed on the other samples.

The oxygen decreases continuously with sputtering time for all the films. The 3Si sample had the thickest oxide film. All the films consisted mainly of oxygen and iron with minor amounts of carbon. The low energy iron peak (47 eV) splits into two peaks at 44 and 52 eV at the surface of the oxide; the height and location of the two peaks change with sputtering time (32). The silicon peak also changes from 82 to 92 eV.

At the air/oxygen interface the films appear oxygen rich. Immediately below the surface there appears a shallow increase in the silicon content, which then decays to the level in the alloy. Similar gradual changes in air formed films on iron-chromium alloys have been observed (33).

The Auger composition profile of air oxidized 99.97% silicon is shown in Figure 27. The silicon wafer was prepared by oxidation at 900°C for 56 hours. The profile shows the ratio of the pH of oxygen

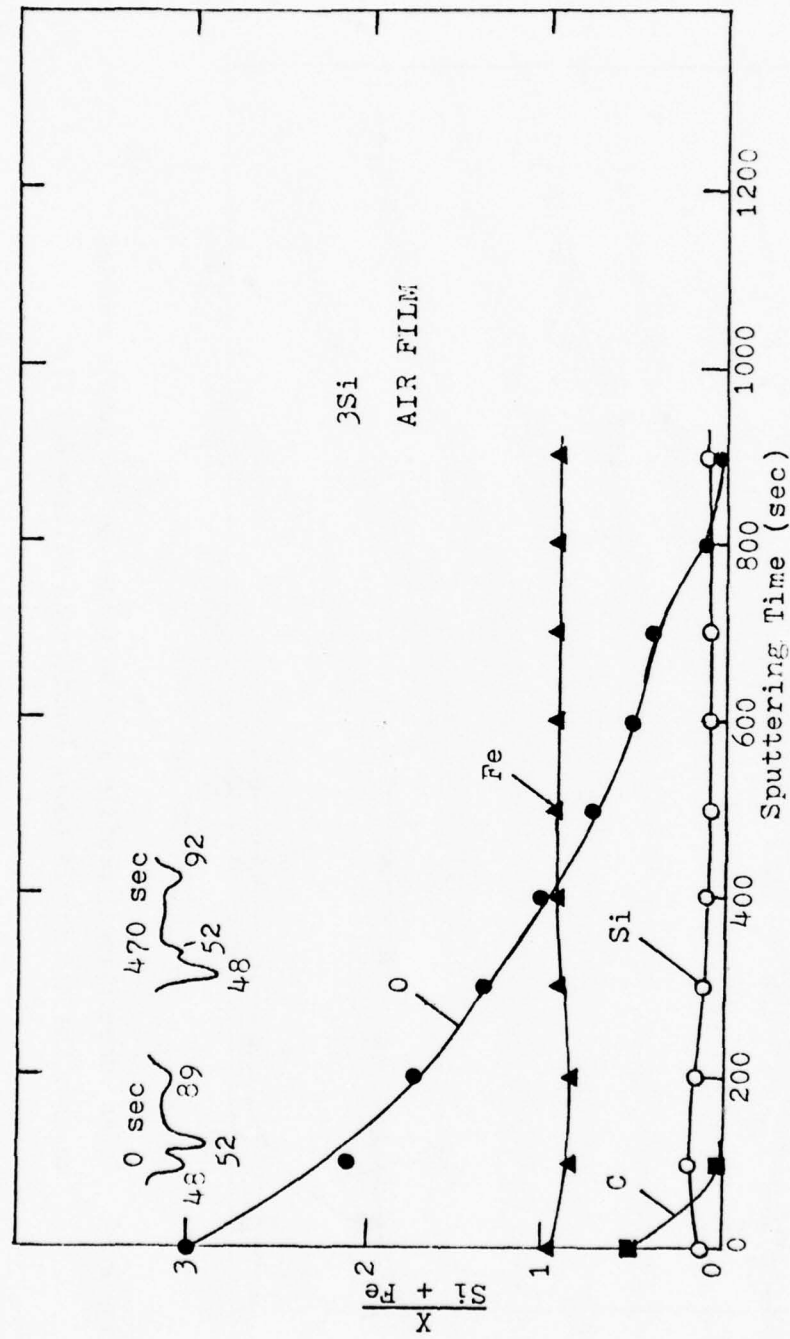


Figure 23. Auger compositional profile of film formed on 3Si sample exposed to only the air for 24 hours (sputtering voltage 600 V).



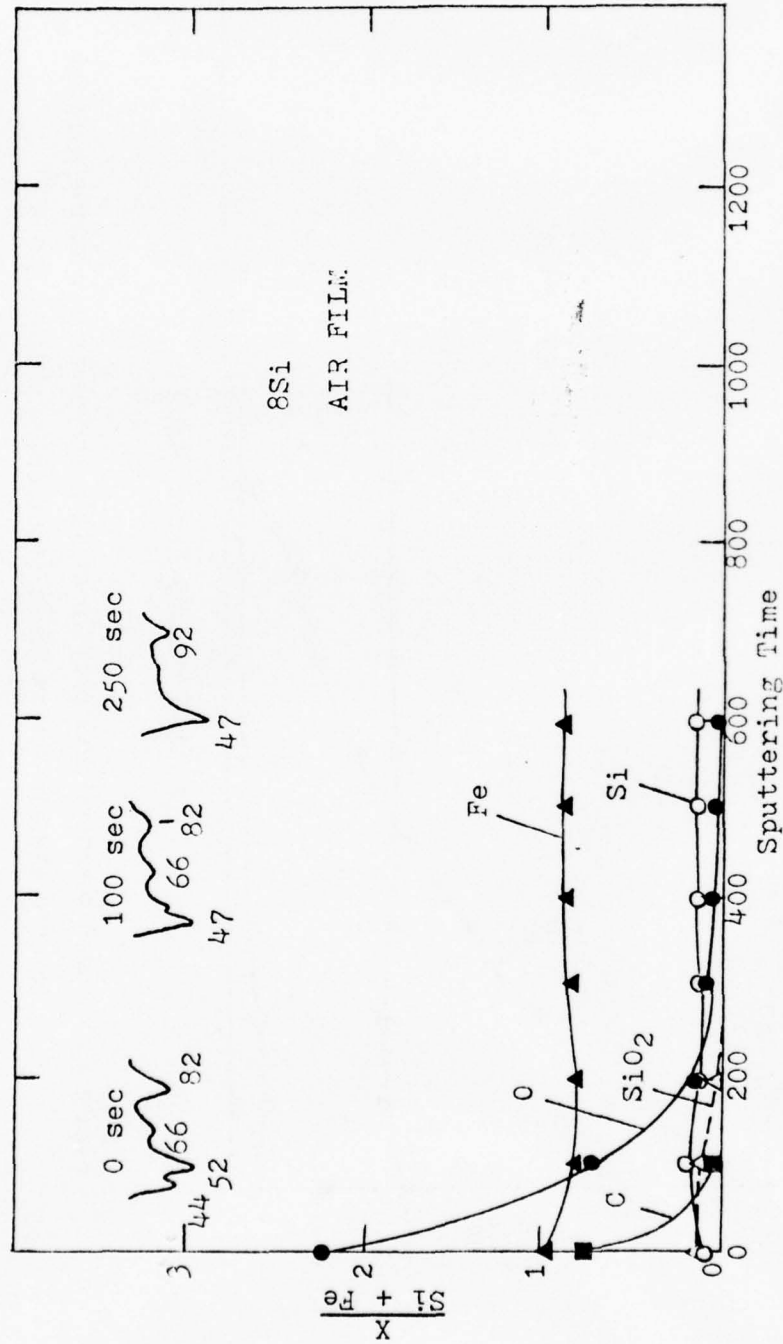


Figure 24. Auger compositional profile of film formed on 8Si sample exposed to only the air for 24 hours (sputtering voltage 600 V).

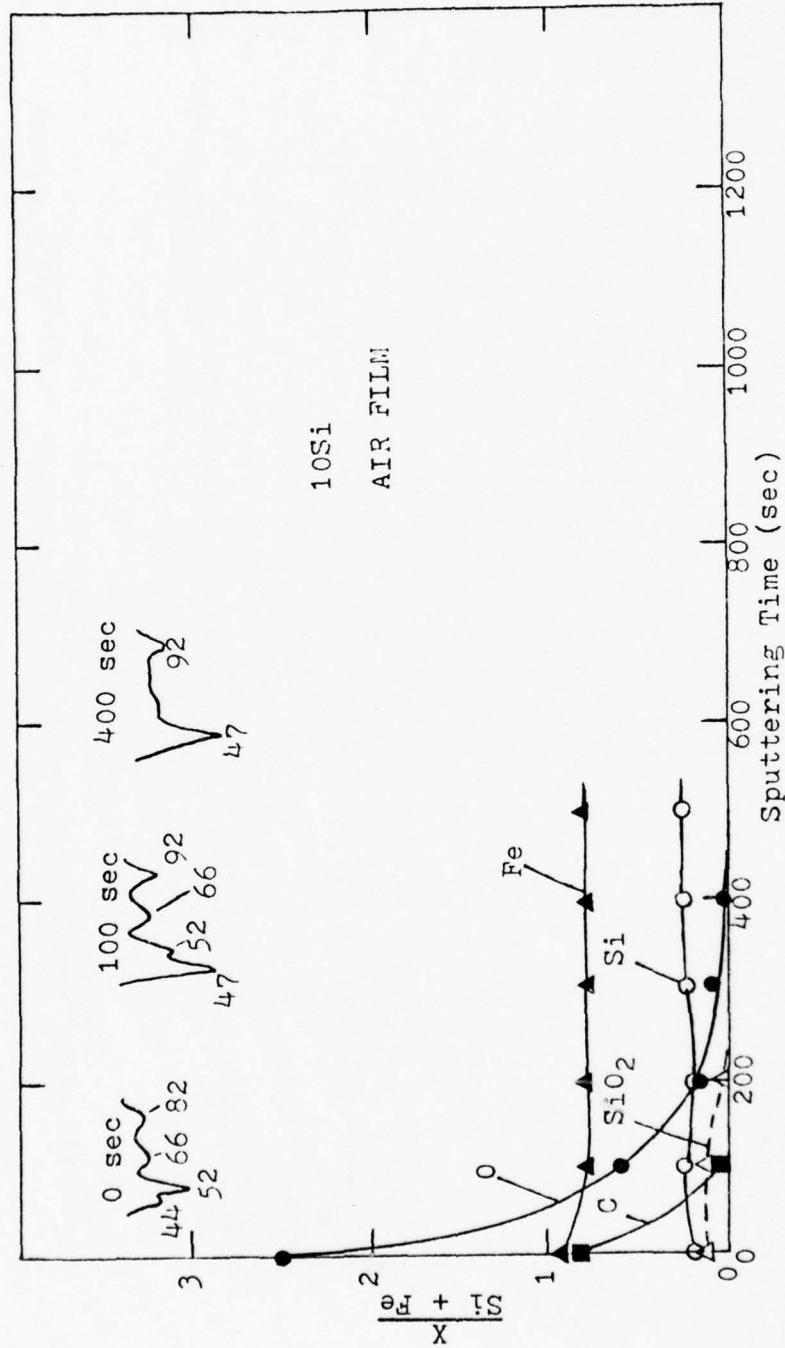


Figure 25. Auger compositional profile of film formed on 10Si sample exposed to only the air for 24 hours (sputtering voltage 600 V).

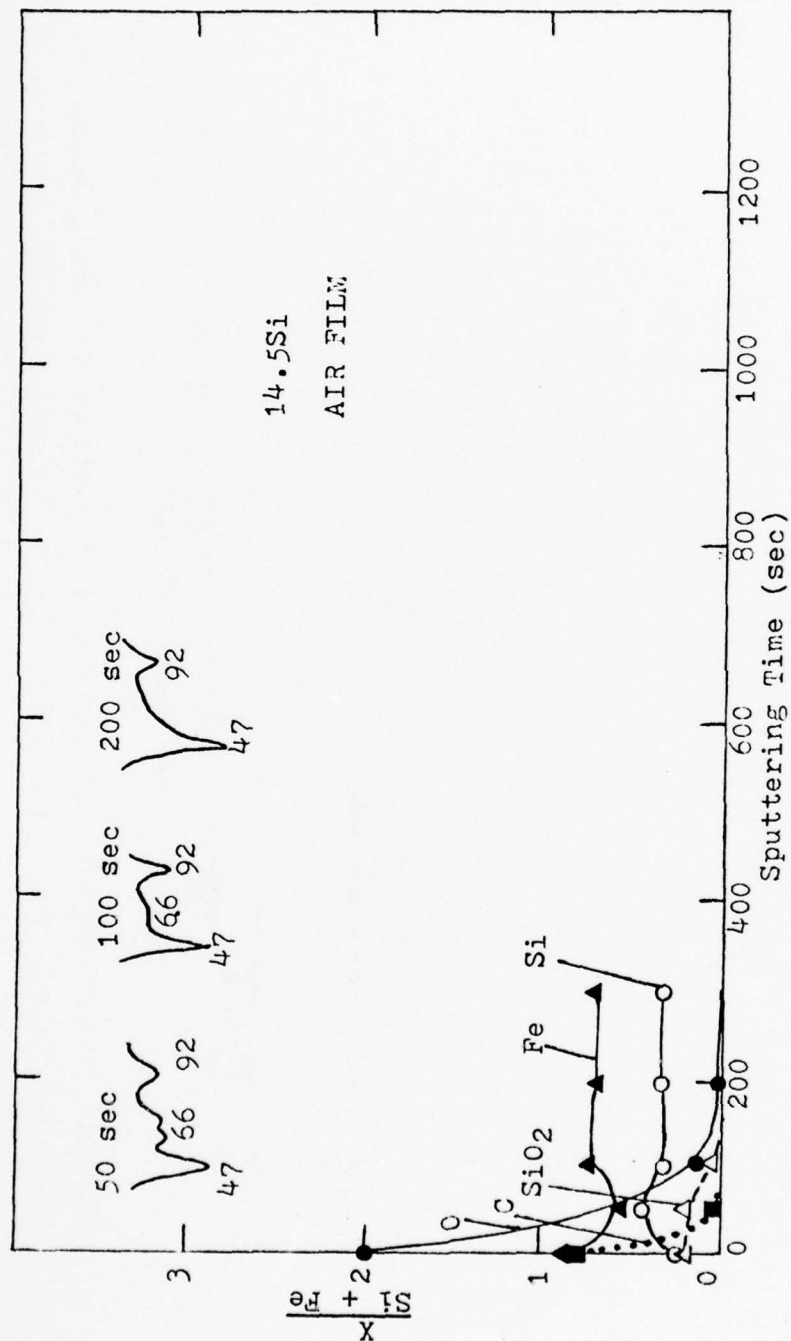


Figure 26. Auger compositional profile of film formed on 14.5Si sample exposed to only the air for 24 hours (sputtering voltage 600 V).

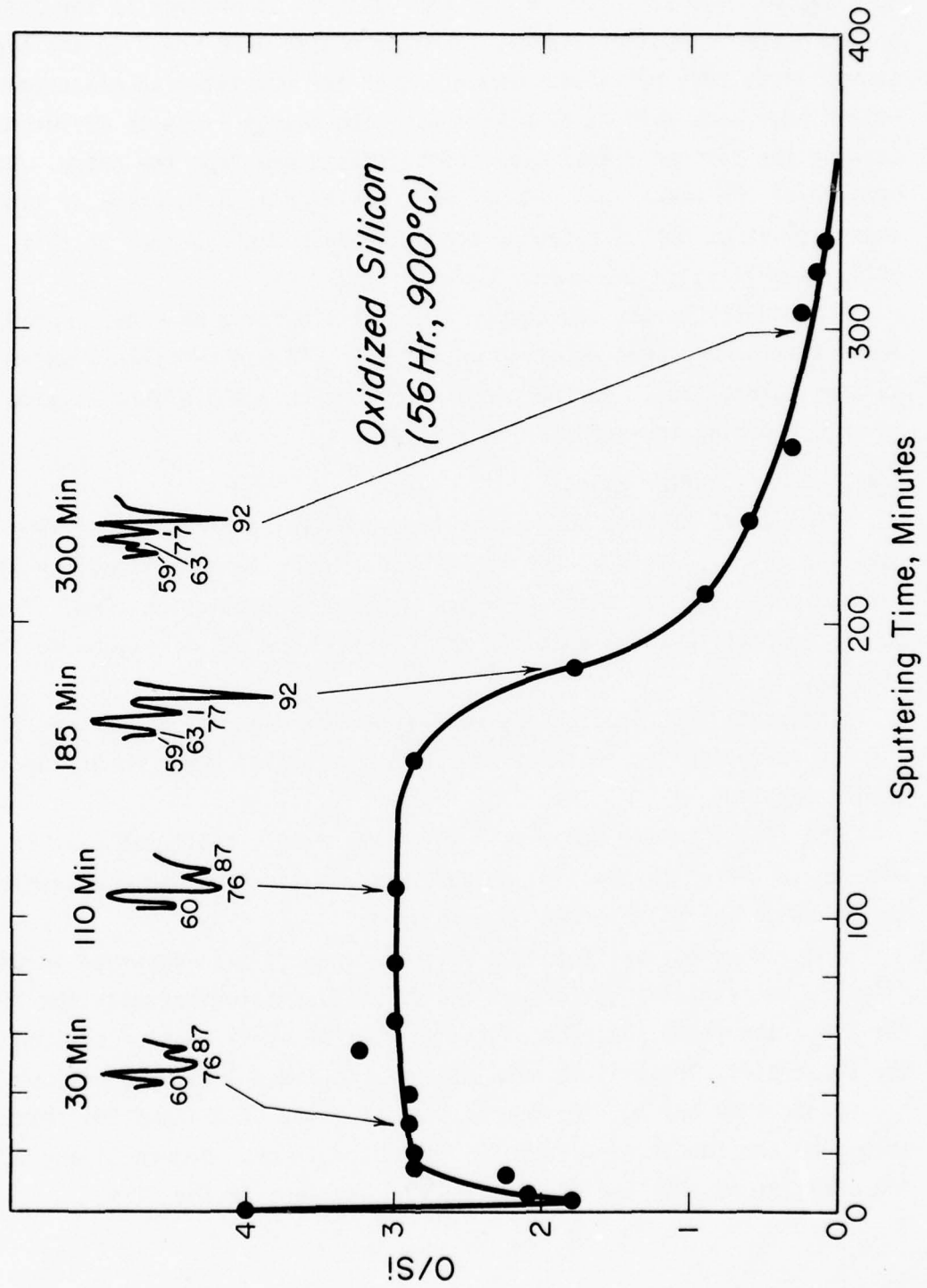


Figure 27. Auger compositional profile of silica formed in air on a silicon wafer.

to silicon. The shift in the low energy lines is evident in the inserts as the oxide is sputtered away. Similar shifts were noted in the high energy lines (34) but these were not used for quantitative measurements. Others have been able to resolve these high energy lines to differentiate between the silicon signal from the substrate and from the oxide. No measure of the variation in Auger peak position as a function of time or charging was attempted although the phenomenon was observed in this oxide as well as in the anodic oxide films.

The shifts in the low energy lines of  $\text{SiO}_2$  have been documented. These shifts have been observed on both  $\text{SiO}_2$  formed on silicon wafers as well as quartz (35). Further mention of the charging effect is made when it occurs during the anodic film analysis.

#### 4.4.3 Borate Buffer Films

Figures 28-32 show the composition profile of films formed in a borate buffer solution at 200 mV SCE for 1 hr. The normalized pph of the various constituents of the film are plotted vs sputtering time. The pure iron profile (Figure 28) is the ratio of the pph of oxygen to that of iron.

The profile of iron agrees well with that reported by Seo et al (36). The low energy shifts in the iron spectra were also observed as the sputtering time increased.

The 14.5Si sample had a film which was easily sputtered away in 100 sec, while the thickest film was observed on 3Si which was comparable in thickness to the film formed on pure iron.

The low energy shift in the silicon lines is also observed in these films. The initial positions of the 82 eV peak coincides with the lines for  $\text{SiO}_2$ ; the final position of the peak at 92 eV is that of silicon in the substrate. These lines were observed in the 8-14.5 wt % silicon samples.

Figures 29 and 30, the composition profiles of 3Si and 8Si respectively, show some enrichment of silicon in the oxide layer. Figure 31 and 32 show the profiles of 10Si and 14.5Si with  $\text{SiO}_2$  evident in the film.



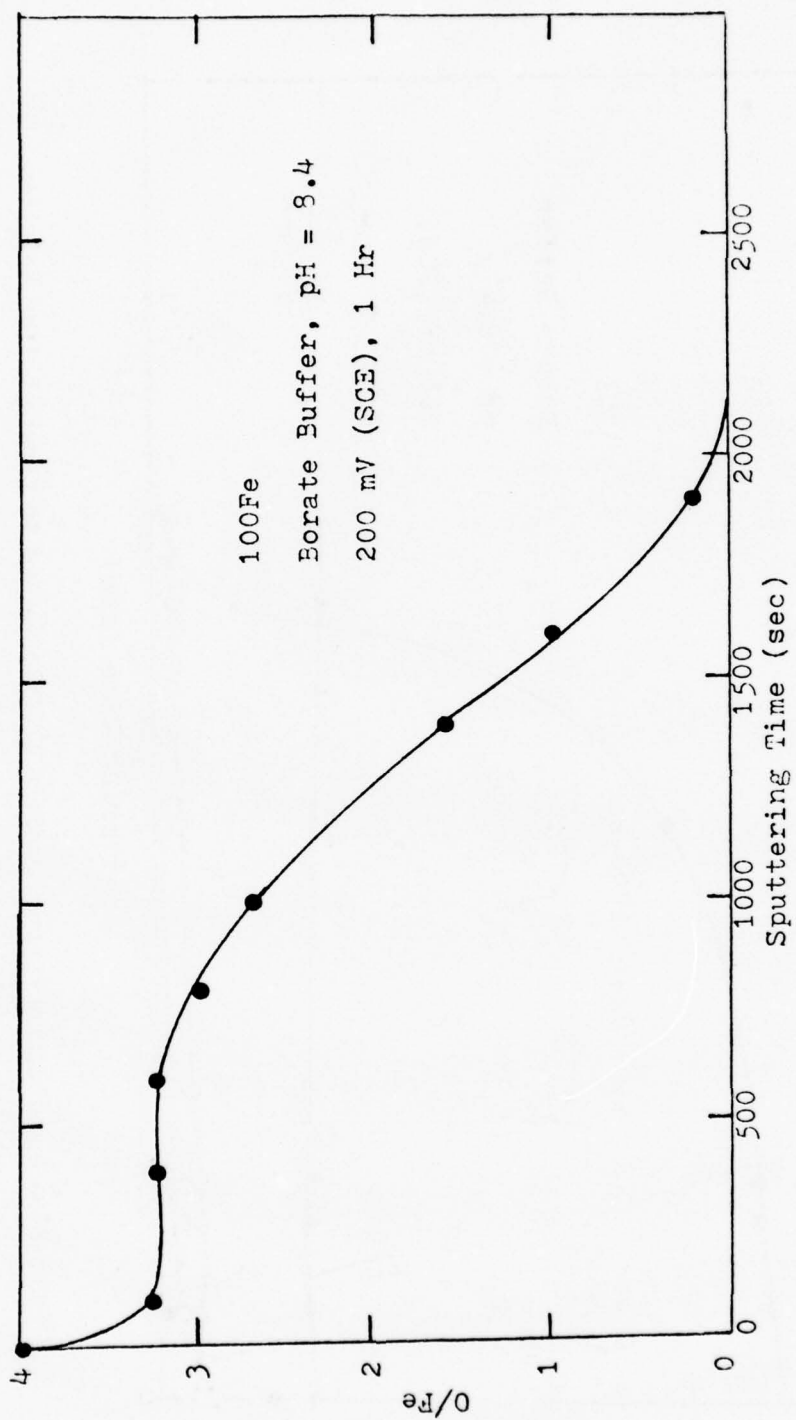


Figure 28. Auger compositional profile of 100Fe passivated for 1 hr in borate buffer at 200 mV (SCE) with sputtering voltage 600 V.

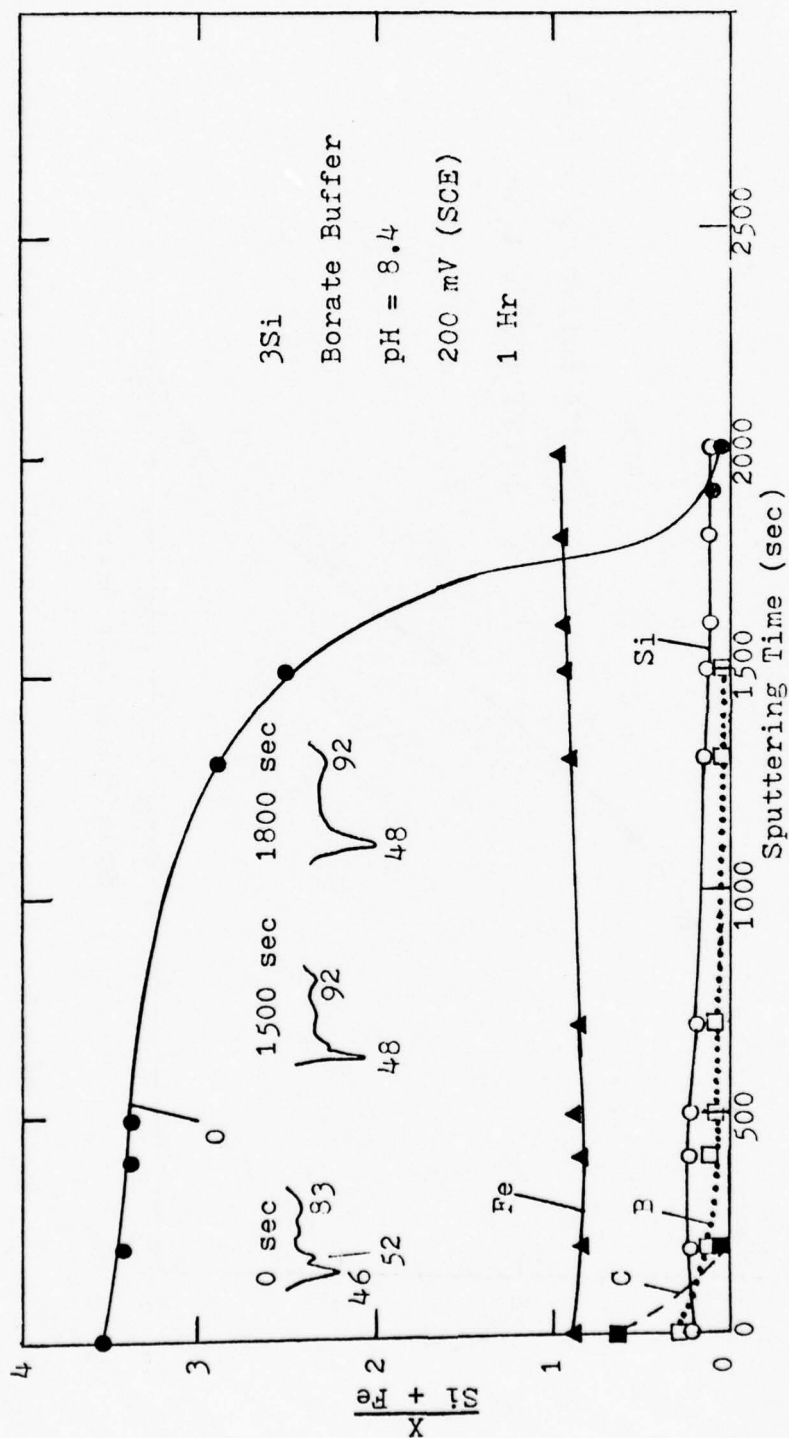


Figure 29. Auger compositional profile of film formed in borate buffer solution at 200 mV (SCE) for 1 hr (sputtering voltage of 600 V).

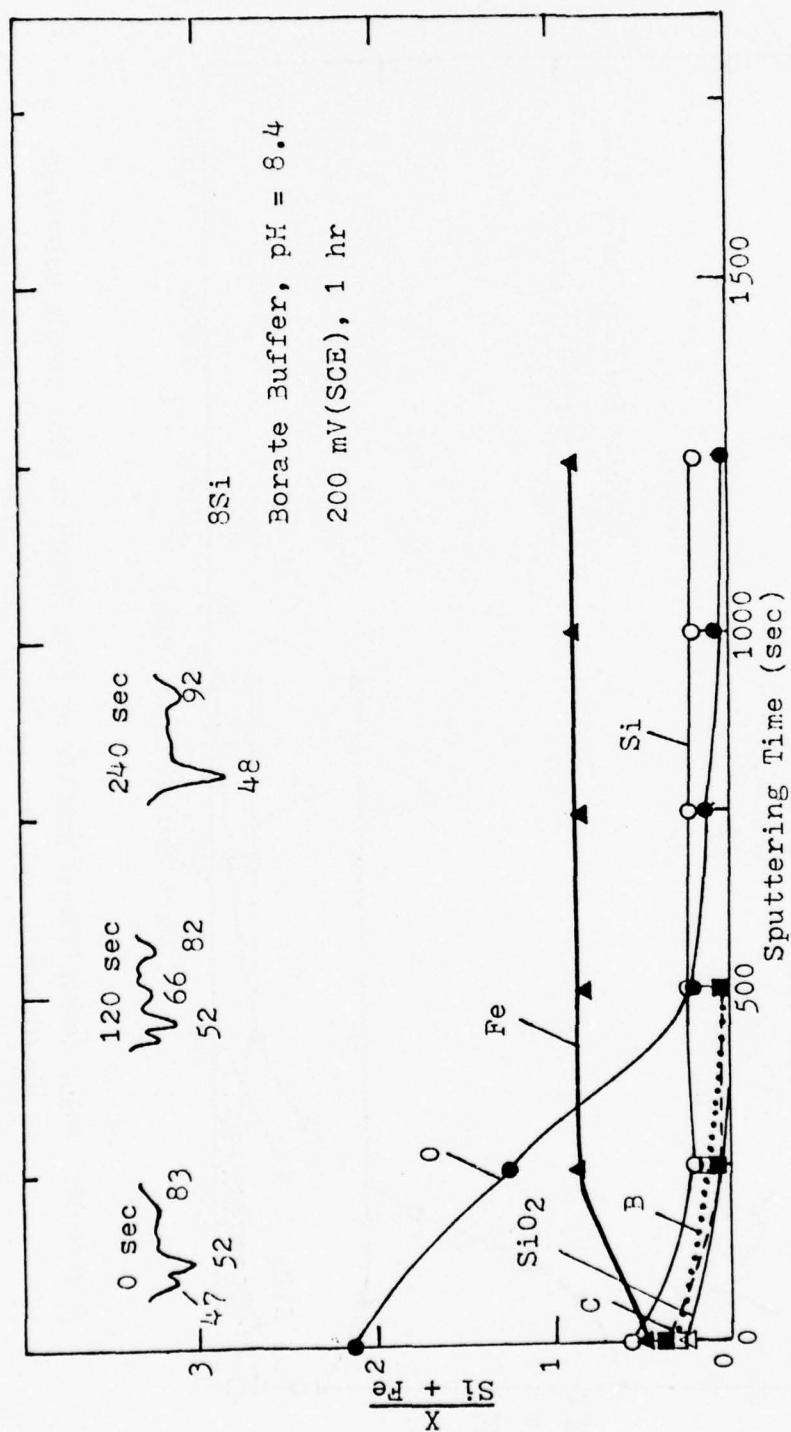


Figure 30. Auger compositional profile of film formed on 8 Si sample polarized in borate buffer solution at 200 mV (SCE) for 1 hr (sputtering voltage 600 V).

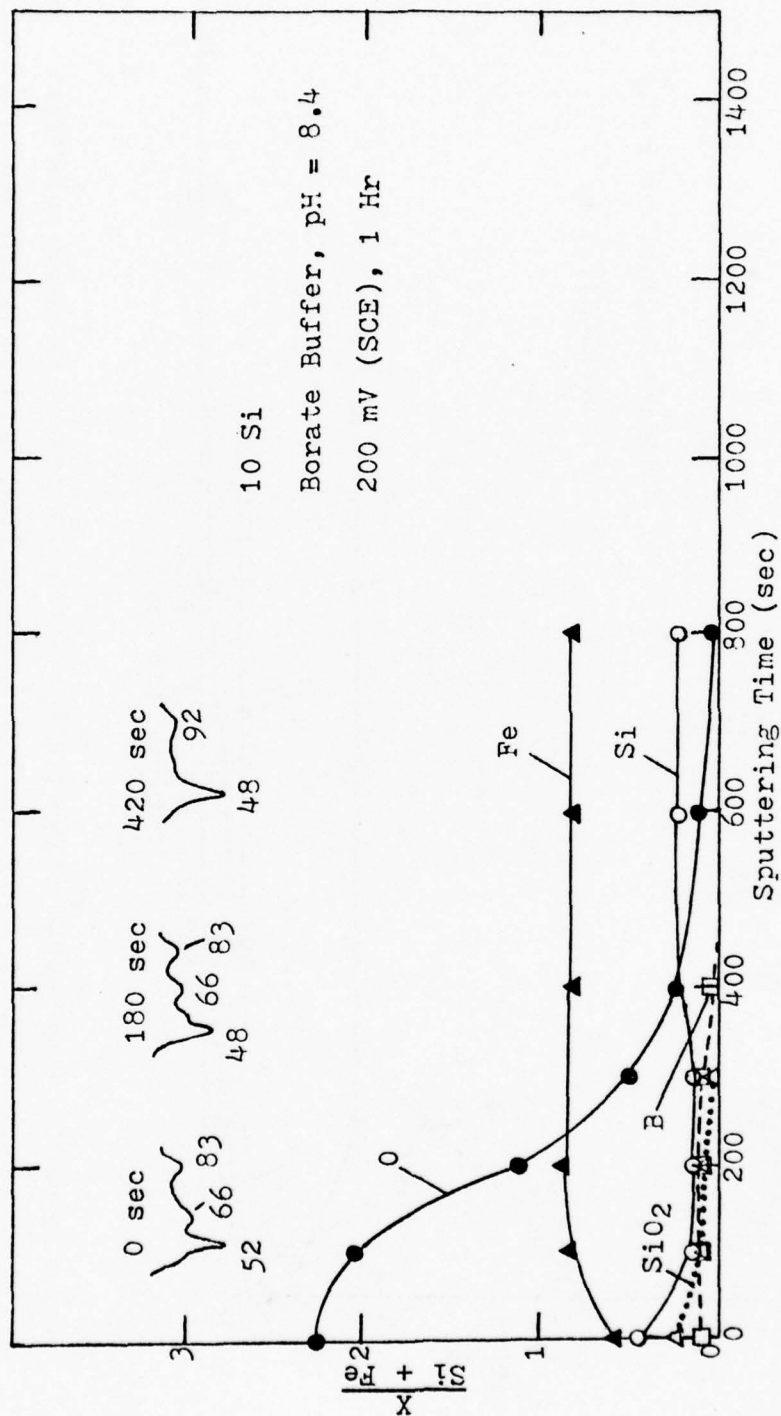


Figure 31. Auger compositional profile of film formed on 10Si sample polarized in borate buffer solution at 200 mV (SCE) for 1 hr (sputtering voltage 600 V).

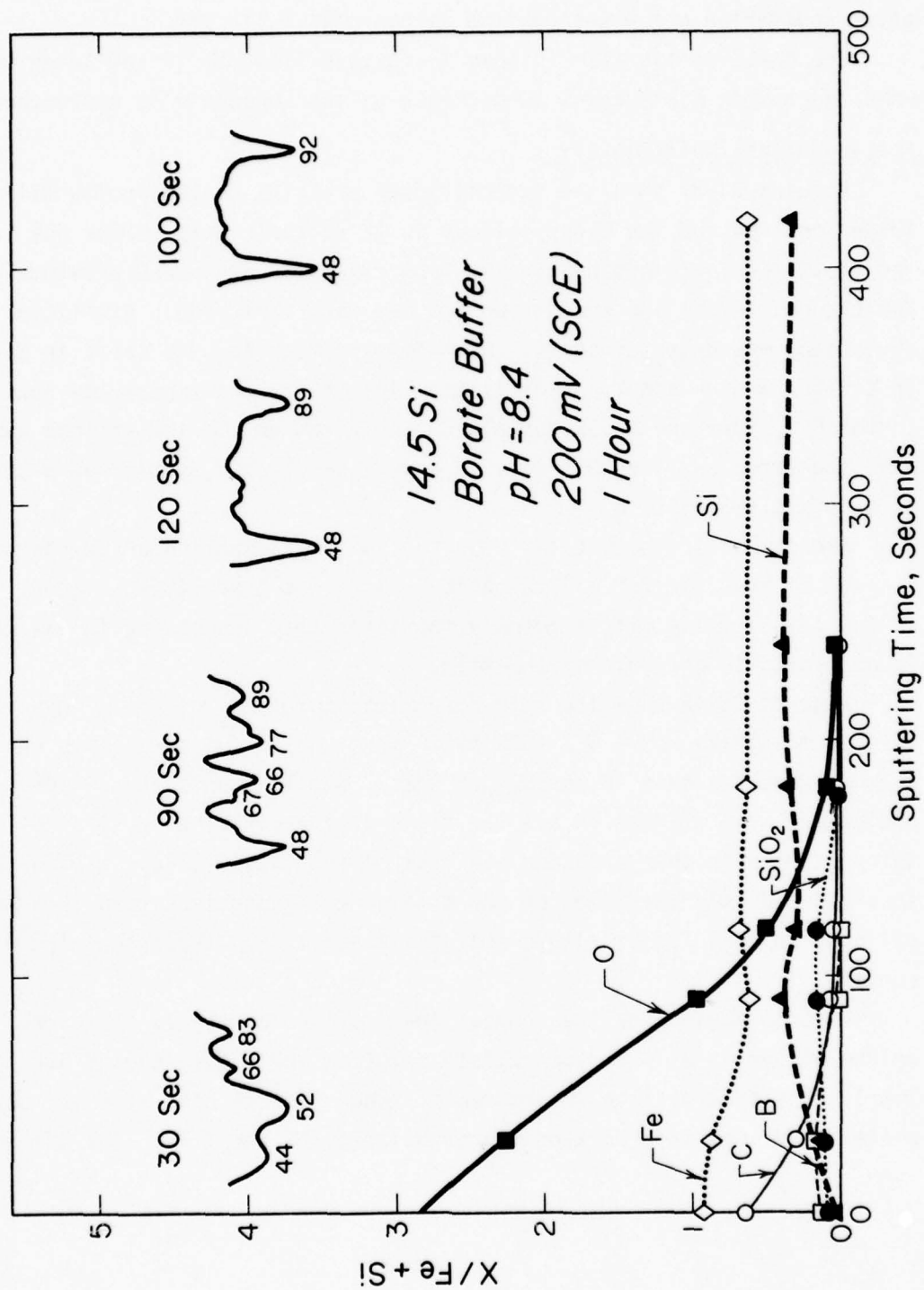


Figure 32. Auger compositional profile for 14.5Si in borate buffer solution.



The carbon in the film results from the preparation procedure since after sputtering a few seconds the carbon peak falls off.

The boron in the film follows the oxygen line; it is sputtered away when the oxygen peak begins to decrease as the substrate is approached.

#### 4.4.4 Sulfate Solution Films

Figures 33-37 show the compositional profiles of the anodic films formed on iron and the binary alloys in 1N sulfuric acid (800mV SCE for 1 hr). The plots were obtained by the same pph ratios as mentioned previously. The changes in the low energy spectra are also indicated. A silicon enrichment was detected in all the films accompanied by a shift in  $\text{SiO}_2$  to silicon in the binary alloy films. The shifts are especially noticeable in the 8Si, 10Si and 14.5Si samples. The films on the low silicon samples were sputtered away in 2000 sec. However, the 14.5Si sample had a plateau of constant composition.

The carbon in these films results from contamination while the sulfur is part of the film for all the alloys with less than 14.5% silicon. In the 14.5Si alloy, it is quickly sputtered away indicating it was not incorporated in the bulk of the film.

Figures 38-42 show the film composition profiles of the alloys in 1N sodium sulfate, pH = 3.2 (600 mVSCE for 1 hr). All the alloys showed a continuous decrease in the oxygen peak. Small amounts of silicon enrichment were evident in all the films of the binary alloys. The thinnest film in this solution was that of the 14.5Si alloy. Sulfur was incorporated into the films of the alloys containing less than 14.5 wt % silicon; in this latter alloy, sulfur was easily sputtered from the alloy surface.

Figures 43-47 show the composition profiles of the films formed on the alloys in a 1N sodium sulfate solution (pH = 6.4, 600 mV SCE for 1 hr). The film on iron showed two plateaus for the pph ratios of oxygen while sulfur was incorporated in the majority of the film. The 3Si and

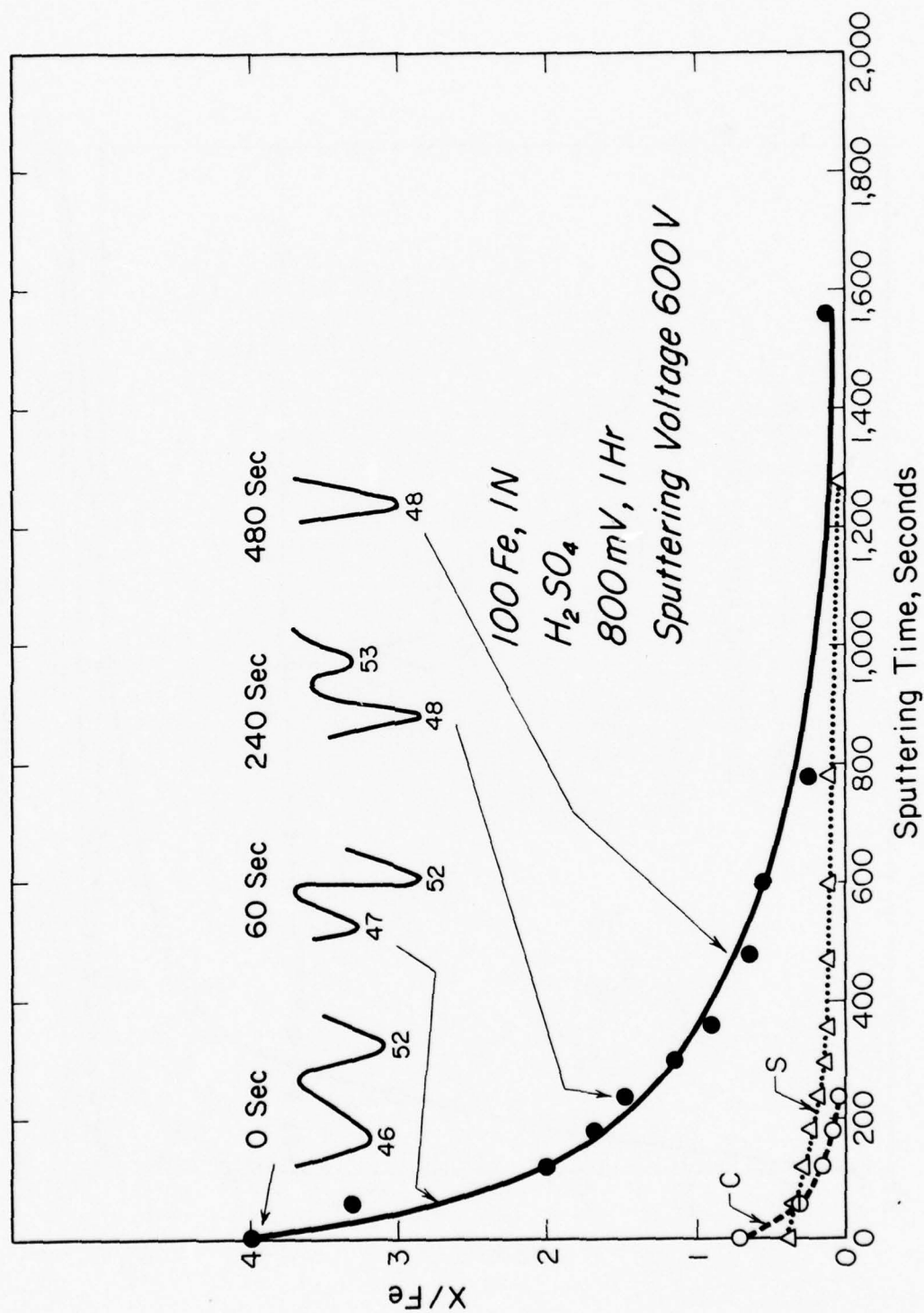


Figure 33. Auger compositional profile for iron with film formed in 1N sulfuric acid.

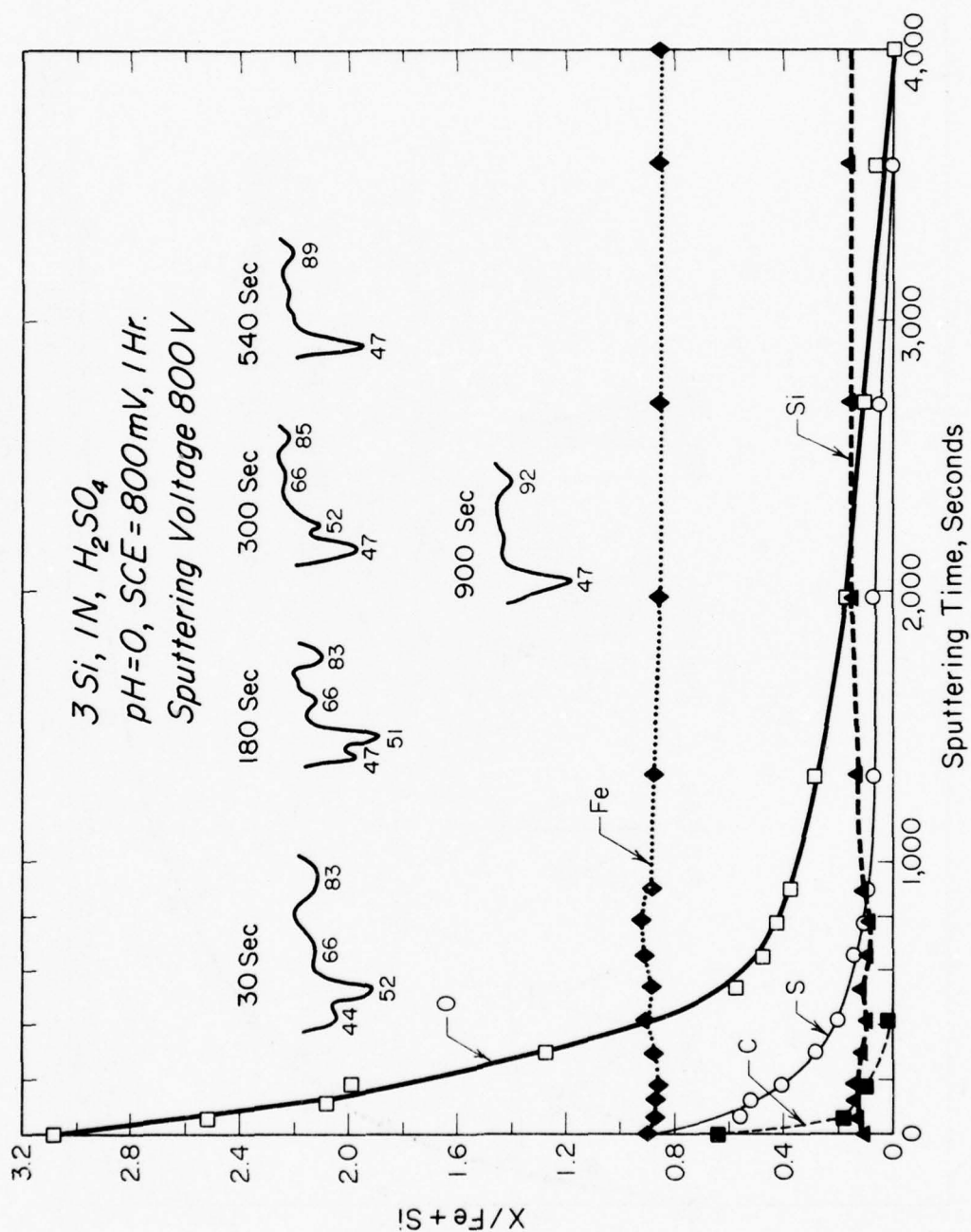


Figure 34. Auger compositional profile of film formed on 3Si in 1N sulfuric acid.

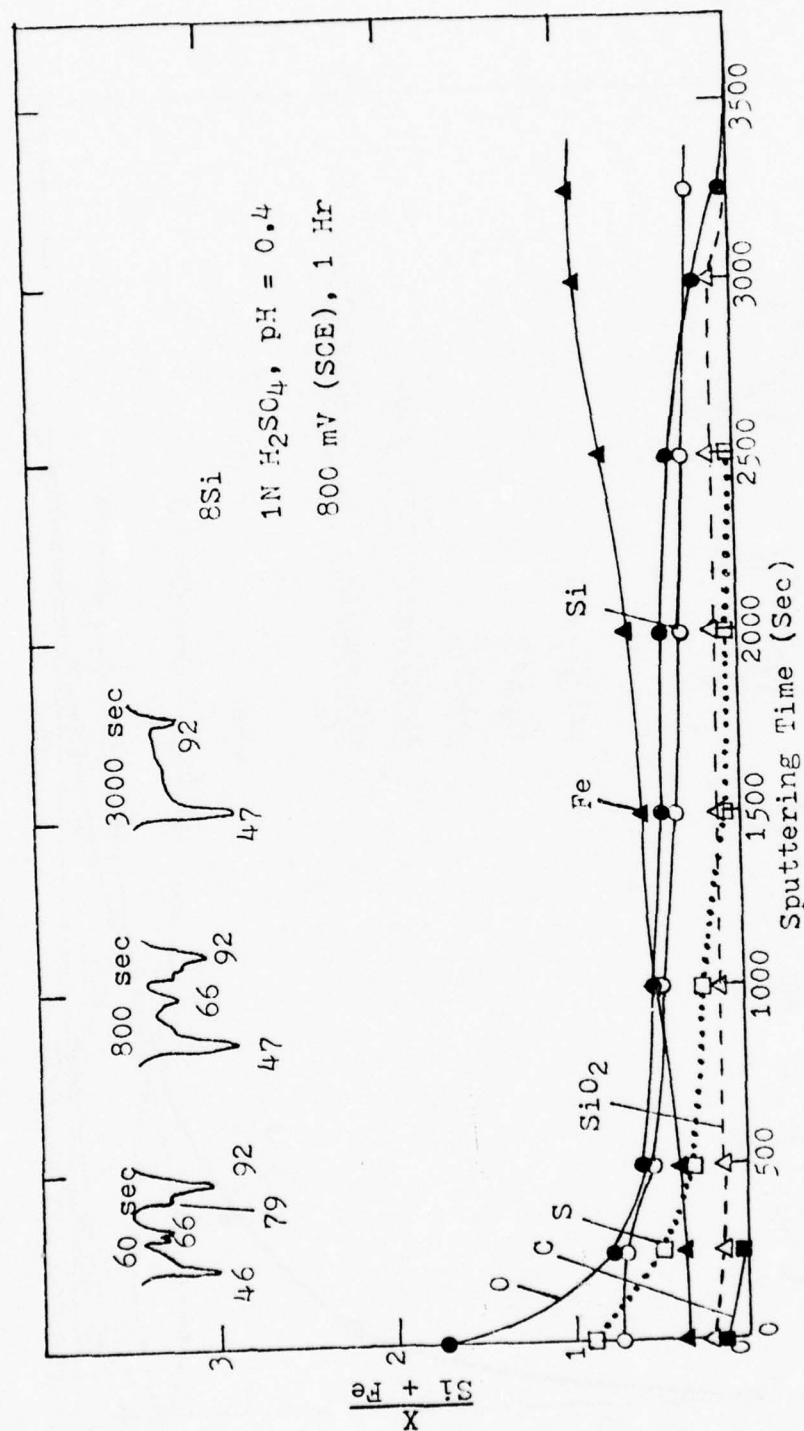


Figure 35. Auger compositional profile of film formed on 8Si sample polarized at 800 mV (SCE) for 1 hr (sputtering voltage 600 V).

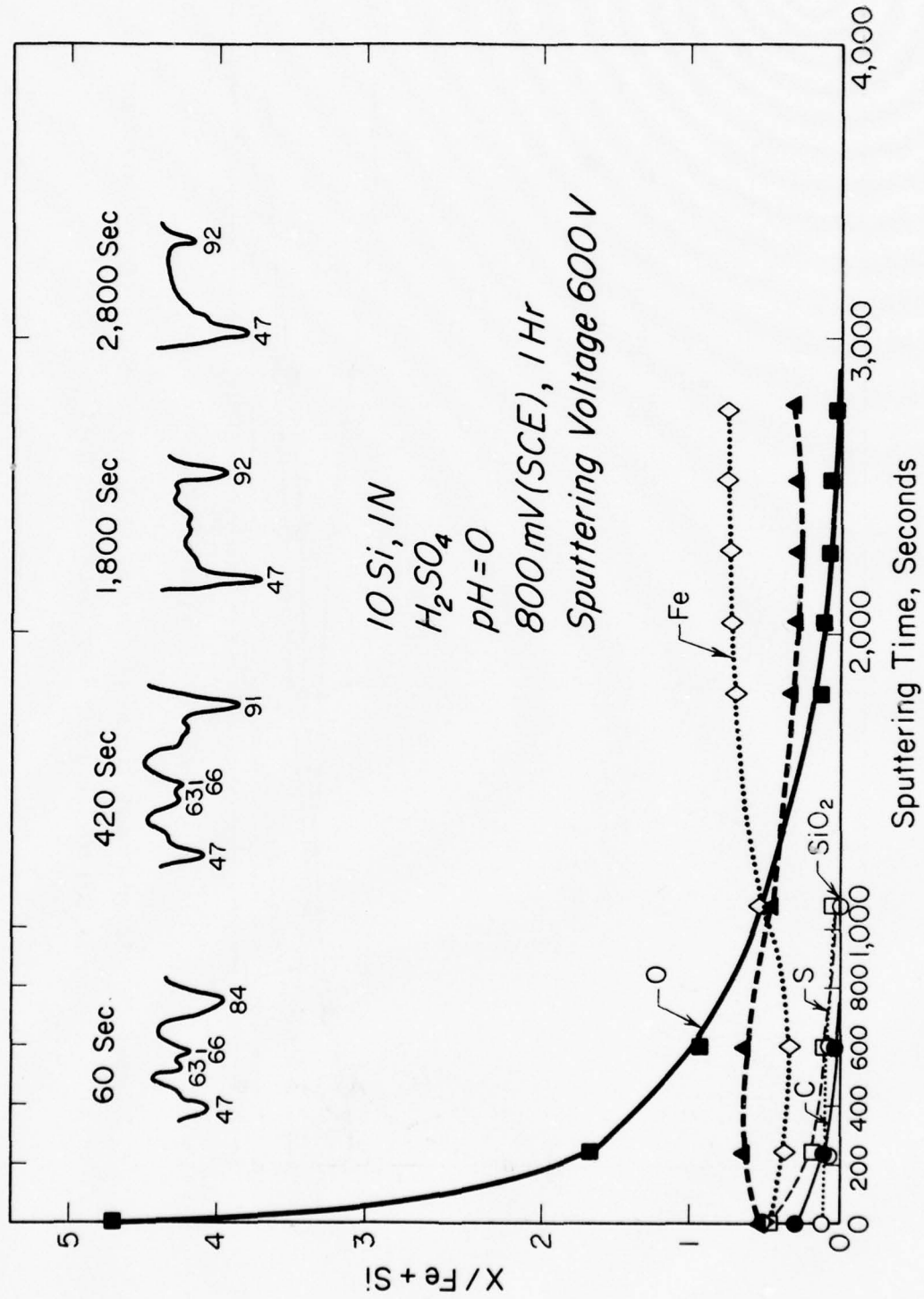


Figure 36. Auger compositional profile of film formed on 10Si in 1N sulfuric acid.



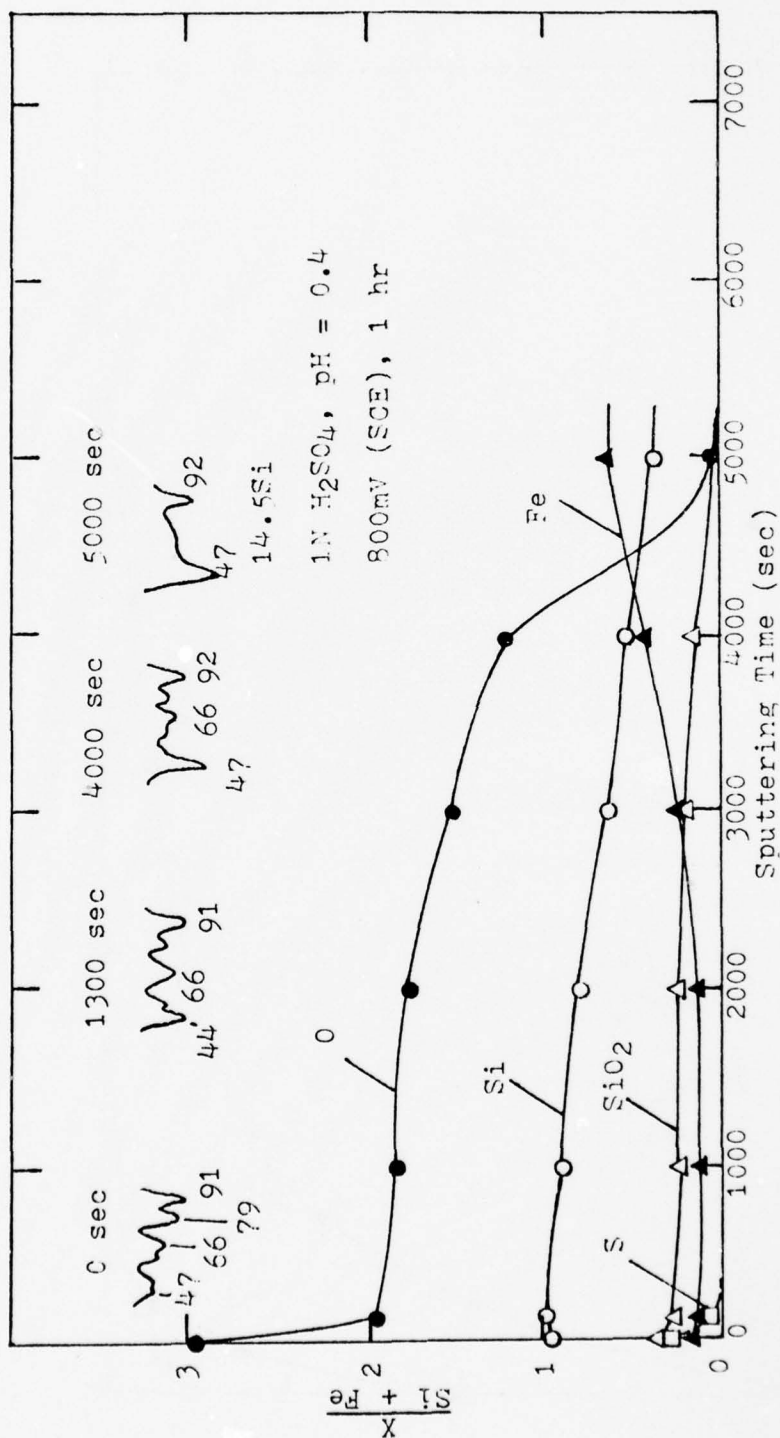


Figure 37. Auger compositional profile of film formed on 14.5Si sample polarized in 1N sulfuric acid at 800 mV (SCE) for 1 hr (sputtering voltage 600 V).

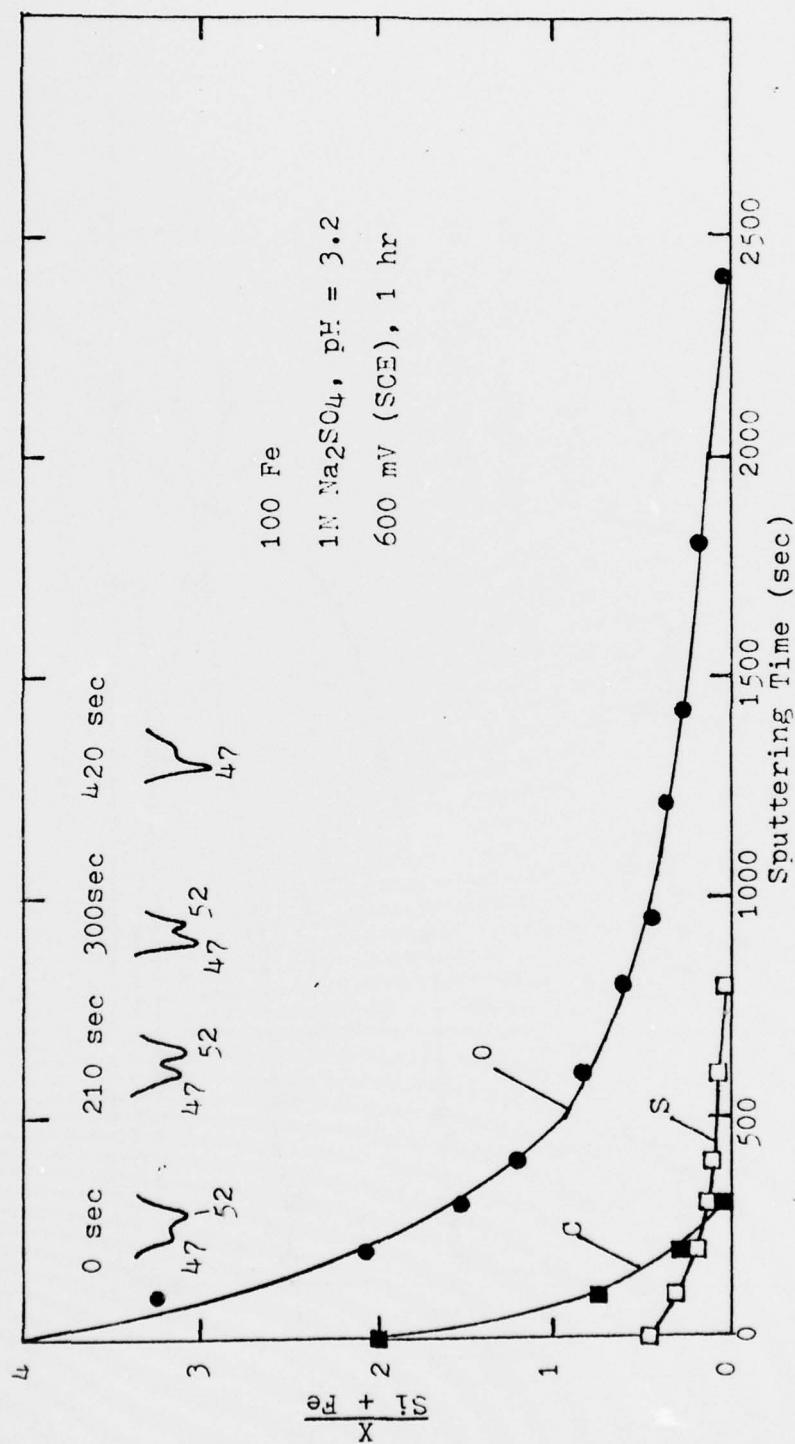


Figure 38. Auger compositional profile of film formed on 100Fe sample polarized in 1N sodium sulfate (pH = 3.2) at 600 mV (SCE) for 1 hr (sputtering voltage 600 V).

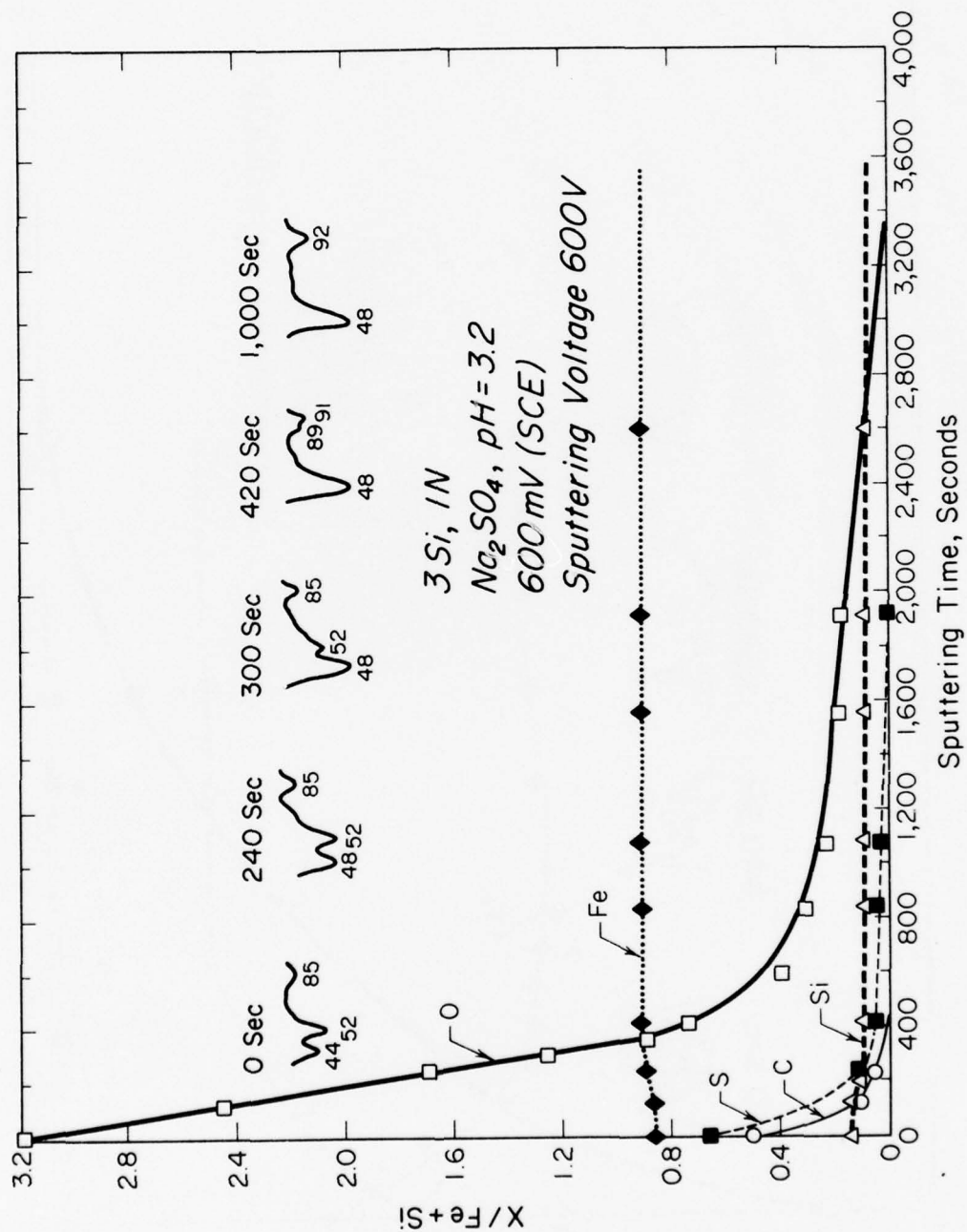


Figure 39. Auger compositional profile of film formed on 3Si in 1N sodium sulfate.

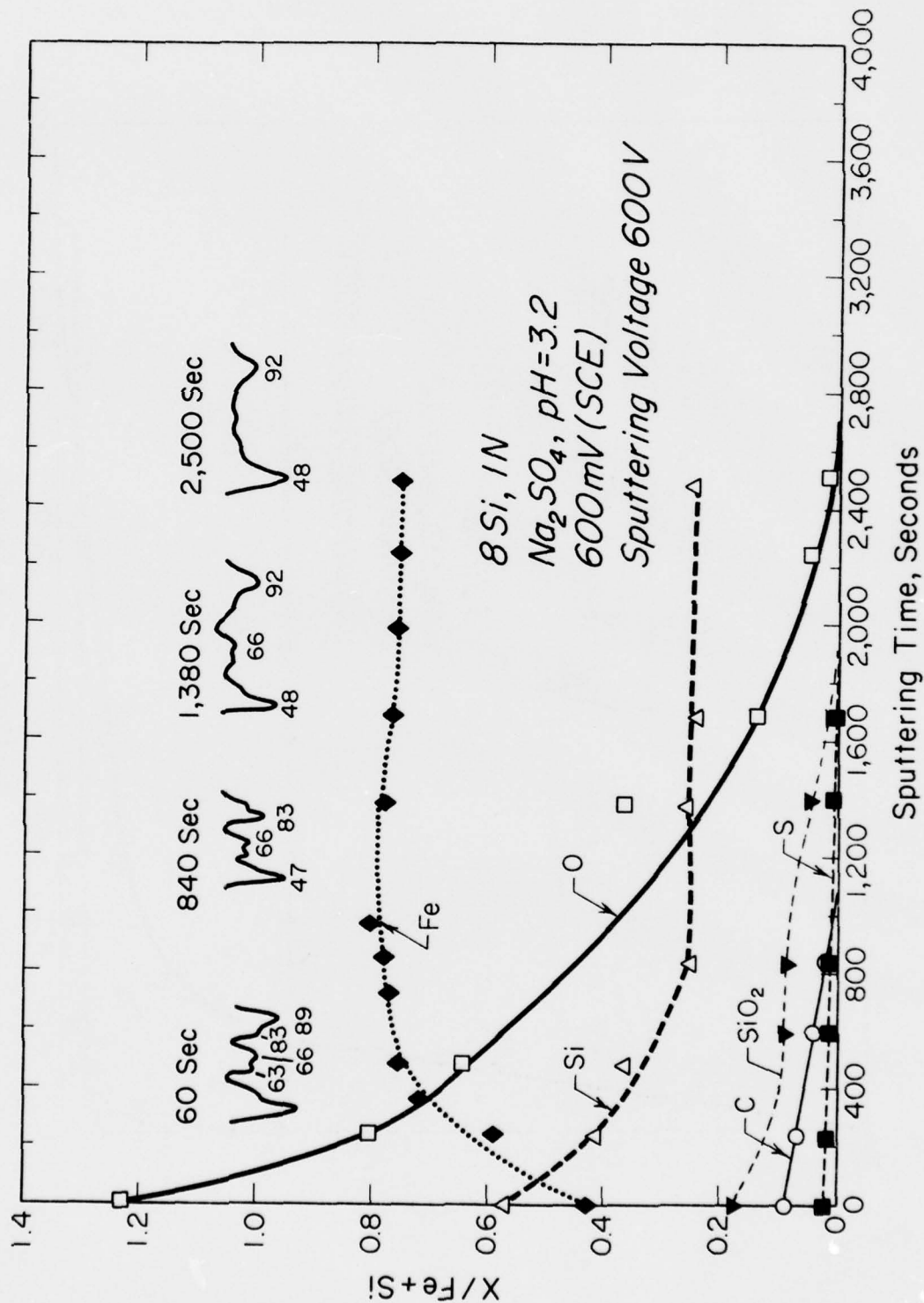


Figure 40. Auger compositional profile of film formed on 8Si in 1N sodium sulfate.

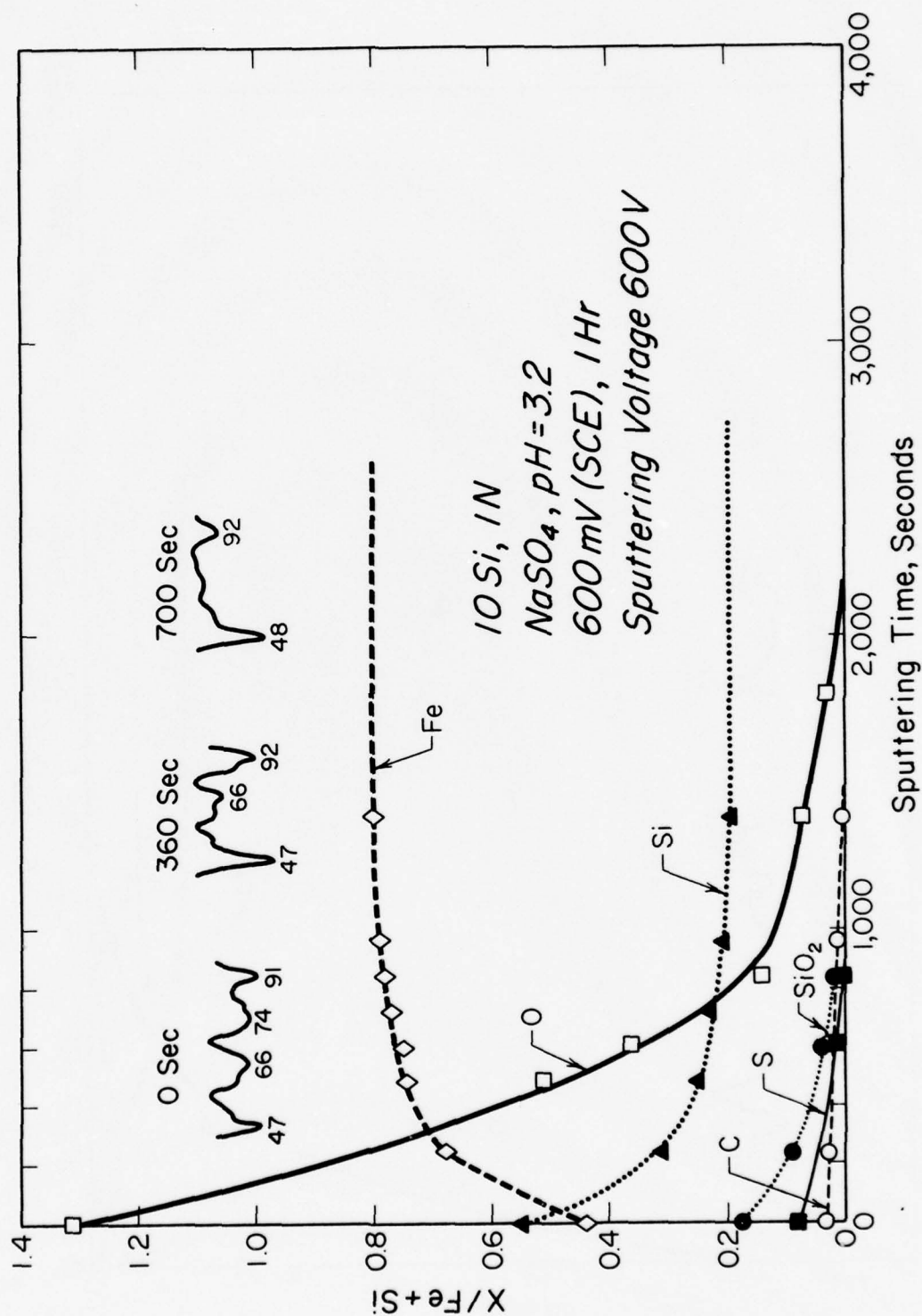


Figure 41. Auger compositional analysis of film formed on 10Si in 1N sodium sulfate, pH = 3.2.



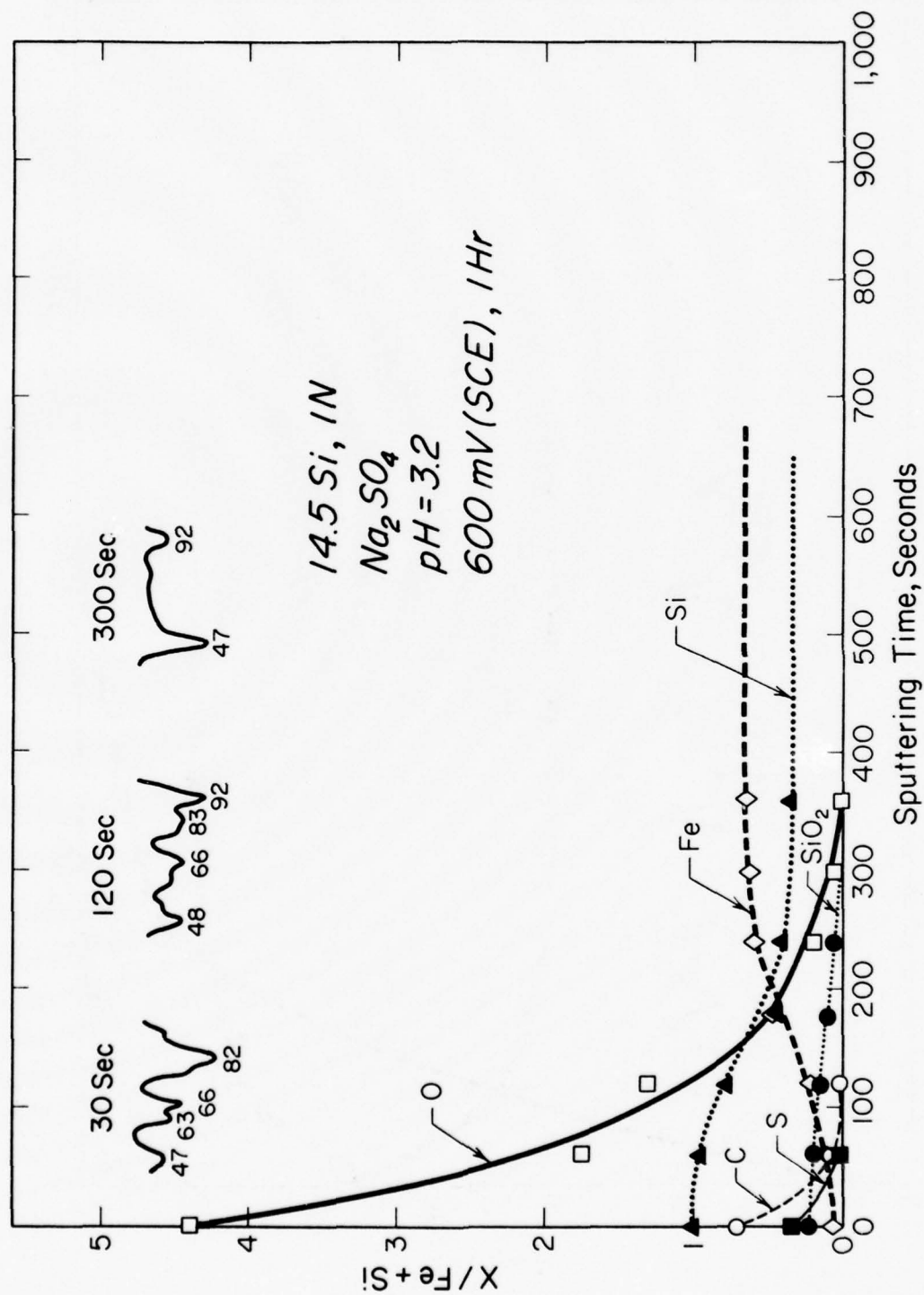


Figure 42. Auger compositional profile of 14.5Si with film formed in 1N sodium sulfate, pH = 3.2.

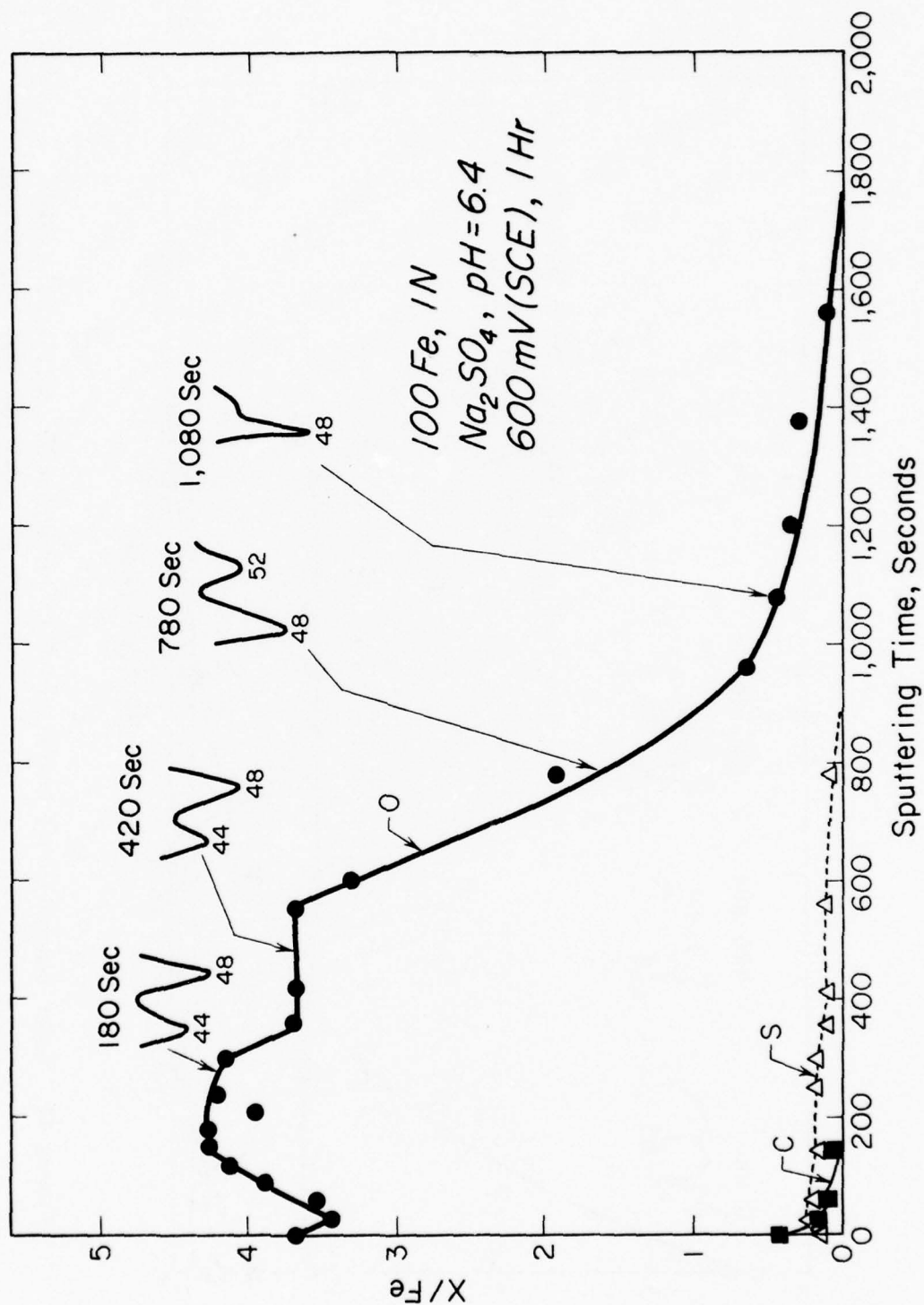


Figure 43. Auger compositional profile of film formed on iron in 1N sodium sulfate.

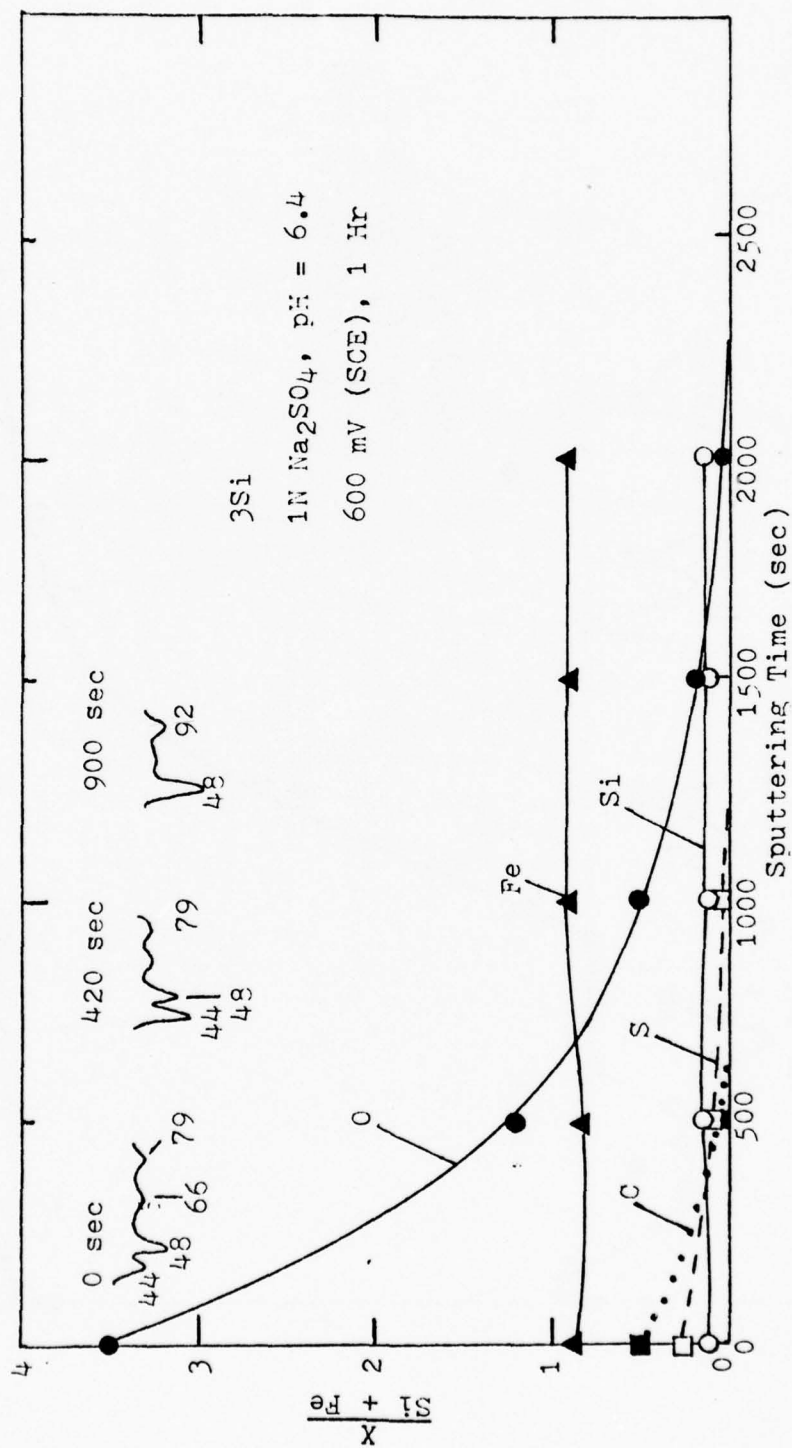


Figure 44. Auger compositional profile of film formed on 3Si sample polarized in 1N sodium sulfate (pH = 6.4) at 600 mV (SCE) for 1 hr (sputtering voltage 600 V).

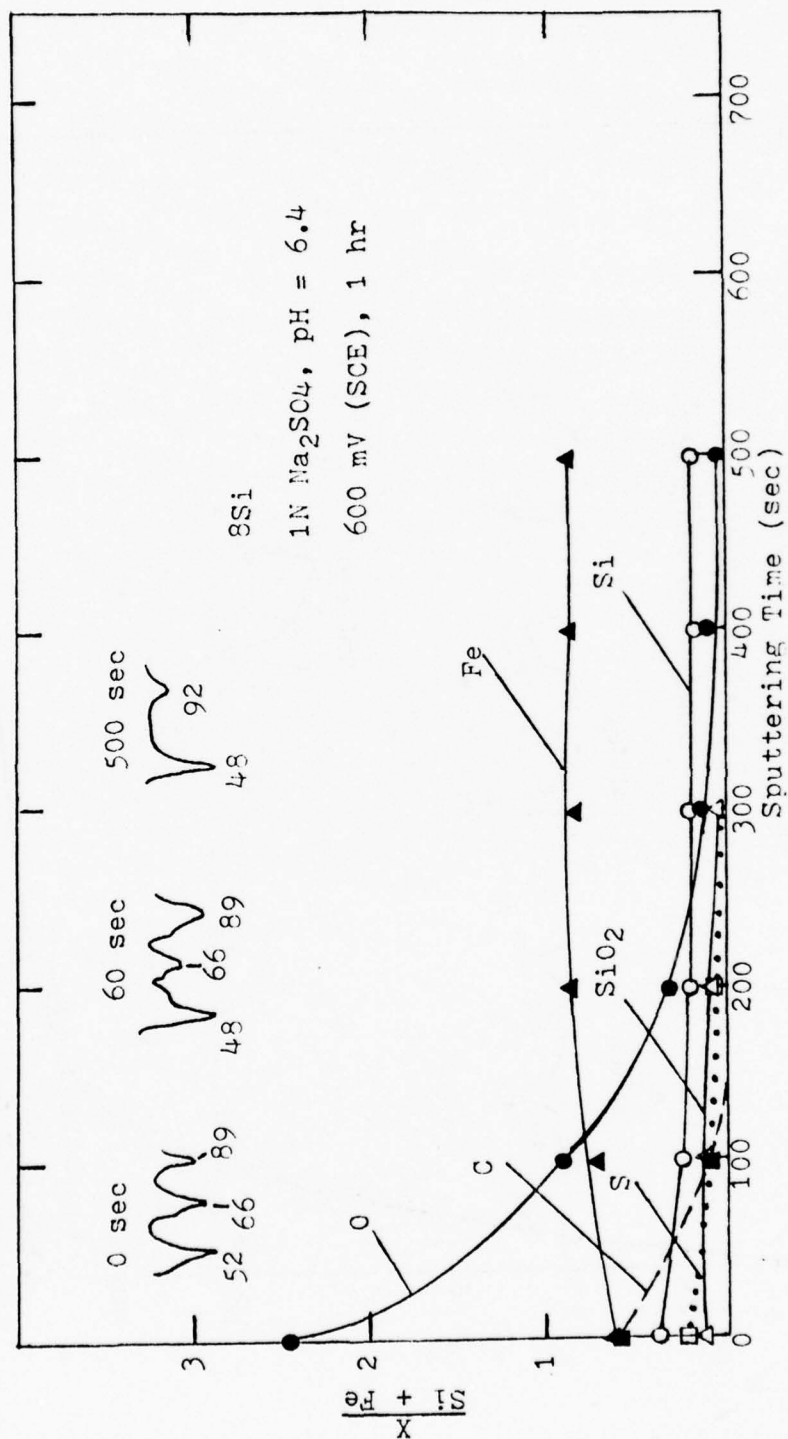


Figure 45. Auger compositional profile of film formed on 8Si sample polarized in 1N sodium sulfate (pH = 6.4) at 600 mV (SCE) for 1 hr (sputtering voltage 600 V).

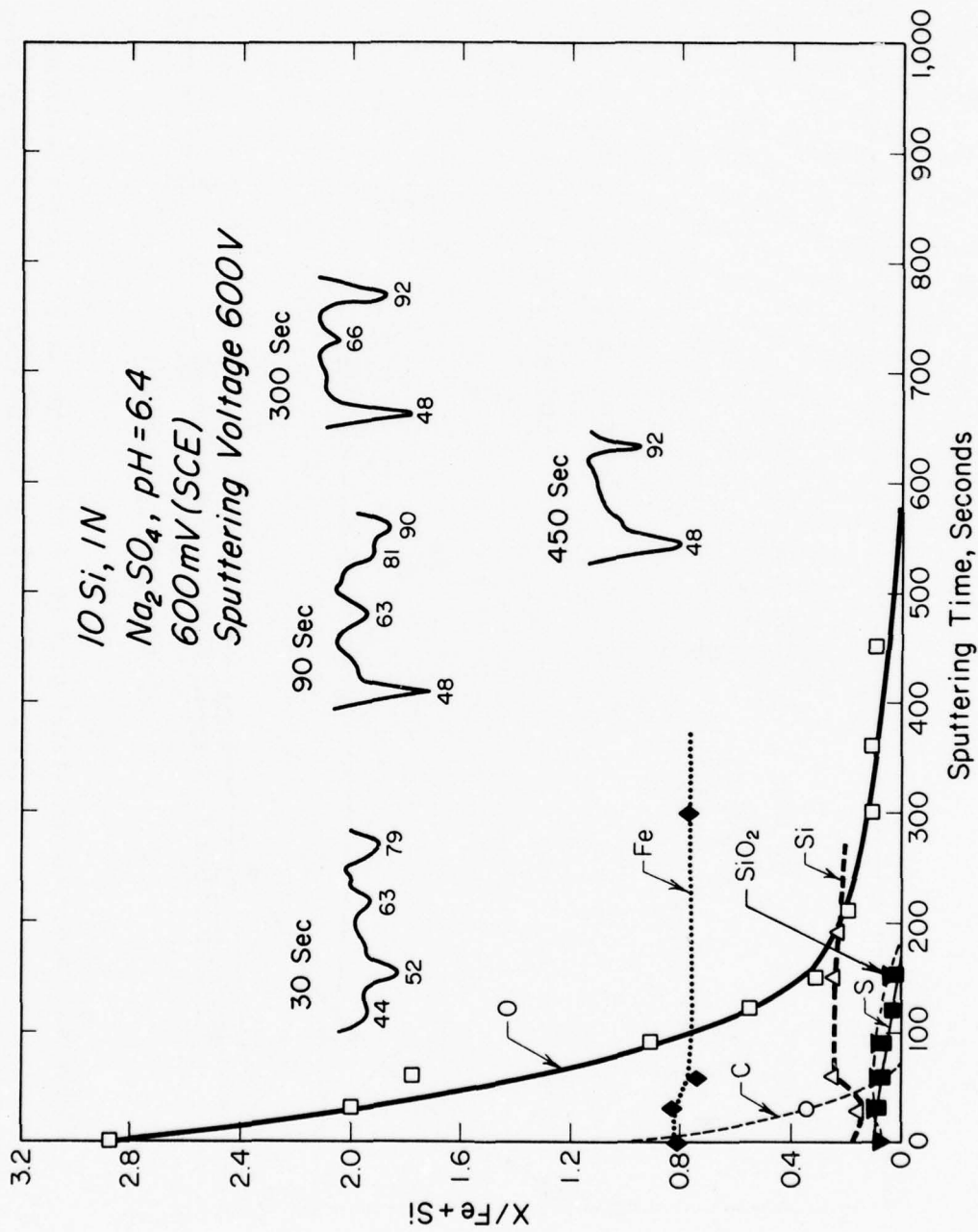


Figure 46. Auger compositional profile of film formed on 10Si in 1N sodium sulfate.



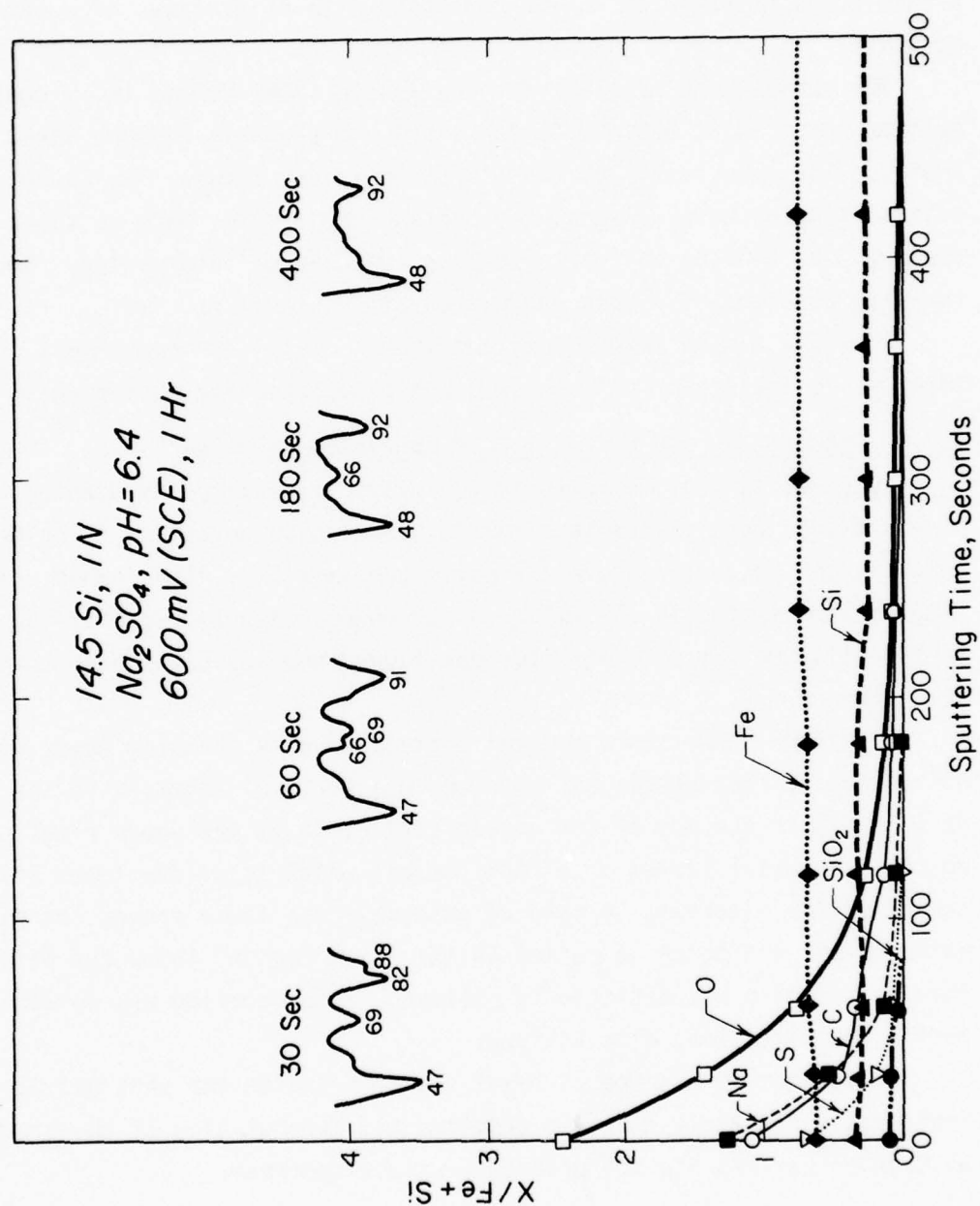


Figure 47. Auger compositional profile of film formed on 14.5Si in 1N sodium sulfate.

8Si alloys exhibited a slight amount of silicon enrichment in the film. The 10Si and 14.5Si alloys also showed enrichment. The binary alloys show a continuous decrease in the oxygen peaks with no plateaus of constant composition.

The composition profiles for the anodic films formed in 1N sodium sulfate (pH = 10.3, 600 mV SCE for 1 hr) are shown in Figures 48-50. Profiles for pure iron, 10Si and 14.5Si only are shown. The lower silicon samples were not analyzed because their films were so thick that charging was induced thereby obscuring composition information. Such charging problems have been found when  $\text{SiO}_2$  is analyzed.

The 10Si sample showed a slight amount of silicon enrichment in the film, while the higher silicon sample did not show any enrichment.

#### 4.4.5 Films in Borate Buffer + 0.1M Potassium Chloride

To characterize the role silicon plays in pitting resistance, the binary alloys were placed in a borate buffer plus potassium chloride solution and polarized above the pitting potential. Pits formed, then the samples were placed in the Auger vacuum chamber for analysis of the material in the pits and the material that had flowed and deposited next to the pits (Figure 51).

Figure 52 shows the elemental distribution by scanning Auger of the pitted areas. The sample was mounted in a vertical position in the solution; in this figure the top of the sample surface is at the upper right hand corner. Material flowed down from the pit which is at the lower left hand corner of the pictures. A halo of potassium was found around the pits, while oxygen and boron deposited in the "flow region" below the pits. This flow region was depleted in silicon. Some chloride was detected inside the pits along with silicon.

An attempt to produce an Auger spectrum inside the pits proved fruitless; once again charging resulted and manipulation of the beam voltage or current did not produce a stable spectrum.

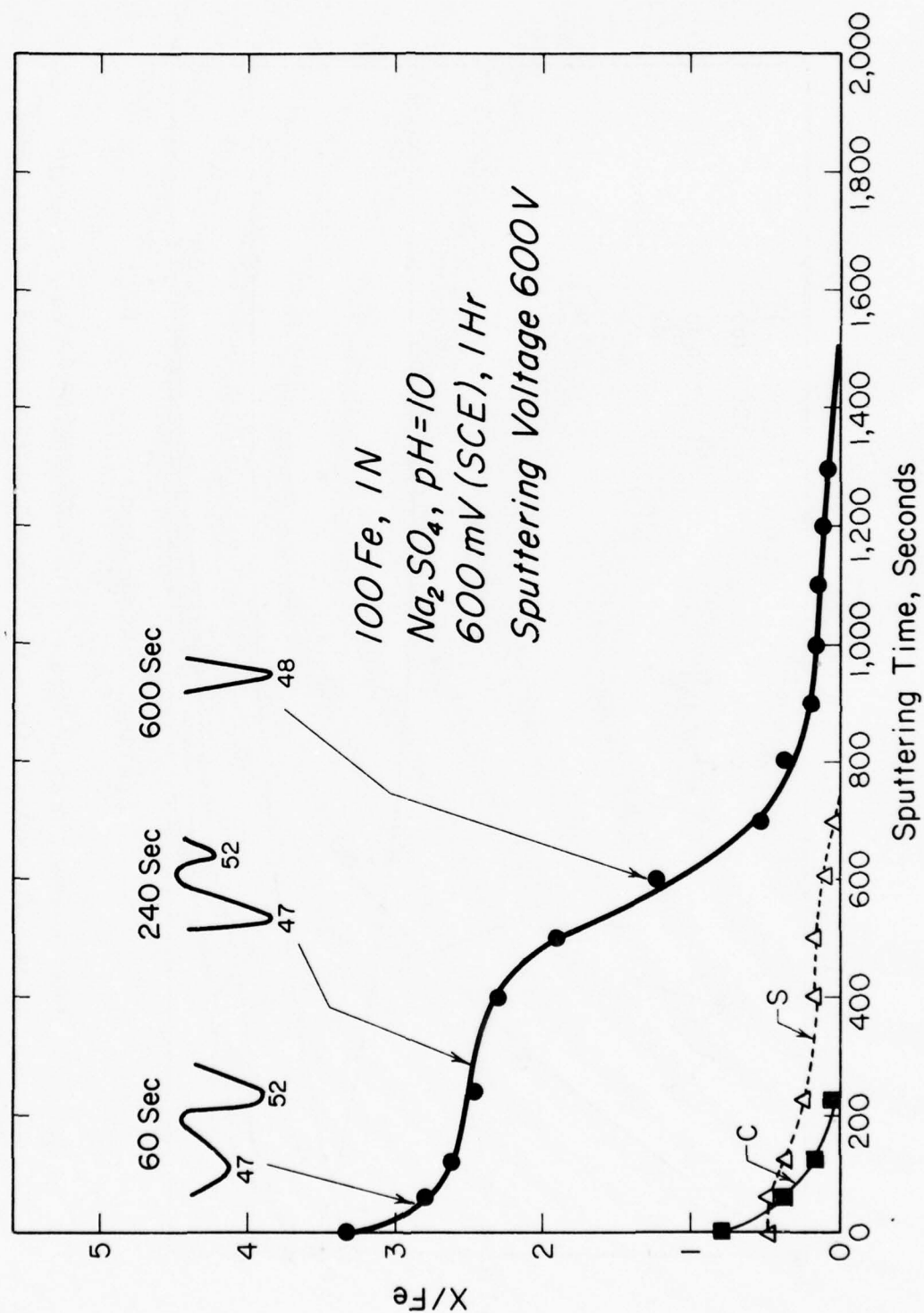


Figure 48. Auger compositional profile of film formed on iron in 1N sodium sulfate, pH = 10.

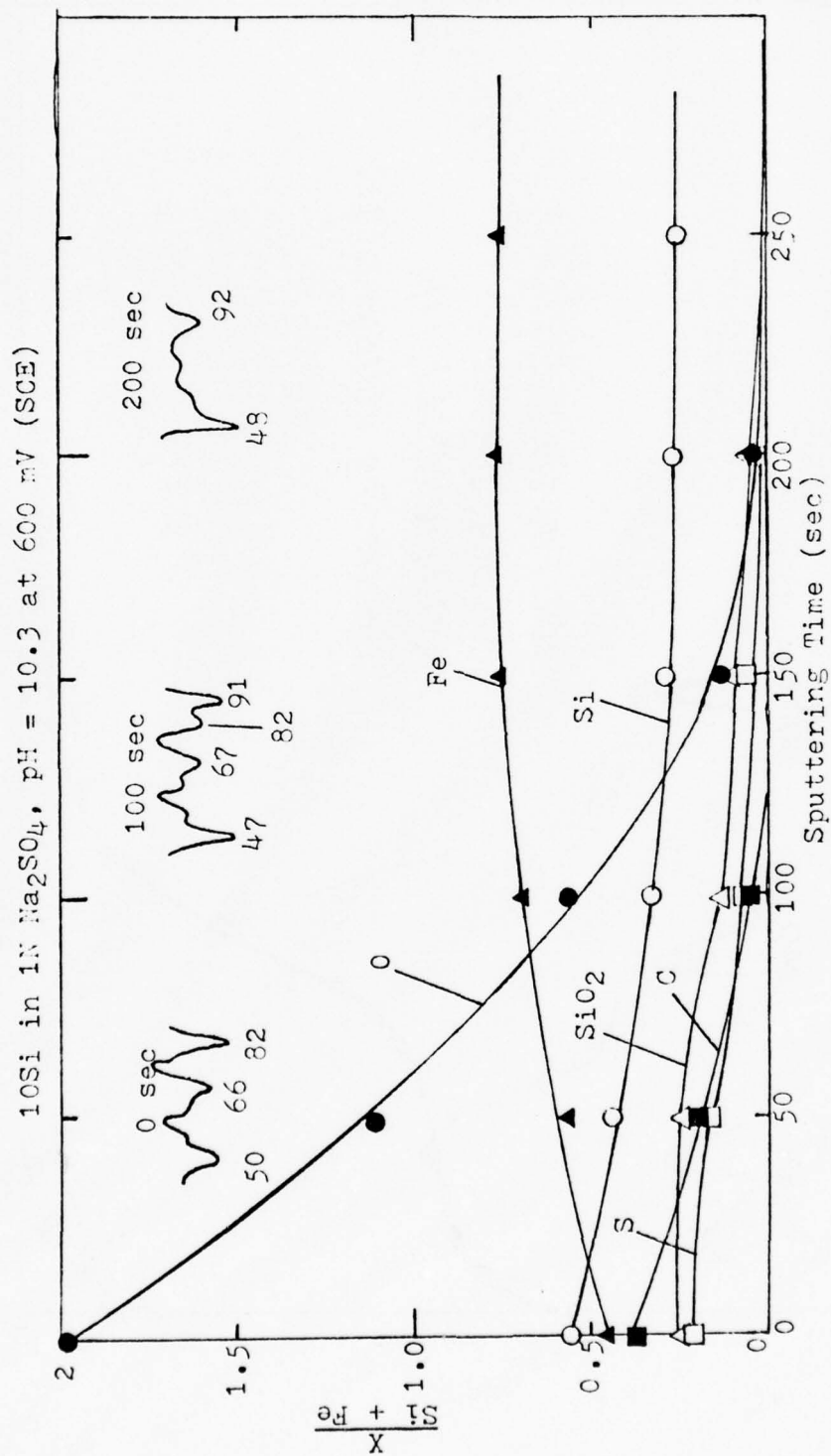


Figure 49. Auger compositional profile of film formed on 10Si sample polarized in 1N sodium sulfate (pH = 10.3) at 600 mV (SCE) for 1 hr (sputtering voltage 600 V).

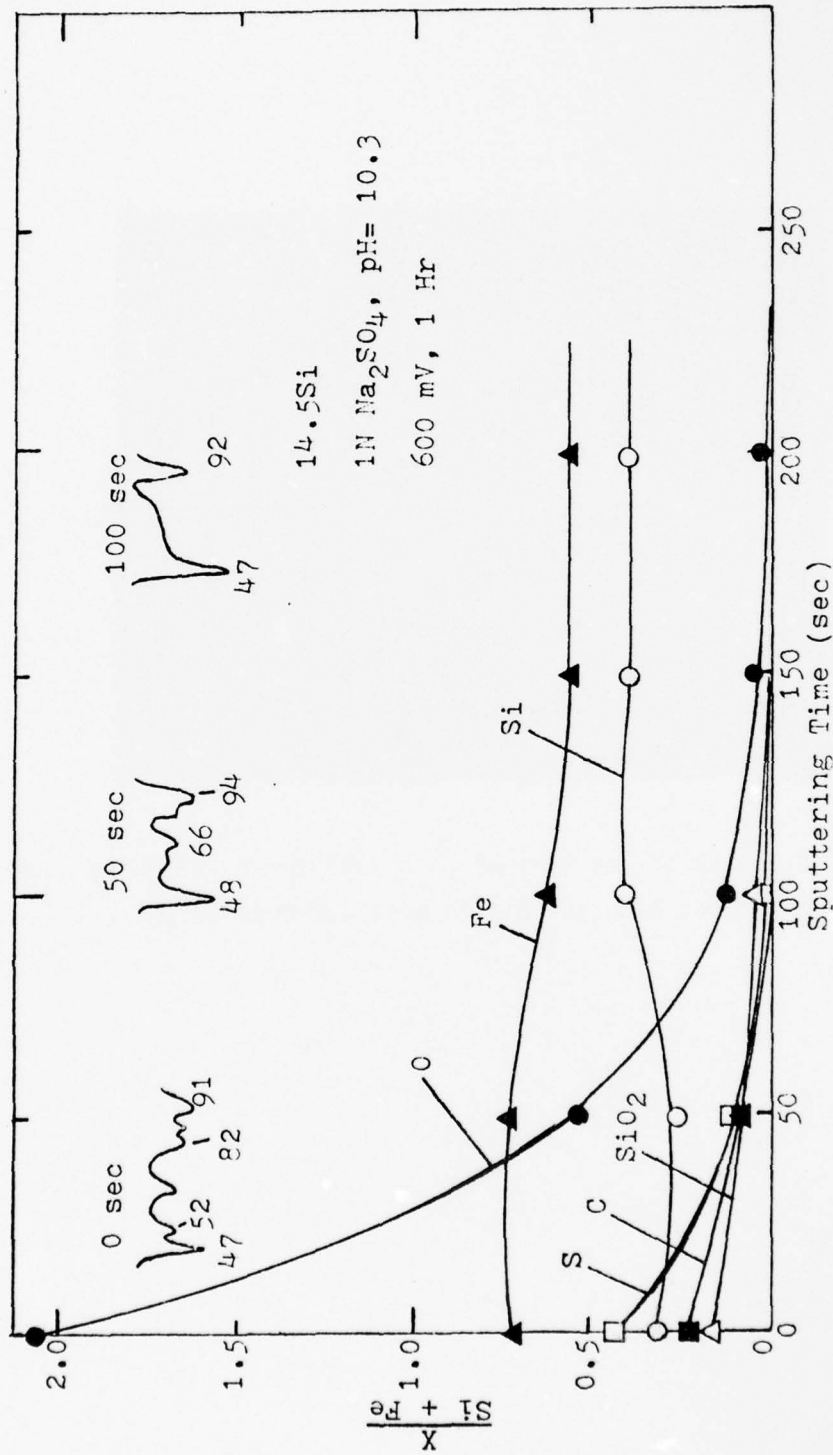


Figure 50. Auger compositional profile of film formed on 14.5Si sample polarized in 1N sodium sulfate (pH = 10.3) at 600 mV (SCE) for 1 hr (sputtering voltage 600 V).





Figure 51. Examples of the type of pits analyzed by scanning Auger in Figure 7; note the etched area surrounding the pits.

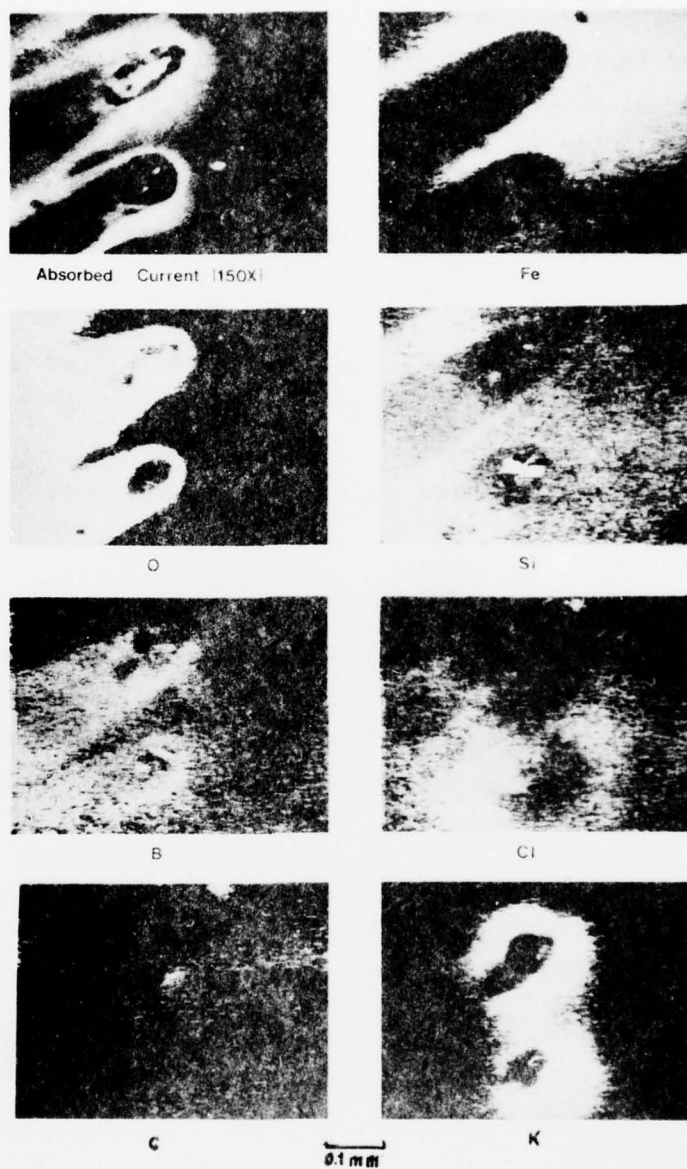


Figure 52. Scanning Auger elemental distribution of material around a pit formed on 8Si in borate buffer and 0.1M potassium chloride.

However, it was possible to obtain a composition profile of the "flow region." Figure 53 shows the profile. Oxygen and boron are concentrated in this region with a depletion of silicon in the area. The boron level does not change until the oxygen begins to do so indicating that the two elements are linked.

The area away from the pits proved almost film-free. Sixty seconds of sputtering removed all traces of foreign substances and produced a spectrum typical of a film free 8Si substrate. This profile is shown in Figure 54.

Similar results were obtained when 3Si was pitted in the same solution; a composition profile for the alloy is shown in Figure 55 for the flow region.

The 14.5Si alloy did not pit in this solution, so no AES was obtained.

#### 4.4.6 Film in 0.1N Sodium Chloride

The composition profile for 14.5Si in sodium chloride, pH = 6.5 held at 200 mV SCE for 1 hour is shown in Figure 56. The film shows a continuous sputtering of oxygen with minor amounts of sodium and chloride incorporated in the film. Silicon is slightly enriched in the film.

#### 4.4.7 Average Film Composition Determination

To interpret the Auger results in terms of silicon enrichment or depletion in the films, a method to determine the average Si/(Si + Fe) composition ratio in the oxide was found (33). The average ratio is given by

$$\left(\frac{\text{Si}}{\text{Si} + \text{Fe}}\right)_{\text{avg}} = (1/t_{\text{O/A}}) \int_0^{t_{\text{O/A}}} \left(\frac{\text{Si}}{\text{Si} + \text{Fe}}\right) dt \quad (14)$$

where  $t$  is the sputtering time,  $t_{\text{O/A}}$  is the time to sputter to the oxide/alloy interface.  $(\text{Si}/(\text{Si} + \text{Fe}))_{\text{avg}}$  may be determined by numerical integration of the area under the Si/(Si + Fe) and  $\text{SiO}_2/(\text{Si} + \text{Fe})$  curves in each of the profiles; each of these curves were integrated

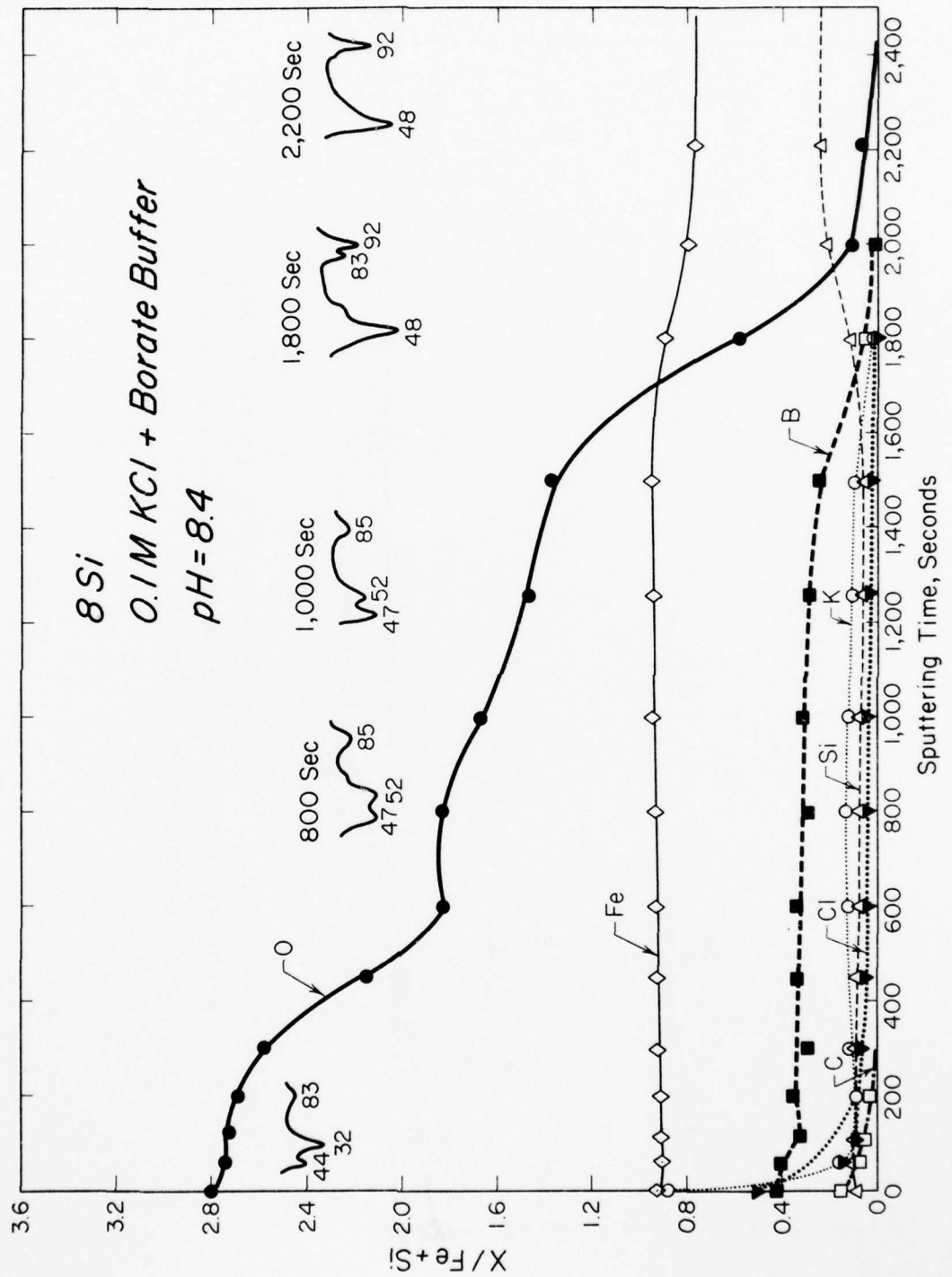


Figure 53. Auger compositional profile of material in "flow region" around pit in 8Si.

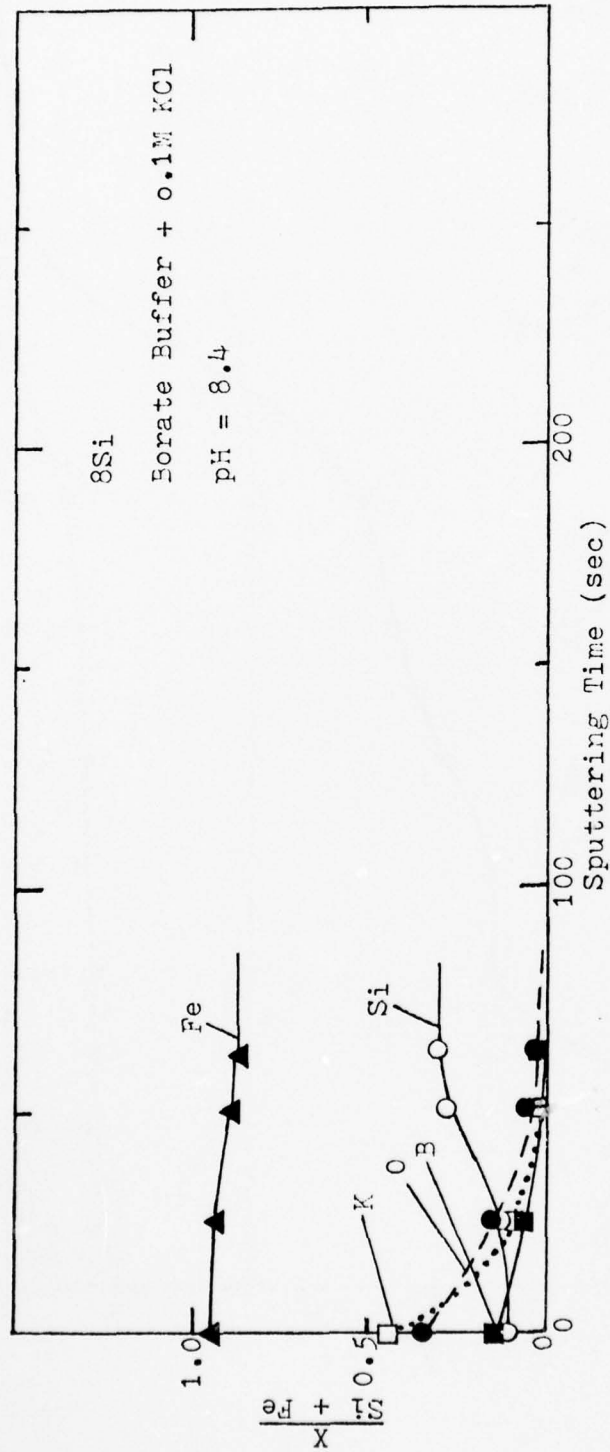


Figure 54. Auger compositional profile of unpitted area on 8Si sample on which pits formed in borate buffer plus 0.1M potassium chloride solution (sputtering voltage 600 V).



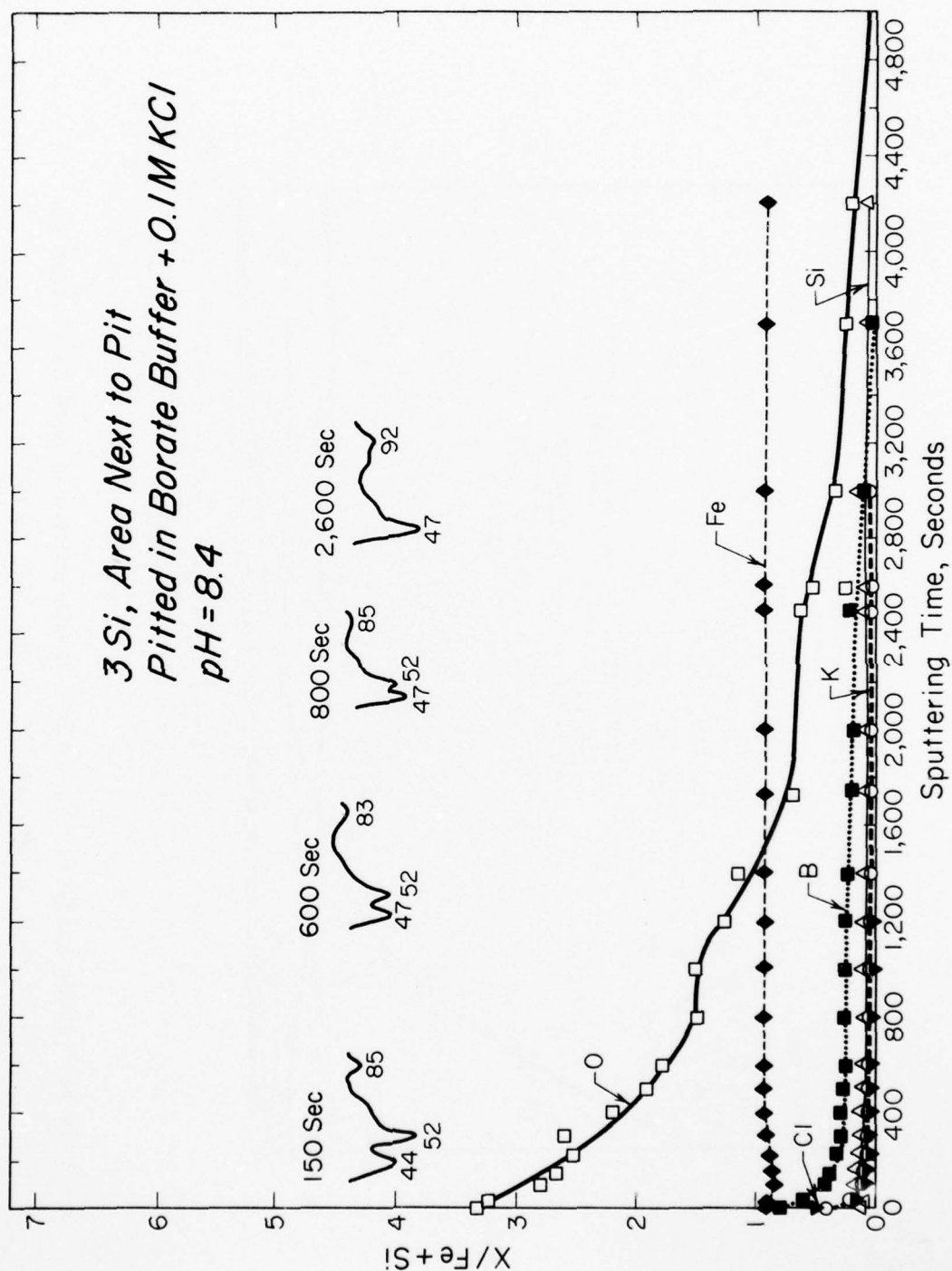


Figure 55. Auger compositional profile of material in "flow region" around pit in 3Si.

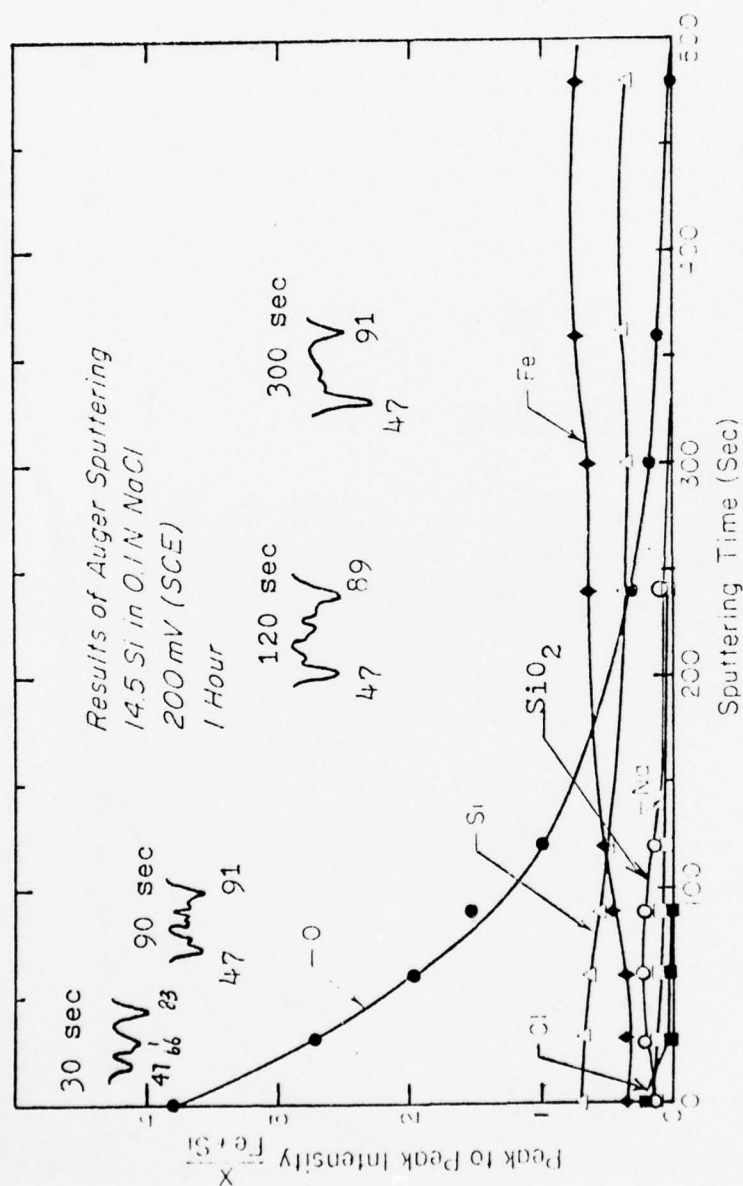


Figure 56. Auger analysis on a 14.5Si sample which had been passivated for 1 hr in 0.1N NaCl at 200 mV SCE (440 mV NHE).

to account for all the silicon in the film. These results were added, divided by  $t_{O/A}$ , and then plotted as a function of the alloy composition,  $(Si/(Si + Fe))_{\text{alloy}}$ , which is the value obtained on the film free substrate.

This calculation was carried out for the films which formed in air; the result is shown in Figure 57. A similar approach was used for the films from the borate buffer solution and is shown in Figure 58. Figure 59 is the result for the anodic films from 1N sulfuric acid. Figure 60 is that for 1N sodium sulfate, pH = 3.2, and Figure 61 is that for pH = 6.4. The dashed lines on the figures are the result for equal concentrations of silicon in the alloy and in the film.

The results from these average film composition determinations together with the compositional profiles and the current decay curves presented in the next section will be used to explain the electrochemical effects observed in the discussion section of this work.

#### 4.5 Current Decay Curves in Sulfate Solutions

The current decay curves for the iron-silicon alloys are shown in Figures 62-65. The plots were obtained by polarizing the samples at a constant potential in the passive region and recording the current change with time. This process was repeated several times for each alloy and solution. The best fit line through the points was determined by the least squares method. Thus, the points represent a statistical average; the points on the lines shown in the graphs of these results are indicative of the amount of scatter encountered.

The scatter was so great because reproducibility of these curves was low. General trends could be noted but the current values did not reproduce. This problem is similar to that encountered by other workers (9) who experienced difficulties in reproducing the same passive current values when generating polarization curves in the iron-silicon alloy system.

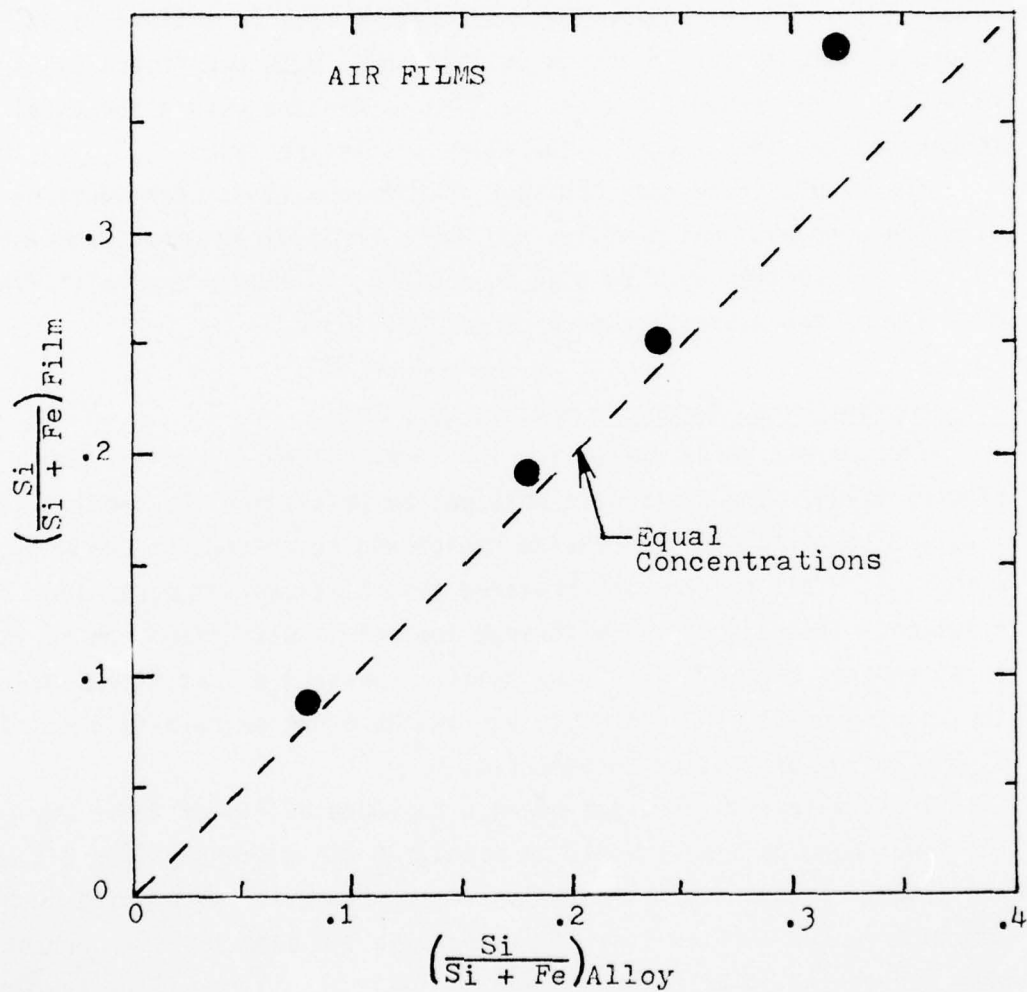


Figure 57. Average air oxide film Si content vs alloy silicon content. Dashed line represents equal concentrations in the oxide and the alloy.

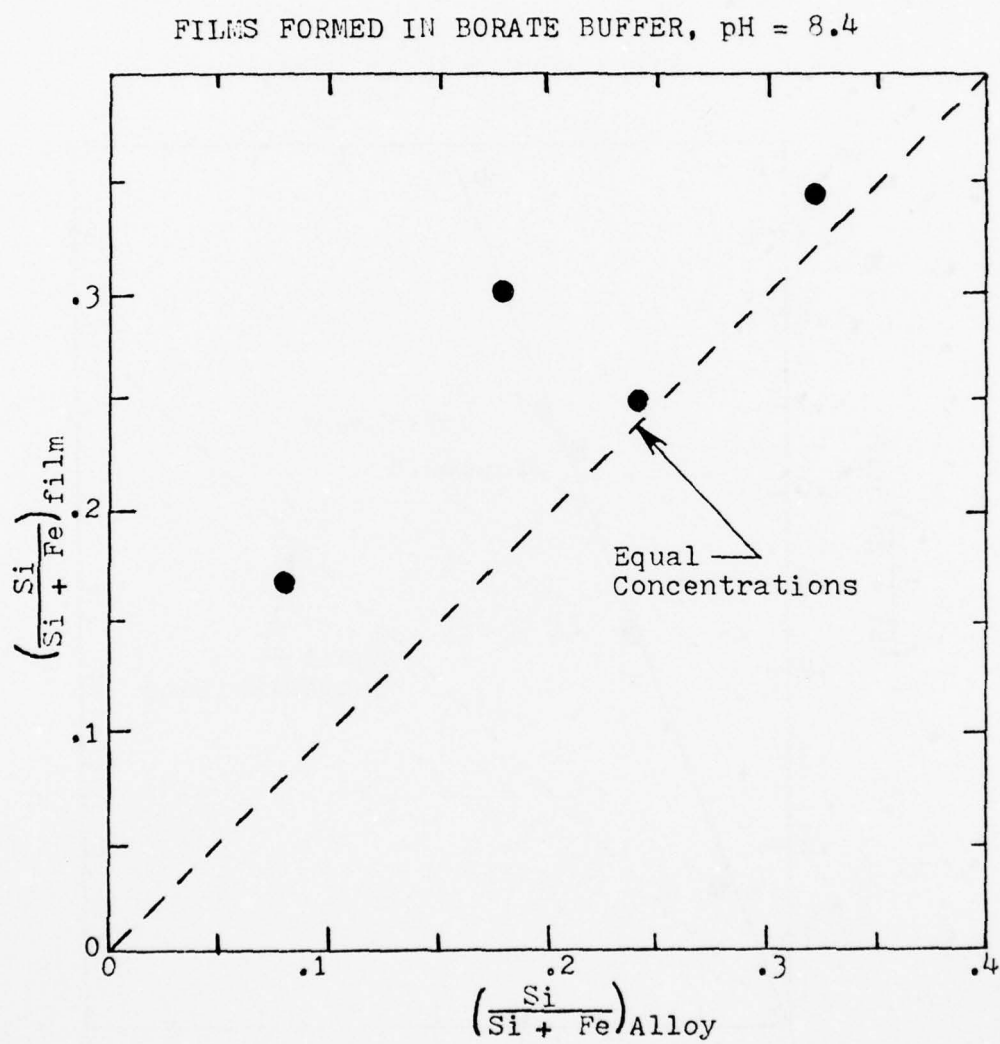


Figure 58. Average anodic oxide film Si content vs alloy Si content. Dashed line represents equal concentrations in the oxide and the alloy.



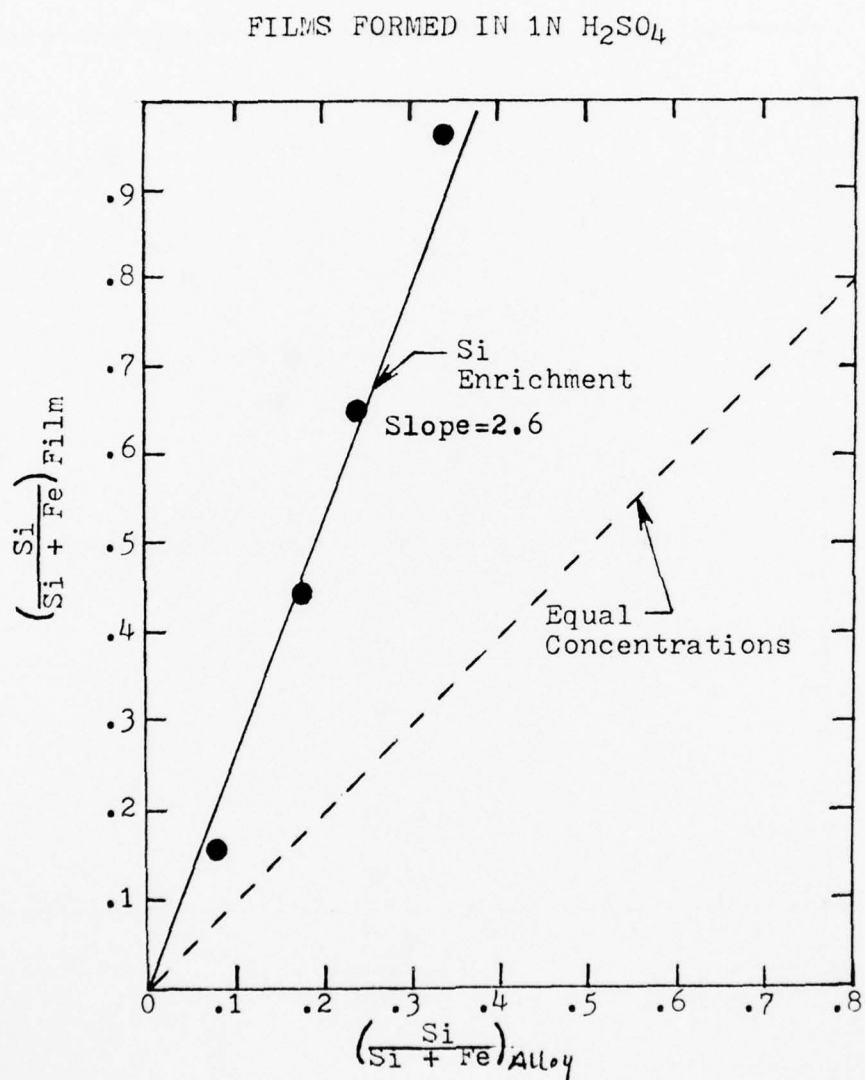


Figure 59. Average anodic oxide film silicon content vs alloy silicon content. Dashed line represents equal concentrations in the oxide and the alloy.

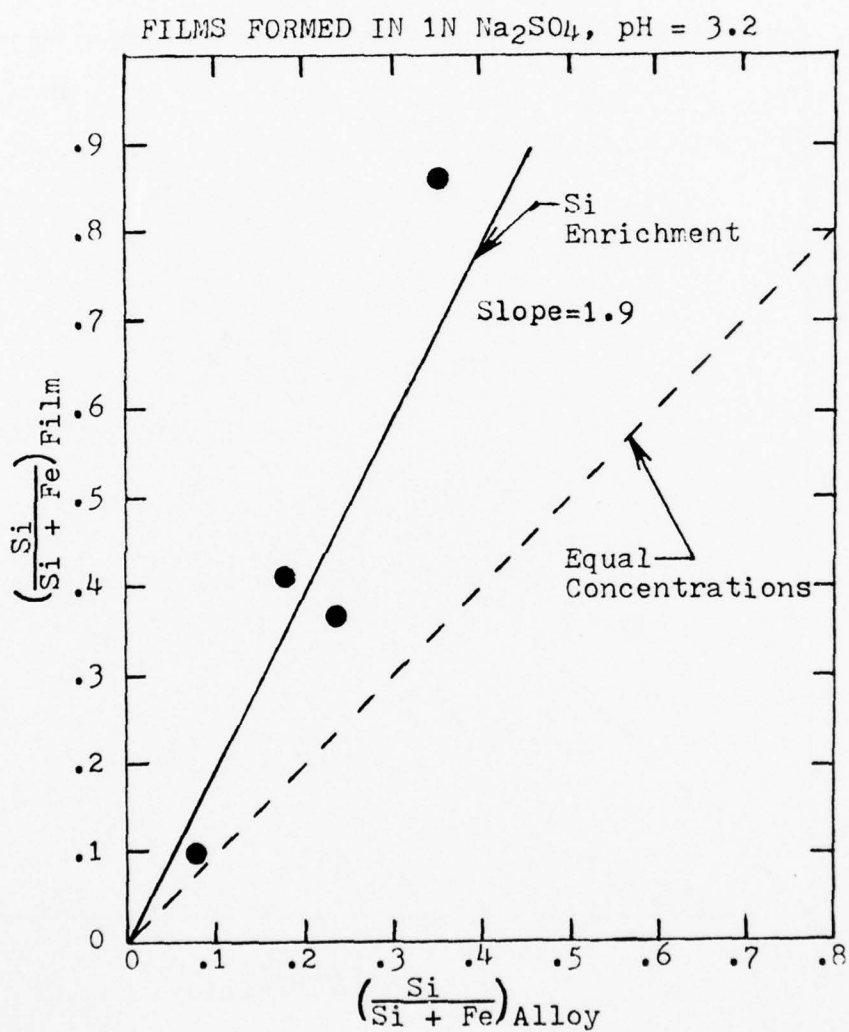


Figure 60. Average anodic oxide film Si content vs alloy Si content. Dashed line represents equal concentrations in the oxide and the alloy.

FILMS FORMED IN 1N Na<sub>2</sub>SO<sub>4</sub>, pH = 6.4

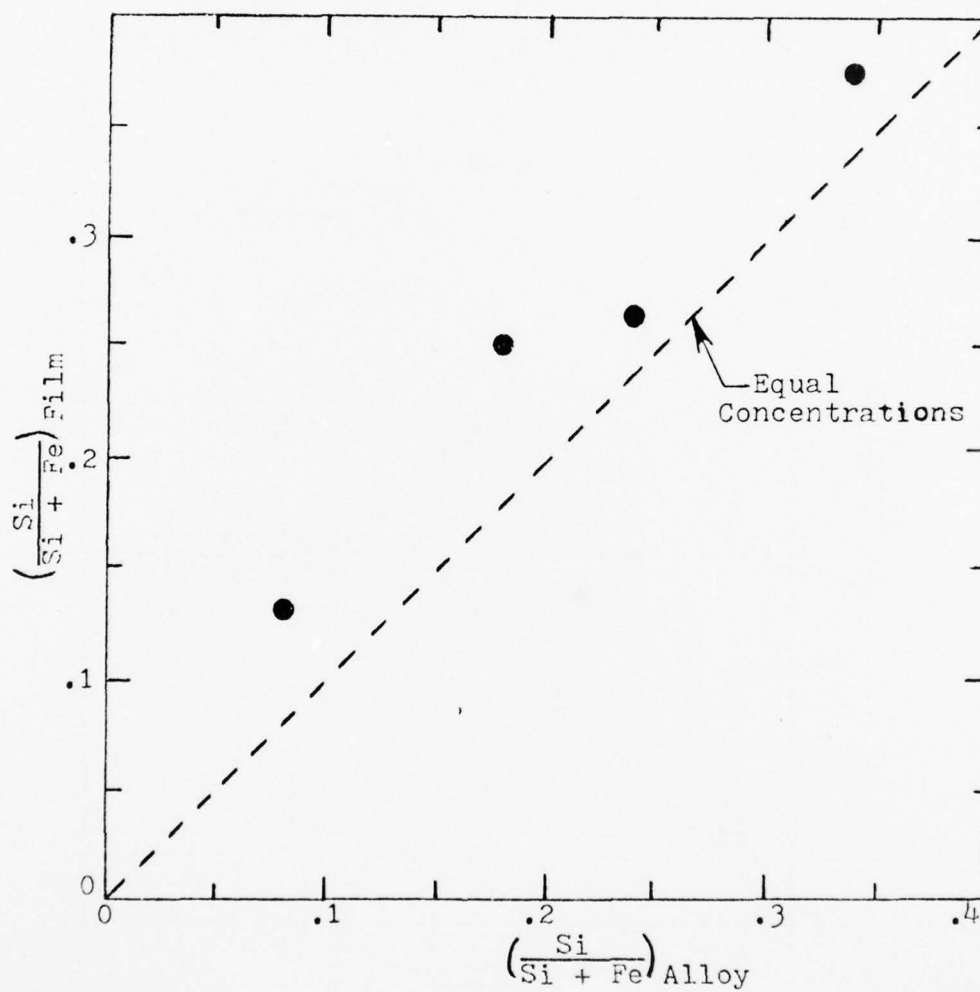


Figure 61. Average anodic oxide film Si content vs alloy Si content. Dashed line represents equal concentrations in the oxide and the alloy.

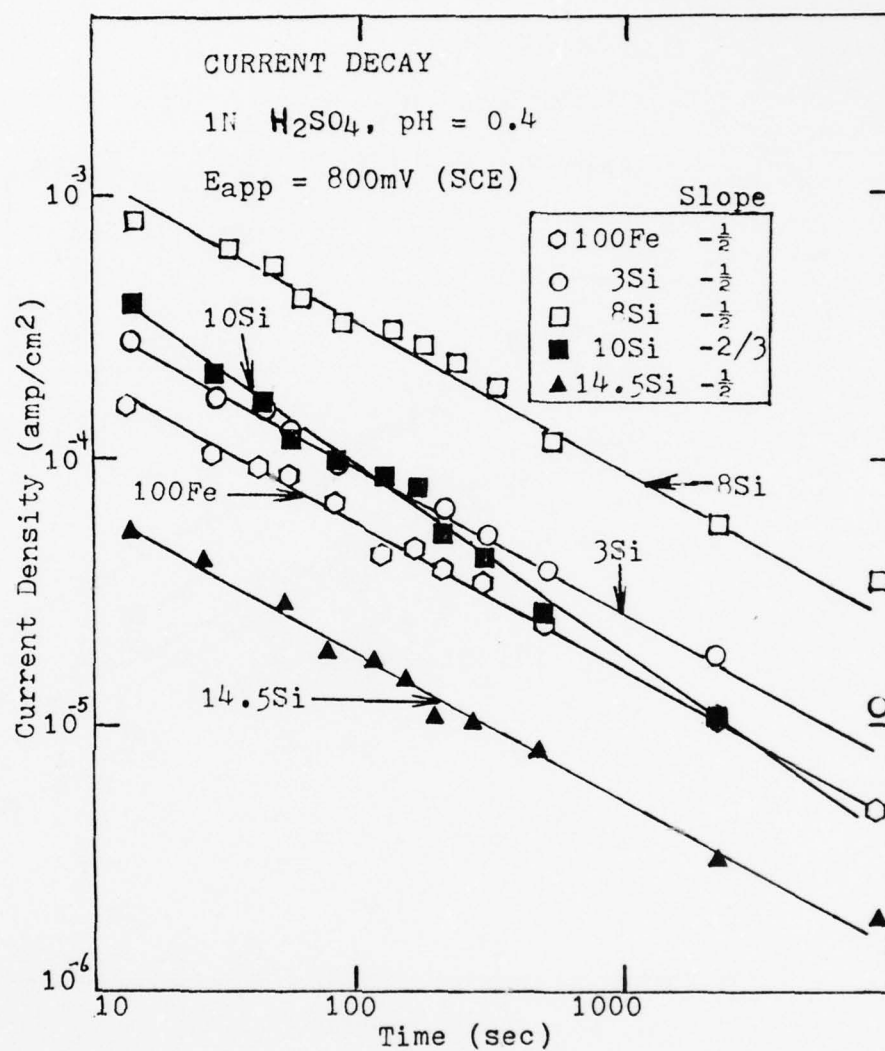


Figure 62. Current decay curves for iron-silicon alloys in 1N  $\text{H}_2\text{SO}_4$ , pH = 0.4,  $E_{\text{app}} = 800\text{ mV (SCE)}$ ,  $1040\text{ mV (NHE)}$ .

AD-A058 326

OHIO STATE UNIV RESEARCH FOUNDATION COLUMBUS  
FUNDAMENTAL STUDIES OF DISSOLUTION AND PASSIVITY OF ALLOYS AND --ETC(U)  
JUL 78 J B LUMSDEN, R W STAEHLE, L ABREGO  
OSIRE-7A4131-3

F/G 11/6

N00014-75-C-0665

NL

UNCLASSIFIED

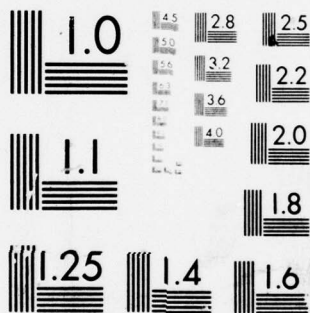
2 of 2

AD  
A068326



END  
DATE  
FILMED  
10-78  
DDC





MICROCOPY RESOLUTION TEST CHART  
NATIONAL BUREAU OF STANDARDS-1963-A

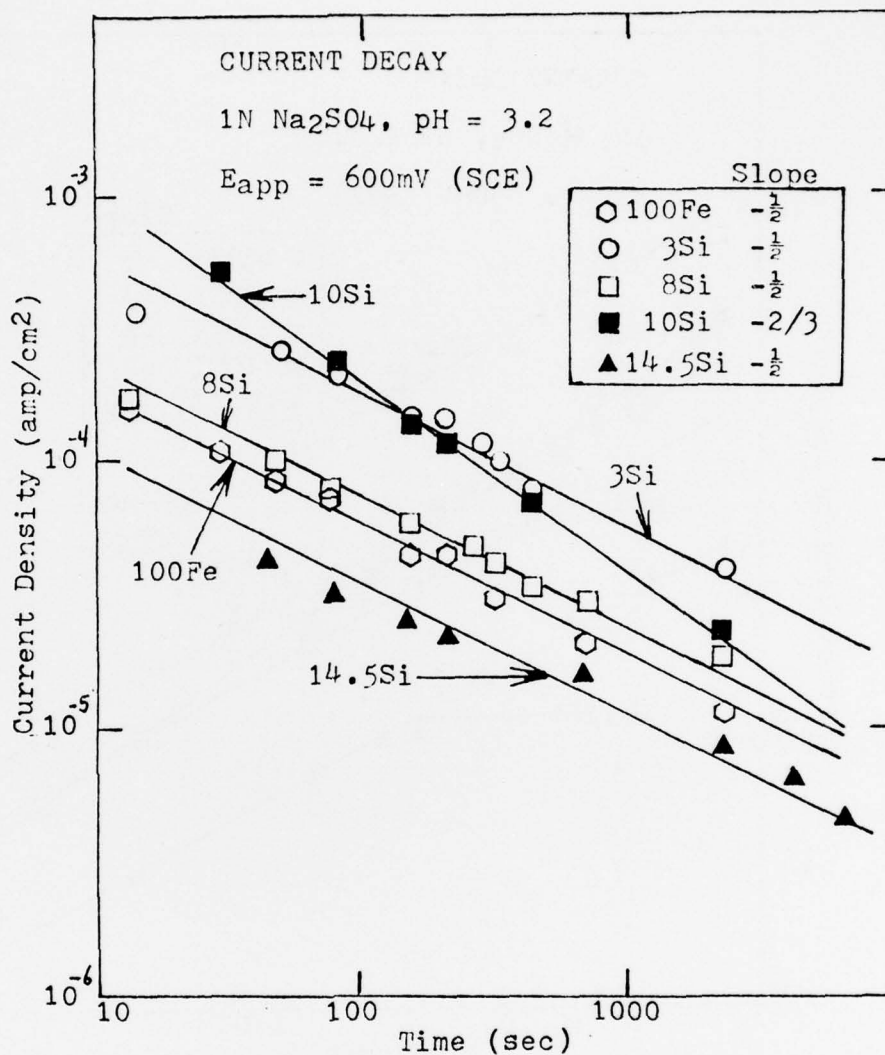


Figure 63. Current decay curves for iron-silicon alloys in 1N Na<sub>2</sub>SO<sub>4</sub> = pH = 3.2, E<sub>app</sub> = 600 mV (SCE), 840 mV (NHE).

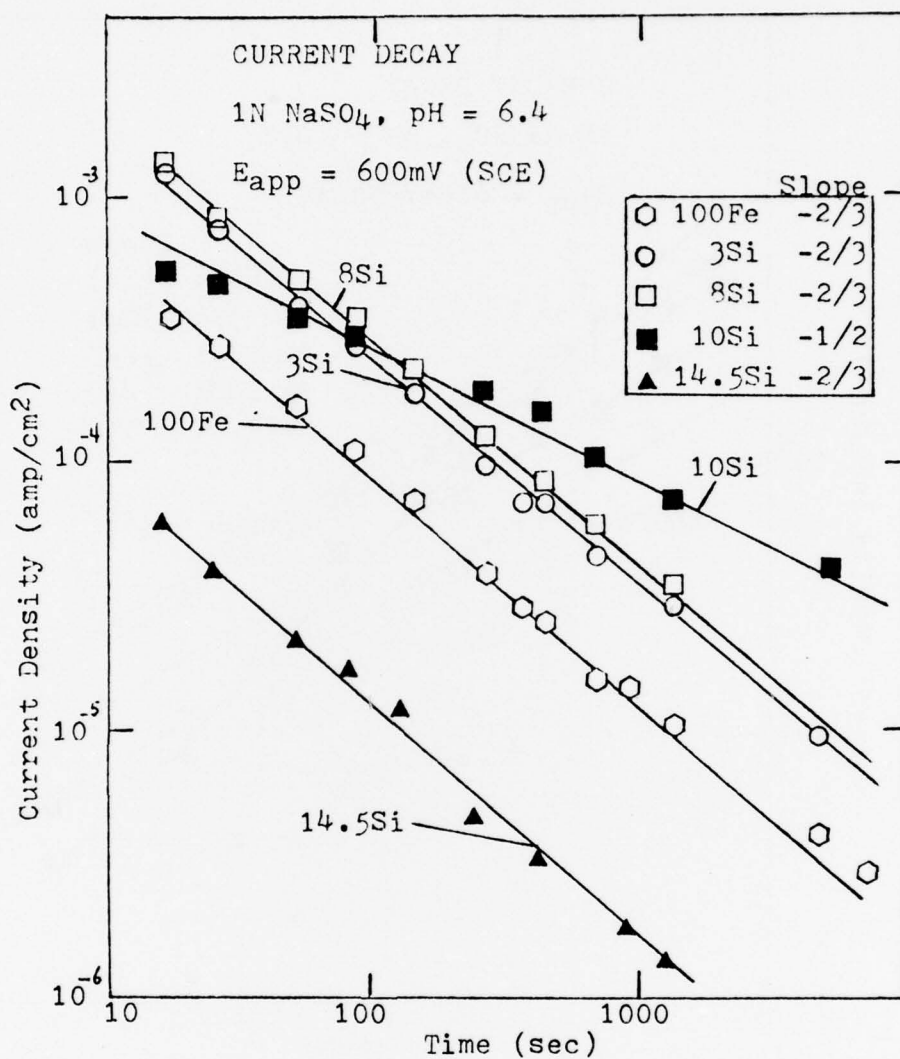


Figure 64. Current decay curves for iron-silicon alloys in 1N Na<sub>2</sub>SO<sub>4</sub>, pH = 6.4,  $E_{app} = 600\text{ mV (SCE)}$ , 840 mV (NHE).

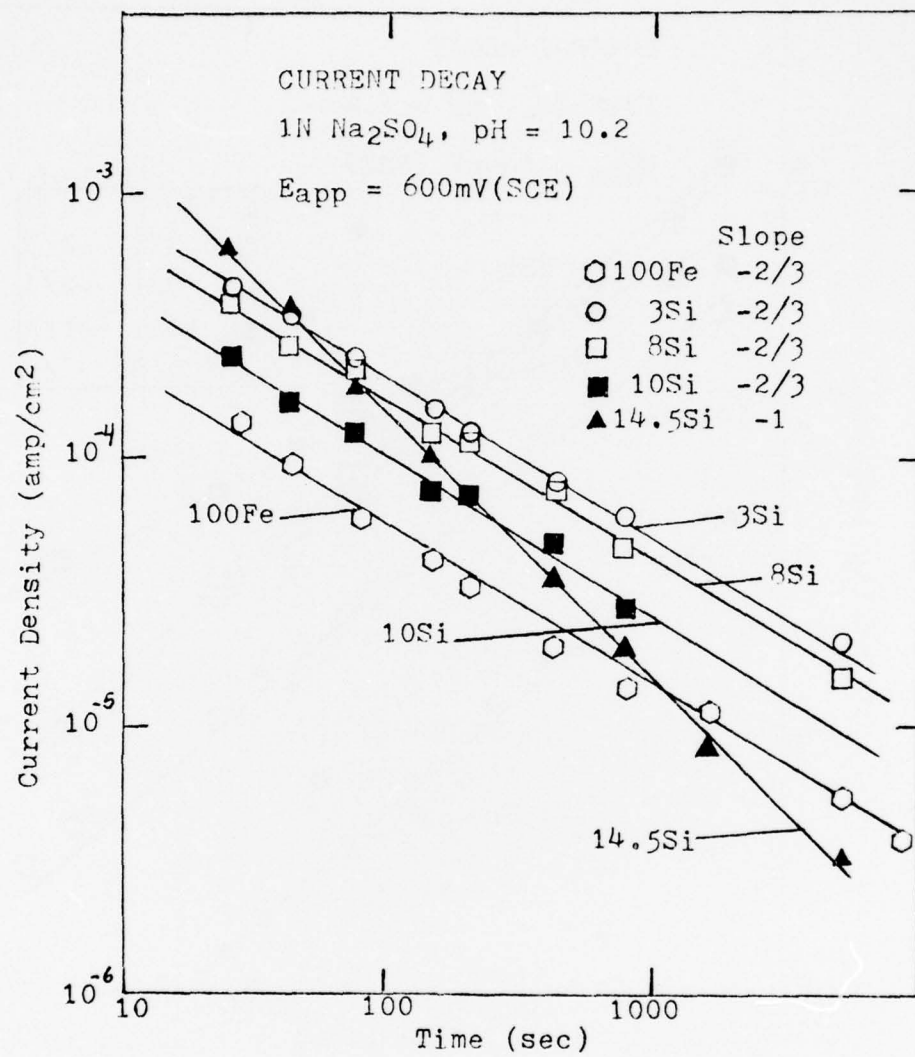


Figure 65. Current decay curves for iron-silicon alloys in 1N Na<sub>2</sub>SO<sub>4</sub>, pH = 10.2, E<sub>app</sub> = 600 mV (SCE), 840 mV (NHE).

Also the oscillations which accompany passivation in the sulfate system (34, 35, 36, 37) were noted even in the passive state. The effect of these sudden jumps in the current was that the current did not always return to a value as low as it had prior to the oscillation. These oscillations would occur every few minutes. The effect may be that they obscure the true passive current and make it difficult to determine the true current value.

Table IV lists the slopes obtained from the solutions as a function of composition, pH and potential.

## 5.0 DISCUSSION

### 5.1 Introduction

This investigation was undertaken to determine if a silica film is responsible for the corrosion resistance of iron-silicon alloys. It had previously been noted that the benefit of silicon additions was not reached until the alloy contained 14.5 wt % (25 at %) silicon. This study has shown by AES and electrochemical measurements that a protective film of  $\text{SiO}_2$  forms on this alloy. And it is this film which is responsible for the electrochemical behavior of this alloy. Silicon enrichment was noted in all the binary alloys studied, but it is not effective until the film consists predominantly of  $\text{SiO}_2$ .

This discussion is divided into the main issues which were studied and what effect the alloy composition had on the subsequent results. These effects include (1) the polarization potential, (2) the passivity of the alloys, (3) the variation of solution pH, (4) the breakdown of passivity, and the effect of the electrolyte anion. These topics are discussed in terms of the electrochemical and AES results.

### 5.2 The Polarization Potential

By studying a series of alloys in which the silicon content varies, it is possible to note the effect that alloy composition exerts on the corrosion potential in a solution.



TABLE IV  
SLOPES FROM CURRENT DECAY CURVES  
IN SULFATE SOLUTIONS

Potential (SCE) mV	800	600	600	600
pH	0.4	3.2	6.4	10.3
Alloy				
100Fe	$-\frac{1}{2}$	$-\frac{1}{2}$	$-\frac{2}{3}$	$-\frac{2}{3}$
3Si	$-\frac{1}{2}$	$-\frac{1}{2}$	$-\frac{2}{3}$	$-\frac{2}{3}$
8Si	$-\frac{1}{2}$	$-\frac{1}{2}$	$-\frac{2}{3}$	$-\frac{2}{3}$
10Si	$-\frac{2}{3}$	$-\frac{2}{3}$	$-\frac{1}{2}$	$-\frac{2}{3}$
14.5Si	$-\frac{1}{2}$	$-\frac{1}{2}$	$-\frac{2}{3}$	-1

Figure 66 shows the effect of alloy composition in terms of atomic % silicon on the corrosion potential,  $E_r$ , in the borate buffer and sulfate solutions. It is apparent that in the 0 to 3 pH region, additions of less than 15 at % silicon shifts the corrosion potential very slightly. It is not until 25 at % (14.5 wt %) silicon is reached that there is a large shift of  $E_r$  in the noble direction. Since the low silicon alloys are composed of a solid solution ferrite matrix (37),  $E_r$  is not greatly affected.

But with 25 at % the change in  $E_r$  represents the increased corrosion resistance of this alloy in the acid solutions in accordance with the superposition of the Pourbaix diagrams of iron-water and silicon-water. Superposition of the equilibrium diagrams indicate that in the low pH region, if sufficient silicon is present in an alloy, then an alloy might evolve which has a protective oxide in the acid pH region. The results indicated in Figure 66 show that this point is approached when the silicon content reaches 25 at %.

In the neutral to basic pH solutions the addition of silicon to the alloy becomes less effective. At pH = 10, an alloy with 25 at % silicon has an active corrosion potential which is an effect explained by the Pourbaix diagrams. Figure 1b, which shows the silicon-water system, indicates that  $\text{SiO}_2$  is soluble around pH = 10. Consequently, the corrosion potential of the high silicon alloy is dominated by the silicon reaction, whereas the alloys containing less silicon are dominated by both iron and silicon reactions.

The silicon content also affected the potentials at which the alloys passivated as they were anodically polarized. The passivation potential,  $E_p$ , vs silicon content (at %) in the sulfate solutions are shown in Figure 67. It shows that increasing the silicon content to 18 at % (8Si) shifted  $E_p$  to less negative values which in effect extended the region of active dissolution, an undesirable situation for alloy development.

However, 25 at % silicon had a passivation potential close to its corrosion potential. This significantly narrowed the dissolution region.

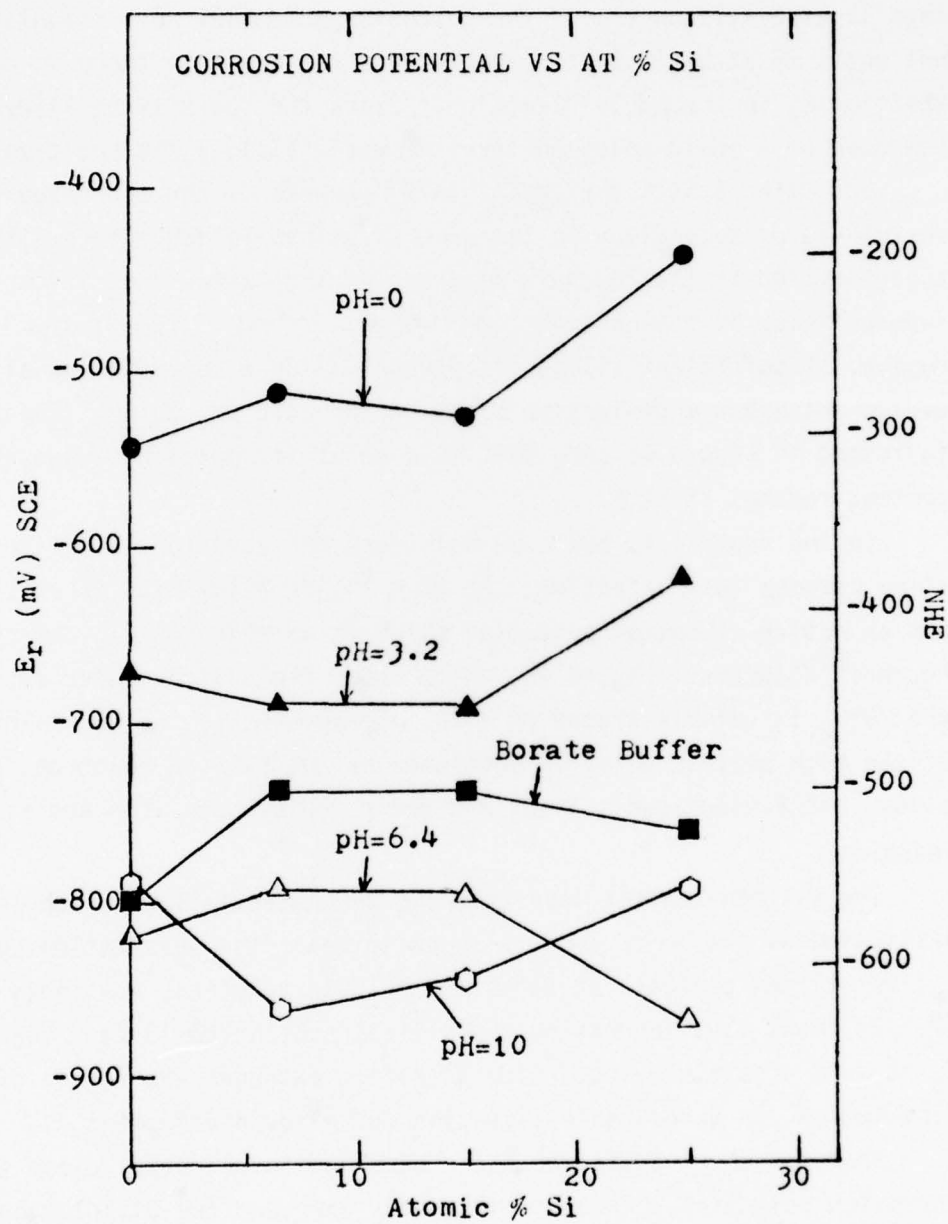


Figure 66. The change in the corrosion potential  $E_r$  as a function of alloy Si content (at %).

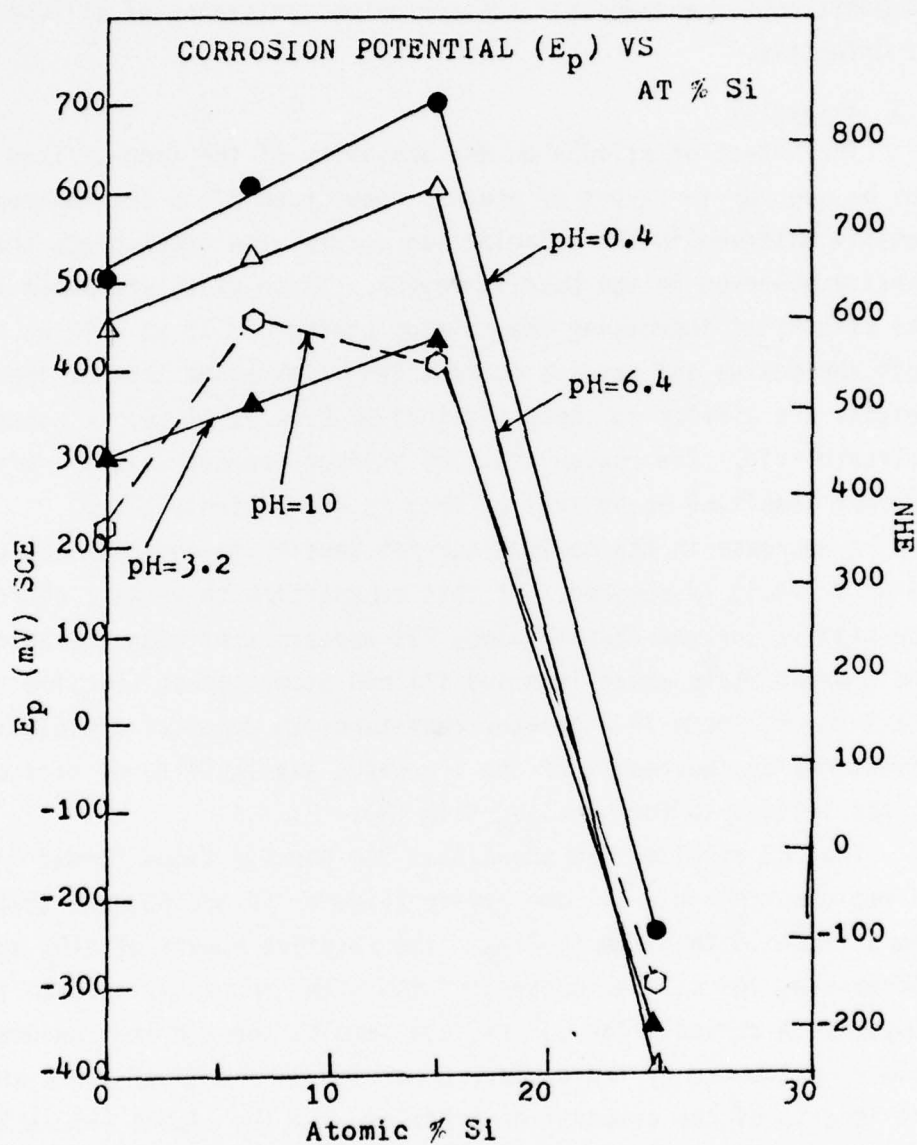


Figure 67. The change in passivation potential,  $E_p$ , as a function of alloy Si content (at %).

The passive film on this alloy had the largest potential stability range. This behavior reflects the effect of  $\text{SiO}_2$  as predicted by the silicon-water Pourbaix diagram. Apparently it is not until the 25 at % (14.5 wt %) composition is reached that the corrosion resistance of silicon alloying is effective.

### 5.3 Passivity

The effect of silicon on the passivity of the iron-silicon alloys can be seen by two types of graphs. One graph plots the maximum current density observed in the polarization curves; the other plots the current density observed in the passive region. These plots are shown in Figure 68. The effects of increasing the silicon content to 15 at % (8 wt %) increases both the active and passive current densities above that of iron. These results are similar to those obtained by Crow et al (9) in concentrated sulfuric acid. The reason that low silicon concentrations increases the current densities above that of iron is not entirely clear.

A decrease in the maximum current density is not obtained until 25 at % (14.5) is reached. At this composition there is a decrease in the passive current density also. It appears that when the alloy reaches the ordered state where iron and silicon atoms occupy specific sites in the lattice, there is a greater resistance to chemical dissolution. This effect may be the result of the increased availability of silicon atoms in the lattice to form an  $\text{SiO}_2$  film (8).

The AES results have shown that the passive films formed in the low pH regions contain a silicon excess (Figures 59 and 60) and that some of the silicon in the film is  $\text{SiO}_2$ . The relative amount of  $\text{SiO}_2$  appears to increase as the silicon content of the alloy increases as seen in the film composition curves. The low silicon samples contain iron oxides in the film as evidenced by the appearance of the 44 and 52 eV lines shown in the inserts of the composition profiles. In the 14.5Si (25 at %) sample there is little evidence of the two low energy iron oxide lines; the



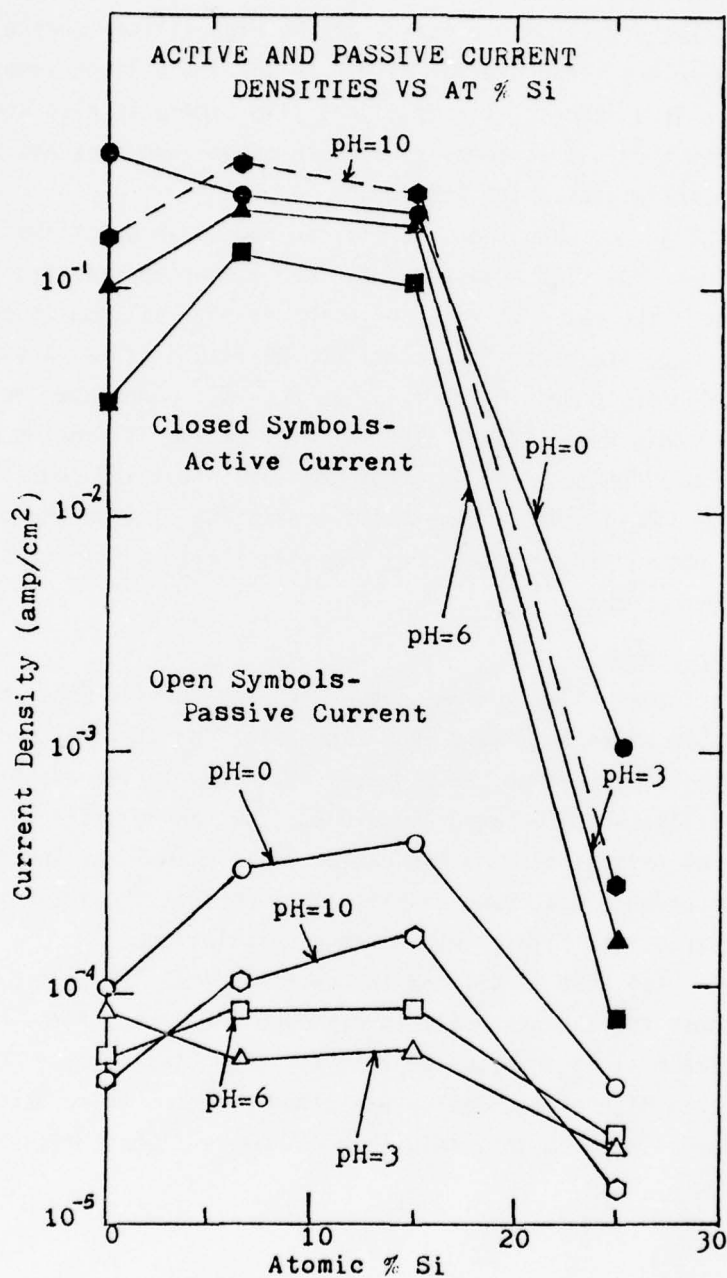


Figure 68. The change in active and passive current densities as a function of alloy silicon content (at %).

47 eV line predominates which is associated with uncombined iron. Consequently, the corrosion resistance of the high silicon sample is due primarily to a silicon dioxide film. In the low silicon samples, although there is an excess silicon in the film, there is also some iron oxide such that the film is composed of both oxides and does not afford the corrosion resistance which  $\text{SiO}_2$  does.

Figures 59 and 60 show that the silicon excess in the films falls along a straight line with a slope of 2.6 and 1.9, respectively; the slopes represent the ratio of silicon in the film to silicon in the alloy. However, the increased corrosion resistance of 14.5Si (25 at % silicon) has been attributed to an  $\text{SiO}_2$  film (1, 2, 4-6, 8). The Auger results have confirmed this proposition. The ratio of excess silicon in all the alloys in the acid pH solution is about the same. But the low silicon samples (3Si and 8Si) have passive films consisting of iron and silicon oxides which are not as protective as the silica film which forms at higher silicon concentrations.

#### 5.3.1 Current Decay

The effect that alloy composition has on the current decay behavior of the alloys is shown in Figure 69. Increasing the silicon concentration in the alloy does not change the slope of the decay curves except for the 18 at % (10Si) alloy, which behaved anomalously; no reason was determined for the behavior of this alloy. No indication of logarithmic or inverse logarithmic dependence was found despite the fact that these two rate laws are forwarded for film growth in aqueous solutions.

At 25 at % (14.5 wt %) silicon the current densities were consistently lower than those for the other alloys although the slope of the current density vs time plot is the same as that for the other alloys. However, at pH = 10, this high silicon alloy exhibited kinetics which deviated from the other alloys; in that solution, an inverse logarithmic expression was obtained.

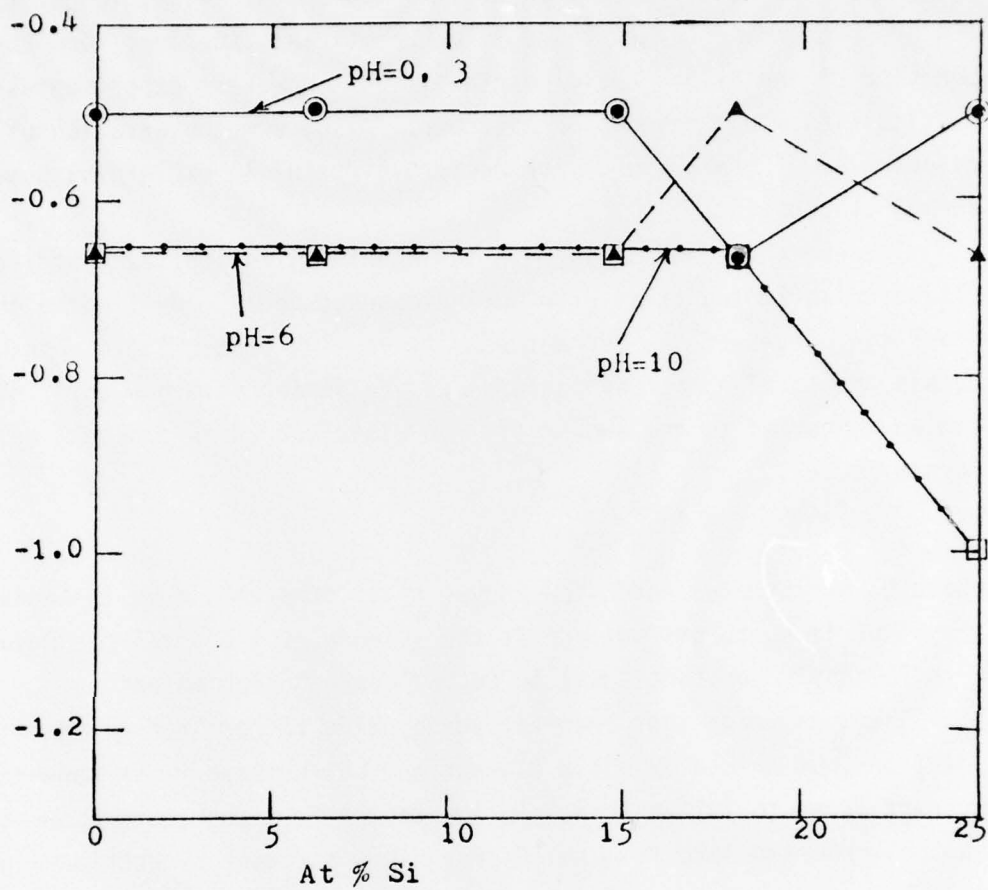


Figure 69. The change in slopes of the current density vs time plots as a function of silicon content of the alloy (at %).

Since the current decay curves were only obtained at one potential for each alloy, no relation between potential and current decay was obtained. Further work in this area is indicated. Also, longer times (24 hrs) for the decay curve would be beneficial; the long term corrosion behavior of the alloys could be classified. However, experimental difficulties would have to be overcome. Also, some observation of the dissolution of grain boundaries may prove useful in explaining some of the anomalous behavior.

The enrichment of silicon in the anodic films implies that iron has dissolved while the films grew during current decay. By finding the area under the curves of the current density vs time plots, it is possible to obtain the total number of coulombs passed during film growth. This amount can be converted to the amount of iron dissolved ( $W$  in  $\text{gms/cm}^2$ ) by Faraday's Law,

$$W = \frac{Q_T \cdot M}{n \cdot F}$$

where  $Q_T$  is the area under the curve in  $\text{coulombs/cm}^2$ ;  $M$  is the molecular weight of iron, 56  $\text{gms/mole}$ ;  $n$  is the valence, 2.5  $\text{equivalents/mole}$ ; and  $F$  is Faraday's constant equal to 96,500  $\text{coulombs/equivalent}$ .

Then, assuming that iron formed an oxide rather than going into solution (not a totally valid assumption, but necessary for converting current decay to film thickness), the weight from the above expression can be converted into film thickness. This was done by considering only one oxide,  $\text{Fe}_2\text{O}_3$ , and calculating how many grams of the oxide the above weight would yield. This value was divided by the oxide density, 5.15  $\text{gms/cm}^3$ , to yield a thickness.

These results are plotted in Figure 70 as a function of the silicon content in the alloy.

However, the true film thickness can be approximated from the Auger composition profiles using a sputtering rate of 1-3  $\text{\AA/min}$ . These results are also plotted vs silicon content in the alloy and are shown in Figure 71.

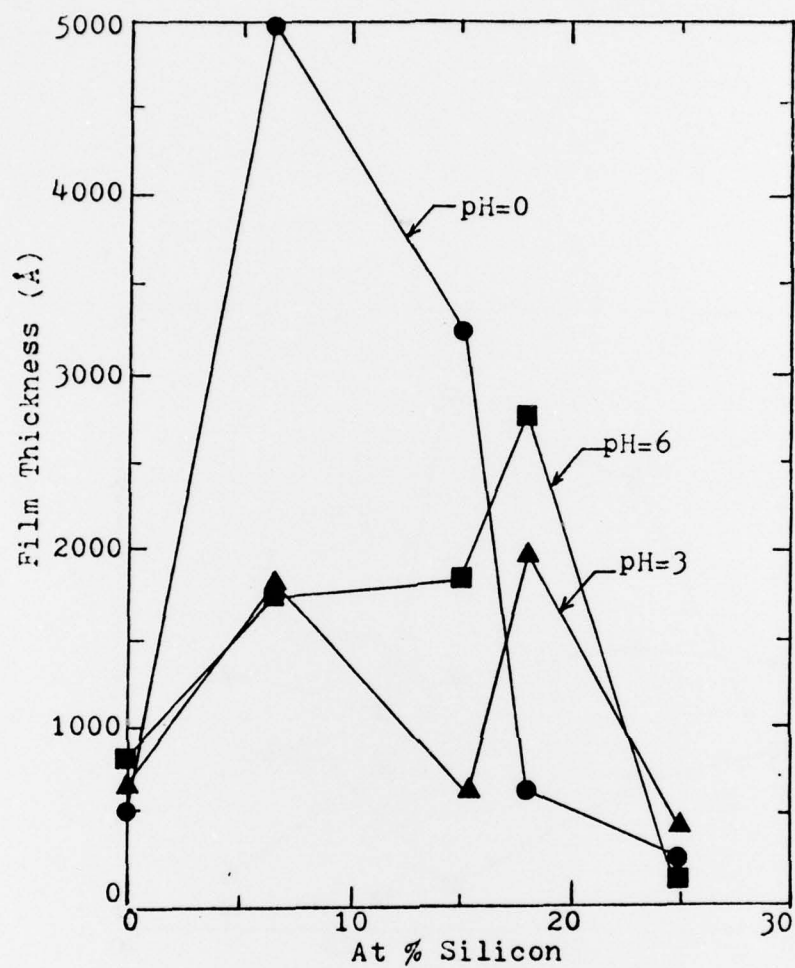


Figure 70. Film thickness calculated from the total charge passed during current decay plotted vs atomic % silicon.



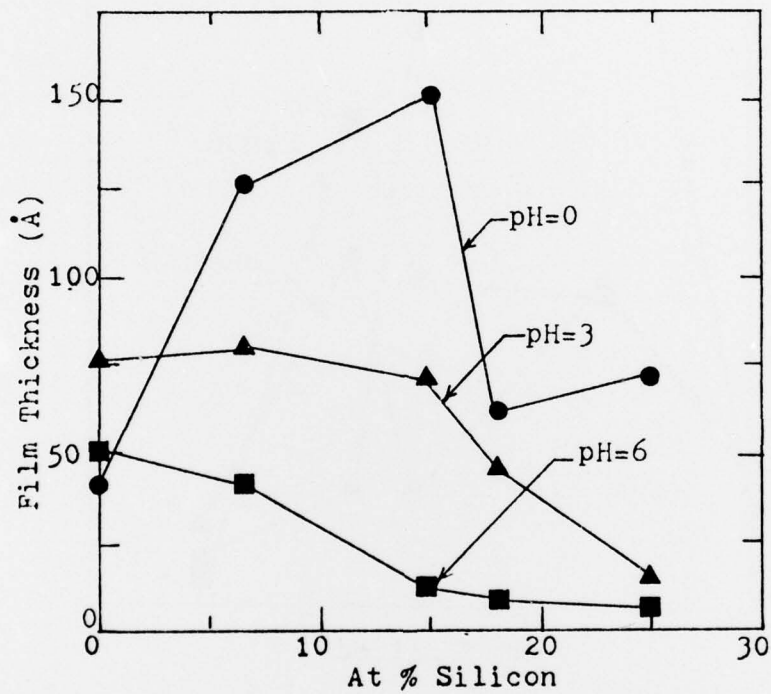


Figure 71. Film thickness from Auger sputtering times assuming a sputtering rate of 1-3 Å/min plotted vs atomic % silicon in the alloy.

The difference between the values in Figures 70 and 71 represents the amount of iron which was lost into the solution instead of forming an oxide. This difference is greatest for alloys with silicon contents up to 18 at % (10 wt %) silicon and least for 25 at % (14.5 wt %). These results indicate that when there is not sufficient silicon in the alloy to dominate the passivation reaction as in the 25 at % alloy, then the result is worse than if the iron were left unalloyed.

This effect of increased dissolution at low silicon contents may be a manifestation of the quality of the film, i.e., a salt film vs a protective film. An examination of the Auger profiles shows that the 14.5Si (25 at % silicon) does not have any sulfate incorporated in its films, while the other alloys do. Smialowska (38) and Florianovich (39) have suggested that films which incorporate the electrolyte anion are less protective than those that do not. Once the sulfate anion is incorporated into the film it participates in the dissolution of the underlying metal which is manifested in the current decay measurements. It is not until the alloy contains 14.5 wt % (25 at %) silicon that it forms a film which resists salt formation and remains continuous and protective.

#### 5.4 The pH Effect

By varying the solution pH in the sulfate systems, it was possible to determine how the electrochemical behavior of the alloys was affected by pH.

Figure 14 shows the variation of both corrosion potential,  $E_r$ , and passivation potential,  $E_p$ , with pH. For all the samples, there was a linear variation of  $E_r$  with pH for solutions with  $\text{pH} \leq 6.4$ . The slopes of these lines did not follow the reversible hydrogen electrode line, but they do follow from mixed electrode theory; as the pH decreased (increasing  $\text{H}^+$  concentration), the corrosion potentials became more noble while the corrosion current also increased. This occurs because the rate of the reduction reaction is proportional to the concentration of the hydrogen ion raised to the power the reaction order requires (usually less than 2).

The pH effect on the passivation potentials does not follow a linear relation. This effect may be due to the high current densities generated, which may affect the surface reactions.

Once again the Pourbaix diagrams  
Iron does not have a protective oxide in the low pH regions, and the alloy does not contain sufficient silicon to affect passivity until 14.5 wt % (25 at %) silicon is present in the alloy.

The effect of pH on the maximum active current density,  $i_a$ , can be seen in Figure 15. As the solution approaches the neutral pH values,  $i_a$  decreases indicating that less dissolution occurs as the hydrogen ion concentration decreases. This effect is particularly apparent in the 100Fe sample, whose oxides are stable in the neutral pH regions (Figure 1a). The alloys with 3 and 8 wt % (6.5 and 18.5 at %) silicon are not as easily passivated as pure iron.

At 14.5 wt % silicon, however, there is again a decrease in  $i_a$  as the pH increases. But at the basic pH values (pH = 10), there is an increase in the active dissolution current of this alloy. This behavior is explained by the Pourbaix diagrams which indicate that  $\text{SiO}_2$  dissolution occurs in this pH region.

In the passive regions, the increase in the pH from 0 to 6 also decreases the passive current densities,  $i_p$ . At the lowest pH value,  $i_p$  is at a maximum. The increased dissolution of the alloys in the passive state is also indicated in the Auger results. A comparison of the slopes of the excess silicon lines in Figures 59 (pH = 0) and 60 (pH = 3) shows that there is a higher ratio of silicon (2.6) in the film at pH = 0, than there is at pH = 3 (slope = 1.9). At pH = 6, the excess silicon approaches the line of equal concentrations in the film and alloy. Thus, the effect of pH is seen in the film; silicon enriches more at the acid pH's. This silicon enrichment is manifested by the variation in  $i_p$  with pH.

A similar analysis at pH = 10 was not possible because the passive films on the low silicon samples were too thick for AES analysis. Charging effects (34, 35) dominated the spectra of these alloys so meaningful information was obscured.

The effect that pH has on the current vs time behavior of the alloys can be seen in Figure 69. The acid pH solutions exhibit similar growth kinetics with a slope of  $-1/2$ . The neutral and basic solutions had slope values of  $-2/3$ . The difference in slopes indicated that the samples passivated more quickly in neutral solutions than in the acid solutions where there was greater dissolution.

Thus, it has been possible to explain the pH effects observed in terms of the equilibrium diagrams for iron-water and silicon-water.

#### 5.5 Breakdown of Passivity

Since previous studies (12-14) had shown that minor additions of silicon to stainless steels enhanced their resistance to pitting, a study of the binary pitting resistance was initiated. It was hoped that the role of silicon in the process could be understood in terms of the pitting models. The borate buffer with potassium chloride additions was used instead of a sodium chloride solution because no active-passive behavior was obtained in the latter solution.

The results from the pitting potential measurements indicate that low silicon additions (3 and 8 wt %) are detrimental; the pitting potentials are more active for these alloys than for pure iron. However, at 10 wt % silicon, there is an improvement in pitting resistance. These effects may be due to the cleanliness of the alloy. Pits may initiate at inclusions or surface defects accounting for a less resistant alloy. However, this lowered pitting resistance was consistent with the increased dissolution observed for these alloys in the sulfate solutions.

No pitting was observed for 14.5 wt % (25 at %).

In terms of alloy development, the pitting results were surprising. In previous alloy evaluation studies (12-14) 2-3 wt % silicon enhanced pitting resistance in stainless steels. In light of the pitting results, the composition effect must be a synergistic effect of silicon with another alloying element in the material. Since no silicon enrichment



has been found in the passive films on stainless steels, the silicon may affect the repassivation kinetics of an alloy; this can be determined by ternary alloy studies.

### 5.6 The Anion Effect

The behavior of the alloys was influenced by the electrolyte in which the experiments were run. This next part of the discussion is divided into the effect of the borate, the sulfate, and the chloride ions.

#### 5.6.1 Borate

The buffering action of a borate solution has been recognized (20). But it provides a solution where the active-passive reaction on iron has been easily studied.

For studying the iron-silicon alloys, the solution may not have been as adequate as it was for pure iron studies. In this solution 3 wt % (6.5 at %) silicon was sufficient to permanently shift the rest potential,  $E_r$ , in the noble direction (Figure 66). All the iron-silicon alloys exhibited greater stability than pure iron in this solution. This result may be due to the buffering action of the solution such that small additions of an alloying element are reflected in the corrosion potential.

In the AES results, the passive film formed on the 14.5Si sample is comparable to the film which is on the alloy prior to immersion in the solution. Consequently, this alloy was never in the film-free state when it was anodically polarized.

The lower silicon samples, on the other hand, did develop anodic films which contained excess silicon (Figure 58). The excess silicon probably results from iron dissolution in the solution. This increased silicon in the film, however, cannot be correlated with the passive current densities observed.

Seo et al (36) have postulated that the borate ion enters into the formation of a passive film. An examination of the AES results for 3Si and 8Si where relatively thick anodic films formed shows that boron is also incorporated in these films. An added silicon reaction must be taken into account for the formation of the film.



In this solution although some effects of silicon content could be noted, the air formed films were never completely removed by the cathodic reduction.

#### 5.6.2 The Sulfate Ion

The action of the sulfate ion is not entirely clear. AES results on alloys with less than 14.5 wt % (25 at %) silicon show that sulfur is incorporated into the passive films. Only in the solution with pH = 10, does that alloy form a film which incorporates sulfur. The pure iron and low silicon alloys had high active current densities in all the sulfate solutions indicating that the sulfate anions accelerated their active dissolution.

Florianovich et al (39) proposed that in sulfate solutions, the anions of the electrolyte directly participate in the process of iron dissolution. Gibbs and Cohen (40) and Smialowska et al (38) also found that the anodic films formed on iron consisted of iron-oxy-sulfate,  $\text{Fe}_3\text{O}_4$  and  $\text{FeOOH}(\delta)$ . These results are in accordance with those ideas.

The films formed on the binary alloys consist of iron oxides, silicon oxide, and sulfates. No compound or mineral consisting of iron silicate-sulfate was found in a search through thermodynamic and X-ray crystallographic tables. The only compound which might be postulated for the low silicon alloys might be an iron silicate,  $\text{Fe}_2\text{SiO}_4$  (fayalite). But this compound would not account for the sulfate. Thus, the iron oxy-sulfate reaction would still have to occur.

Smialowska (38) has postulated that the presence of sulfate ions in the passive film decreases its protective properties. Some evidence for this behavior can be drawn from the AES results combined with the electrochemical measurements. The films on the high silicon alloy (14.5 wt %) exhibit no evidence of sulfate; this is the alloy with the most protective film. In the lower silicon alloys, however, sulfate anions are indicated; these are the alloys with the highest dissolution rates. Thus, the film consisting

of an iron and silicon oxide mixture with sulfate anions affords the least protection. Silica films such as those found on 14.5 wt % silicon alloys are the most protective and resistant to sulfate anion penetration.

### 5.6.3 Chloride Ion

As a prelude to this discussion, a brief summary of the AES results which are referred to is presented.

The AES result on pitted samples are shown in Figure 52. These results show that some material dissolution took place and flowed out of the pitted area. There are some features on these pits which are not explained. Among these is the potassium halo about the pits; another is that boron is concentrated in the "flow region." The composition profile for the flow region, Figure 53, indicates that silicon is not a major constituent of this material. The Auger image shows that silicon has concentrated in the pit and that iron has dissolved. Although the Auger image does not show an iron enrichment and the presence of iron oxides (inserts). Chlorine has not deposited inside the pit but is concentrated in the flow material. It appears that the material is a ferrous borate with chloride, which has deposited as the iron dissolved out of the pit.

Four pitting models have been postulated in order to understand the alloying role in the process. In the adsorbed ion displacement model, the chloride ion is supposed to adsorb on the passive film, displace oxygen in the film, and breakdown the film. The pitting potential is that potential at which chloride adsorption occurs. This work did not determine the relation between adsorption and pitting potential. The same applies to the ion penetration model.

The chemical-mechanical model proposed that breakdown occurs where the damaging anion (chloride) promotes the formation of pockets of non-protective, low density material, which affects the repassivation rate of the film. The AES results showed the formation of a ferrous borate-chloride deposit, but whether this is a non-protective material, it is not possible to say.

Certainly, no silicon oxide film was detected in the vicinity. The silicon was concentrated only in the pit.

In the transport process model, the pitting potential,  $E_p$ , is affected by the alloy composition, and it is the potential needed for sustained pit activity. This work has determined  $E_p$  is composition dependent. Galvele (41) proposes that competitive adsorption and salt film formation do not enter into this model. In this respect the model does not explain the flow material observed. Since  $E_p$  consists of several factors such as an over-potential term and an inhibitor term which were not measured it was not possible to evaluate  $E_p$  in terms of predicted values vs measured values.

#### 6.0 CONCLUSIONS

The conclusions which are reached on the basis of the experimental results presented in this work are:

(1) The beneficial effects of silicon alloying for corrosion resistance is not effective until the alloy contains 14.5 wt % (25 at %) silicon; silicon contents of less than 8 wt % (15 at %) are detrimental to the corrosion properties in sulfate and chloride solutions.

(2) Silicon enrichment and the formation of an  $\text{SiO}_2$  film are responsible for the corrosion resistant properties.

(3) The formation of an  $\text{SiO}_2$  film resists the penetration of the sulfate anion.

(4) Since no evidence of enhanced pitting resistance was noted in 3 and 8 wt % (6.5 and 15 at %) silicon alloys, it is postulated that the increased pitting resistance noted in stainless steels with 2-3 % silicon is due to a synergistic effect of silicon with another alloying element.

# REFERENCES

1. M.G. Corson, AIME Tech. Publ. No. 96, 249 (1928).
2. R.J. McKay and R. Worthington, Corrosion Resistance of Metals and Alloys, Reinhold Publishing Corporation, New York, 274, (1936).
3. M. Pourbaix, Atlas of Electrochemical Equilibria, Pergamon Press, London, pp. 308 and 459, (1966).
4. W.T. Bryan, "Silicon-Iron Alloys," in The Corrosion Handbook, H.H. Uhlig ed., John Wiley and Sons, New York, p. 201, (1948).
5. M.G. Fontana and N.D. Greene, Corrosion Engineering, McGraw-Hill Book Company, New York, p. 161, (1967).
6. L.L. Shrier, ed. Corrosion, Vol. 1, Newnes-Betterworth, Boston, Chapter 3.9, (1976).
7. F.P.A. Robinson and D.J. DuPlessis, Corrosion, 22, p. 117, (1966).
8. Y. Omartug and M. Doruk, Corrosion Science, 10, p. 225, (1970).
9. W.B. Crow, J.R. Myers and J.V. Jeffries, Corrosion, 28, p. 77 (1972).
10. O. Tajima, K. Nakao, M. Matusda and H. Miyamae, Chemical Abstracts, 69, 64046b, (1968).
11. H. Mitani, M. Onishi and M. Yagjima, Chemical Abstracts, 70, 63346h, (1969).
12. M.A. Streicher, J. Electrochem. Soc., 103, 384, (1956).
13. S.M. Novokshchenova, A.A. Babakov and V.M. Knyazheva, ZashchitaMetal., 4, 588, (1968).
14. A.W. Lozinow and T.F. Bates, Corrosion, 25, 15, (1969).
15. T.N. Rhodin, Corrosion, 12, 123t, (1956).
16. J.E.O. Mayne and P. Ridgway, Brit. Corr. et., 6, 244, (1971).
17. G.C. Wood and C.F. Cammack, Corrosion Science, 8, 159, (1968).
18. A. Joshi, L.E. Davis, and P.W. Palmberg, "Auger Electron Spectrscopy," in Methods of Surface Analysis Vol. 1: Methods and Phenomena: Their Application in Science and Technology, A.W. Czanderna, ed, Elsevier Scientific Publ. Co., New York, 15q, (1975).
19. M. Seo, J.B. Lumsden, and R.W. Staehle, Surface Science, 50, 541, (1975).



20. M. Nagayama and M. Cohen, J. Electrochem. Soc., 109, 781, (1962).
21. G. Economy, R. Speiser, F.H. Beck and M.G. Fontana, *ibid.*, 108, 337, (1961).
22. J.H. Bartlett and L. Stephenson, *ibid.*, 99, 504, (1952).
23. M. Frommet, M. Keddam and P. Morel, C.R. Acad. Sci. Paris, 253, 2529, (1961).
24. Z. Epelboin, C. Gabrielle, M. Keddam, J.C. Lestrade and H. Takenouti, J. Electrochem. Soc., 119, 1632, (1972).
25. S. Asakura and K. Nobe, *ibid.*, 118, 536, (1971).
26. C.M. Shephend and S. Schuldiner, *ibid.*, 115, 1124, (1968).
27. M. Janik-Czachor, Brit. Corr. J., 6, 57, (1971).
28. Z. Szklarska-Smialowska, Corrosion, 27, 223, (1971).
29. K.J. Vetter and H.H. Streblow, "Pitting Corrosion in an Early Stage and Its Theoretical Implications," in Passivity and Its Breakdown on Iron and Iron Base Alloys, USA-Japan Seminar, NACE, Houston, 10, (1976).
30. D.A. Stout, Corrosion, in press, (1978).
31. C.J. Semino and J.R. Galvele, Corrosion Science, 16, p. 297, (1976).
32. M. Seo, J.B. Lumsden and R.W. Staehle, Surface Science, 50, p. 541, (1975).
33. R.P. Frankenthal and D.M. Calcom, J. Electrochem. Soc., 123, p. 186, (1976).
34. C.C. Chang and D.M. Bolin, Surface Science, 69, 385, (1977).
35. B. Barriere and B. Lang, *ibid.*, 64, 209, (1977).
36. M. Seo, M. Sato, J.B. Lumsden and R.W. Staehle, Corrosion Science, 17, 209, (1977).
37. G.R. StPierre, W.M. Boorstein, and H.C. Lin, "Ductility of Iron-Silicon Alloy Castings,: Final Report, The Ohio State University, Research Foundation, No. 3366, (1973).
38. Z. Szklarska-Smialowska and G. Mrowczynski, Brit. Corr. J., 10 187, (1975).
39. G.M. Florianovich, L.A. Sokolva and Y.M. Kolotyarkin, Electrochim. Acta, 12, 879, (1967).
40. D.B. Gibbs and M. Cohen, J. Electrochem. Soc., 119, 416, (1972).
41. J.R. Galvele, *ibid.*, 123, 464, (1976).